The effect of small-scale heterogeneity
on the propagation of waves

with application to forward modeling and
inversion in global surface wave tomography

Jesper Spetzler

The effect of small-scale heterogeneity on the propagation of waves

with applications to forward modeling and inversion in global surface wave tomography

Het effect van kleinschalige heterogeniteiten op golfvoortplanting

met toepassing op voorwaartse modelering en inversie in globale oppervlaktegolf tomografie

(met samenvattingen in het Nederlands en het Deens)

PROEFSCHRIFT

TER VERKRIJGING VAN DE GRAAD VAN DOCTOR AAN DE UNIVERSITEIT UTRECHT, OP GEZAG VAN DE RECTOR MAGNIFICUS, PROF. DR W. H. GISPEN, INGEVOLGE HET BESLUIT VAN HET COLLEGE VOOR PROMOTIES IN HET OPENBAAR TE VERDEDIGEN OP WOENSDAG 20 JUNI, 2001 DES MIDDAGS TE 14:30 UUR

DOOR

Jesper Spetzler

GEBOREN OP 13 JULI 1972, TE KOPENHAGEN, DENEMARKEN

Promotor :   Prof. Dr R. K. Snieder
                Institute of Earth Sciences
                Utrecht University
                The Netherlands
                now at:
                Dept. of Geophysics
                Golden School of Mines
                USA
Co-Promotor: Dr J. Trampert
                Institute of Earth Sciences
                Utrecht University
                The Netherlands

Who dares to take a chance, may get disappointed for a moment,
who does not dare to take a chance, may regret for the rest of life.

(Free translation from Danish to English)
Søren Aabye Kierkegaard, Danish Philosopher, 1813-1855.

To the ones I love and care about.

Contents

Chapter 1

Introduction

Seismic tomography is a technique to study the internal structure of the Earth. The word tomography originates from the two Greek words *tomos* meaning *a slice* and *graphi* meaning *to write on*, and these two words together signify *to write on a slice*. Seismological tomography (Iyer and Hirahara, 1993) is the discipline where information (e.g. timeshifts, phaseshifts, absolute travel times or amplitudes) retrieved from seismic waves probing the Earth is converted into images of the Earth's velocity structure, so that we can get a better insight into the structures and processes which take place in the Earth.

Techniques applied in seismology are mostly based on simplified versions of ray theory (Dziewonski, 1984; Woodhouse and Dziewonski, 1984; Iyer and Hirahara, 1993; Trampert and Woodhouse, 1995; Bijwaard and Spakman, 1998; Curtis *et al*., 1998; Ritzwoller and Levshin, 1998). Ray theory is a high-frequency approximation in which wave energy propagates along infinitely narrow trajectories called rays. The consequence is that for wavefield calculations using ray theory, only the velocity structure on the ray between the source and receiver is important. It is correct to apply ray theory in the description of the propagation of waves in media with heterogeneity that changes slowly over a characteristic scales a that is large with respect to the wavelength λ and the width L_F of the Fresnel zone. The length-scale of inhomogeneity, the wavelength and the Fresnel zone are illustrated in Fig. 1.1. The Fresnel zone is defined as the region between the source and receiver that generates scattered waves which interfere constructively when they arrive at the receiver position. In Fig. 1.1, an example of a diffracted wave due to a point scatterer inside the Fresnel zone is given; A wave is emitted from the source (star) and follows the path L_1 to the point scatterer (thick circular point) and is deflected in the direction of the receiver (triangle). The diffracted wave propagating towards the receiver follows the path L_2. The ballistic wave which is the first arriving energy propagating along the straight line with the length $L_{ballistic}$ between the source and receiver. The condition for constructive interference of waves is that the difference in propagation length of the diffracted wave and the ballistic wave, $L_1 + L_2 - L_{ballistic}$, is smaller than a certain fraction of the wavelength. (In the literature, one uses that the wavelength is divided by 2 or 4 in order to assure constructive interference of waves, Yilmaz, 1987; Hardage, 1992). Scattering

theory of waves is relevant for the description of wave propagation in media with velocity anomalies that vary on scale-lengths comparable to the wavelength and the width of the Fresnel zone. This causes wave energy to be scattered, and ray theory is inadequate in explaining the change of wavefields due to the perturbation of the velocity in such complex media.
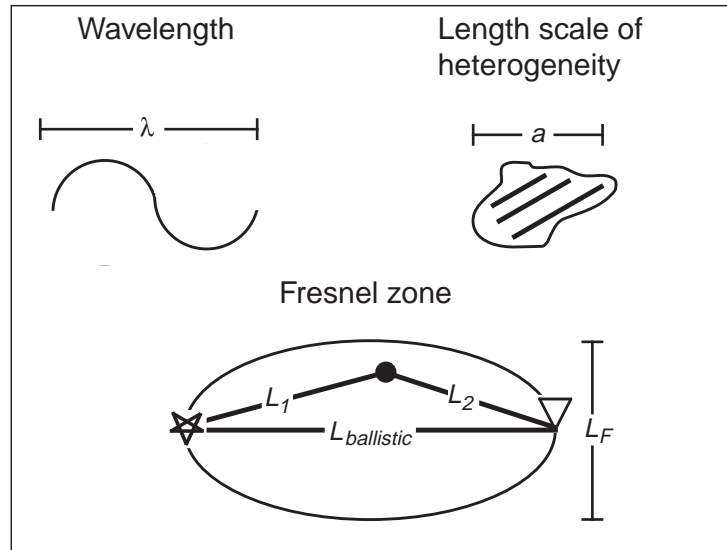
Figure 1.1: *An illustration of the physical variables that are used to define the validity of ray theory and scattering theory. The wavelength is denoted by λ and the characteristic length of heterogeneity is written as a. The concept of Fresnel zones is defined in terms of constructive interference of waves that are scattered by heterogeneity inside the Fresnel zone. For instance, a diffracted wave propagating from the source (star) and to the receiver (triangle) following the path $L_1 + L_2$ is deflected by the point scatterer (thick circular point). The first arriving wavefield propagates along the line $L_{ballistic}$. The width of the Fresnel zone is denoted by L_F.*

Present-day high-resolution tomographic models obtained in seismology show length-scales of inhomogeneity which are comparable with the wavelength and the Fresnel zone (e.g. Passier and Snieder, 1995). This means that the conditions for ray theory in high-resolution tomography are often violated, which introduces a problem from a methodological point of view. It is unacceptable to use an approximate theory (namely ray theory) in imaging experiments for which the conditions of the applied theory are not fulfilled in the end-result (i.e. the tomographic image). In order to improve the theory for wave propagation in tomographic imaging experiments, it is important to take the scattering of waves into account.

In this thesis, a linear theory for transmitted waves is developed by applying the first-order Rytov approximation (Snieder and Lomax, 1996) on the acoustic wave equation. It is shown that a frequency-dependent delay time can be expressed as a volume integral of the slowness perturbation field weighted by the Fréchet kernel, where the Fréchet kernel is a function that specifies the sensitivity to the slowness perturbation field point by point in the volume between the source and receiver. This sensitivity function that accounts for non-ray geometrical effects, has the maximum sensitivity to slowness perturbations away from the geometrical ray. One obtains the counter-intuitive result that for waves propagating in three dimensions the slowness perturbation sensitivity vanishes on the ray path connecting the source and receiver. Ray theory predicts that the sensitivity to slowness perturbations is only non-zero on the ray. This result also has been derived using a different approach, namely a linearised version of the cross-correlation function wherein the single-scattering of waves is taken into account (Marquering *et al.*, 1998; Tong *et al.*, 1998; Marquering *et al.*, 1999; Dahlen *et al.*, 2000; Hung *et al.*, 2000; Zhao *et al.*, 2000).

The theoretical developments of diffraction theory are tested in a numerical as well as in a laboratory experiment using ultrasonic waves in which scattering effects are important. These experiments clearly show that ray theory and scattering theory give the same result in media where the conditions for ray theory are valid. For more complex media, where the conditions for ray theory are no longer satisfied, one needs to use diffraction theory for the description of the propagation of first arriving waves.

Triplications (related to caustics) are multi-valued wavefield arrivals for which the amplitude of the first arriving wave may be much smaller than the amplitude of the later arrivals. It is therefore difficult to detect the first arriving wave when the formation of caustics is relevant. Triplications occur when a wavefield propagates in a medium with focusing effects (Kravtsov, 1988). It is shown by using numerical experiments of transmitted waves in complex media that caustics present in the propagating wavefield are delayed compared with the first arrival. The developed diffraction theory for ballistic waves is applicable even though the formation of caustics is significant.

The finite-frequency effect of velocity perturbation on transmitted, unconverted surface waves is incorporated in a global surface wave tomographic experiment. Phaseshifts for Love waves with periods at 40 s and 150 s are used in an inversion for the global phase velocity using the ray theoretical great circle approximation (Woodhouse and Dziewonski, 1984; Trampert and Woodhouse, 1995) and the scattering theoretical approach. The scattering of surface waves is increasingly important for increasing period because the width of the Fresnel zone increases with period. That is why the limitations of ray theory in surface wave tomography are most restrictive for the longest periods.

The developed diffraction theory is not only limited to the application in global surface wave tomography. The non-ray geometrical effect should be considered in other wave experiments as well, where the conditions for ray theory are questionable. This is for example the case in regional surface wave tomography and global body wave tomography (van der Lee and Nolet, 1997; Bijwaard and Spakman, 1998; Ritzwoller and Levshin, 1998), in seismic exploration experiments such as borehole-to-borehole tomography, vertical seismic profiling and reflection seismics (Yilmaz, 1987; Hardage, 1992; Parra and Bangs, 1992; Goudswaard *et al.*, 1998; Hatchell, 2000), in medical imaging

such as ultrasonic sound imaging of the chest, the heart, the foetus, the veins etc.. (Baba *et al.*, 1989; King and Shao, 1990) and in ocean acoustics (Hodgkiss *et al.*, 1999).

In addition, it is of interest to investigate to what extent diffraction theory in tomographic wave experiments can increase the resolution in tomographic models. Consider for instance synthetic aperture radar (SAR) experiments (Massonnet and Feigl, 1998) that are used to retrieve high-resolution radar images of the Earth's surface. The radar waves are emitted and recorded by satellites that circle around the Earth. It is found in SAR that the highest possible resolution in radar images (for instance of topography) is much smaller than the width of the Fresnel zone. The high resolution of SAR-images is due to the fact that SAR focuses the radar images by overlapping the Fresnel zone of these radar waves. In a similar vein, it is possible to increase the resolution of controlled seismic wave experiments such as borehole-to-borehole seismic, vertical seismic profiling and reflection seismic where the Fresnel zones of seismic waves with different source-receiver geometry overlap.

The last part of this thesis treats the spectral leakage problem (Trampert and Snieder, 1996). The term spectral leakage means that observed data affected by structures with a length-scale that is not accounted for in a given inversion can leak into the long-wavelength structures that are part of the estimated model. In the case of global surface wave tomography, surface wave scattering theory is used in an inversion including the spectral leakage correction of phase velocity measurements for Love waves at periods of 40 s and 150 s.

Chapter two deals with triplications of waves propagating in two and three dimensional media. Criteria for the formation of caustics are derived for models with horizontally layered structures and for Gaussian random media, respectively, using ray perturbation theory. The theory for the formation of caustics is applied in **chapter three**, where a 2-D finite-difference wave experiment is carried out using complex media for which scattering theory and focussing effects are both important. The approach based on the scattering of waves is compared with the ray theoretical treatment in the 2-D finite-difference wave experiment. The conditions for scattering theory are confirmed in a specially designed slowness perturbation model. Additionally, it is shown that scattering theory predicts very well the observed data obtained from the finite-difference wave experiment using slowness perturbation media for which the effect of wave scattering is significant. In **chapter four**, a test of the developed diffraction theory is carried out in a physical experiment where ultrasonic waves propagate in samples of granite with grain-sizes much smaller than the Fresnel zones. The ultrasonic wave experiment was conducted at the Geological Survey of Japan in collaboration with Osamu Nishizawa and Chadaram Sivaji. In **Chapter five**, the scattering theory is applied in surface wave tomography. It is shown in this chapter that present-day global high-resolution surface wave tomography is at the limits of the application of the ray theoretical great circle approximation. The inversion of phase velocity measurements is considered in **Chapter six** for Love waves between 40 s and 150 s in global surface wave tomography where surface wave scattering theory is combined with spectral leakage theory.

References

Baba K., Satch S., Sakamoto S., Okai T. and Shiego I. (**1989**). Development of an ultrasonic system for three-dimensional reconstruction of the foetus, J. Perinat Med. **17**, 19-24.

Bijwaard H. and Spakman W. (**1998**). Closing the gab between regional and global travel time tomography, Geophys. Res. Lett. **103**, 30055-30078.

Curtis A., Trampert J., Snieder R. and Dost B. (**1998**). Eurasian fundamental mode surface wave phase velocities and their relationship with tectonic structures, J. Geophys. Res. **103**, 26919-26947.

Dahlen A., Hung S. H. and Nolet G. (**2000**). Fréchet kernels for finite-frequency travel times-I. theory, Geophys. J. Int. **141**, 157-174.

Dziewonski A. M. (**1984**). Mapping the lower mantle: determination of lateral heterogeneity in *P*-velocity up to degree and order 6, J. Geophys. Res. **89**, 5929-5952.

Goudswaard J. C. M., ten Kroode F. P. E., Snieder R. and Verdel A. R. (**1998**). Detection of lateral velocity contrasts by crosswell traveltime tomography, Geophysics **63**, 523-533.

Iyer H. M. and Hirahara K. (**1993**). *Seismic tomography; theory and pratice* (Chapman and Hall.).

Hardage B. A. (**1992**). *Crosswell seismology and reverse VSP* (Geophysical Press LTD, London.).

Hatchell P. K. (**2000**). Fault whispers: transmission distortions on prestack seismic reflection data, Geophysics **65**, 377-389.

Hodgkiss W. S., Song H. C., Kuperman W. A., Akal T., Farla C. and Jackson D. (**1999**). A long-range and variable focus phase-conjugation experiment in shallow water, J. Acoust. Soc. Am. **105**, 1597-1604.

Hung S. H., Dahlen A. and Nolet G. (**2000**). Fréchet kernels for finite-frequency travel times-II. examples, Geophys. J. Int. **141**, 175-203.

van der Lee S. and Nolet G. (**1997**). Upper mantle *S*-velocity structure of North America, J. Geophys. Res. **102**, 22815-22838.

King D. L. and Shao M. Y. (**1990**). Three-dimensional spatial registration and interactive display of position and orientation of real-time ultrasound images, JUM. **9**, 525-532.

Kravtsov Y. A. (**1988**). Rays and caustics as physical objects in *Prog. in Optics*, XXVI, Edited by Wolf E. (Elsevier, Amsterdam), 227-348.

Marquering H., Nolet G. and Dahlen F. A. (**1998**). Three-dimensional waveform sensitivity kernels, Geophys. J. Int. **132**, 521-534.

Marquering H., Dahlen F. A. and Nolet G. (**1999**). The body-wave traveltime paradox: bananas, doughnuts and 3-D delay-time kernels, Geophys. J. Int. **137**, 805-815.

Massonnet D. and Feigl K. L. (**1998**). Radar interferometry and its application to changes in the Earth's surface, Rew. Geophys. **36**, 441-500.

Parra J. O. and Bangs J. H. (**1992**). High-resolution reverse VSP and interwell seismic experiments at the Buckhorn test site in Illinois, *62nd Annual Internat. Mtg., Soc. Expl. Geophys., Expanded Abstracts* 103-107.

Passier M. L and Snieder R. (**1995**). Using differential waveform data to retrieve local S-velocity structure or path-averaged S-velocity gradients, J. Geophys. Res. **100**, 24061-24078.

Ritzwoller M. H. and Levshin A. L. (**1998**). Eurasian surface wave tomography: group velocities, J. Geophys. Res. **103**, 4839-4878.

Snieder R. and Lomax A. (**1996**). Wavefield smoothing and the effect of rough velocity pertubations on arrival times and amplitudes, Geophys. J. Int. **125**, 796-812.

Tong J., Dahlen F. A., Nolet G. and Marquering H. (**1998**). Diffraction effects upon finite-frequency traveltimes: a simple 2-D example, Geophys. Res. Lett. **25**, 1983-1986.

Trampert J. and Woodhouse J. H. (**1995**). Global phase velocity maps of Love and Rayleigh waves between 40 and 150 seconds, Geophys. J. Int. **122**, 675-690.

Trampert J. and Snieder R. (**1996**). Model estimation biased by truncated expansions: possible artifacts in seismic tomography, Science **271**, 1257-1260.

Yilmaz Ö. (**1987**). *Seismic data processing* (Society of Exploration Geophysicists).

Woodhouse J. H. and Dziewonski A. M. (**1984**). Mapping the upper mantle: three-dimensional modeling of Earth structure by inversion of seismic wavefroms, J. Geophys. Res. **89**, 5953-5986.

Zhao L., Jordan T. H. and Chapman C. H. (**2000**). Three-dimensional Fréchet differential kernels for seismic delay times, Geophys. J. Int. **141**, 558-576.

Chapter 2

The formation of caustics in two and three dimensional media

Abstract.

In terms of ray theory, the focus point (also related to caustics and triplications) is the point in space where the ray position is stationary for perturbations in the initial condition. Criteria for the formation of caustics are presented. With ray perturbation theory, a condition for the development of triplications is defined for plane wave sources and for point sources. This theory is then applied on two cases of slowness media; 1-D slowness perturbation models and 2-D Gaussian random media. The focus position in 1-D slowness models is proportional to the inverse of the square root of relative slowness fluctuations. For Gaussian random media, the distance at which caustics generate is dependent on the relative slowness perturbation in a power of - 2/3. It is shown with snaphots of propagating plane wavefields that caustics develop as predicted by theory. The theory for caustic formation can be generalised to three dimensions.

2.1   Introduction

In terms of ray theory, the concept of caustics is understood as the focus point in space through which rays go. The consequence of the generation of caustics in a wavefield is, in the ray geometrical limit, that the amplitude in the wavefield is infinitely high at the focus point because the geometrical spreading factor is zero at the caustic point (Aki and Richards, 1980; Menke and Abbot, 1990). This phenomenon is investigated by several authors; White *et al*. (1988) use limit theorems for stochastic differential equations on the equation of dynamic ray tracing to predict when caustics start to develop in Gaussian random media. Kravtsov (1988) gives a thorough description of caustics. Brown and Tappert (1986) use Chapman's method to write explicitely the variation of 2-D and 3-D

wavefields in the vicinity of focus points. They set up three properties of transient wave-fields away from caustics; the most important characteristic of transient waves through caustics is that the triplication will generate after the ballistic wavefield due to causality.

A new theory for caustic formation is presented. This theory is based on ray pertur-bation theory but is formally equivalent to dynamical ray theory as used in White *et al.* (1988) because the normal derivative of the equations in ray perturbation theory is identi-cal to the equation of dynamic ray tracing (Pulliam and Snieder, 1998). In contrast to the treatment of White *et al.* (1988) this application is not restricted to random media.

In section 2.2, the general theory for caustic formation of wavefields emitted by plane wave sources and point sources is presented. The theory is then applied on a 1-D slowness perturbation medium and a 2-D Gaussian random medium for both plane wave sources and point sources. The results for the 2-D Gaussian random medium are similar to those found in White *et al.* (1988). In section 2.3, the theory for caustic formation is tested on numerical experiments where a plane wavefield propagates in a 1-D slowness perturbation field and in a 2-D Gaussian random medium.

2.2   Theory

We demonstrate how the focal length of converging wavefields in 2-D slowness perturba-tion fields can be computed. First, we derive the general theory for two distinct source geometries; the plane wave (plw) source and the point source (ps). Second, we apply this theory on two case studies; 1-D slowness perturbation fields and 2-D Gaussian random media. The presented theory for caustic formation can be generalised to three dimensions.

2.2.1   General theory

We make use of ray perturbation theory (Snieder and Sambridge, 1992) and separate the ray into a reference ray and a perturbed ray. The slowness field $u = u_0 + u_1$, is decom-posed into the reference slowness field u_0 and the slowness perturbation field u_1. The reference slowness u_0 is kept constant in this work which means that the reference ray is a straight line. The perpendicular deflection from the reference ray to the perturbed ray at propagation distance x_0 is denoted by $q(x_0)$.

First, the case of an incoming plane wave is treated. Imagine two horizontal reference rays with slightly different initial positions. One reference ray is at the position z while the other reference ray is at the position $z + \delta z$. See Fig. 2.1 for a definition of the geometrical variables. For each reference ray there is a perturbed ray due to the slowness perturbation in the medium. The condition for caustics, that is to say that the two perturbed rays intersect, gives the following equation:

$$q(x_0, z + \delta z) + \delta z - q(x_0, z) = 0, \qquad (2.1)$$

or

$$\frac{\partial q}{\partial z}(x_0) = \lim_{\delta z \to 0} \frac{q(x_0, z + \delta z) - q(x_0, z)}{\delta z} = -1. \qquad (2.2)$$
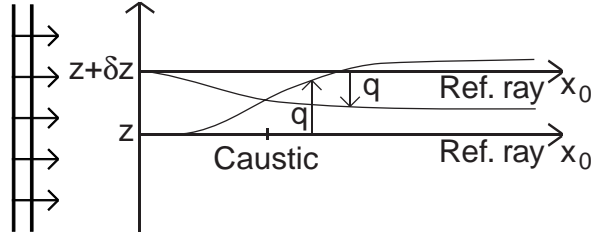
Figure 2.1: *Definition of the geometric variables for an incoming plane wave in a 2-D medium with a constant reference slowness. There is one horizontal reference ray at z and another one at $z + \delta z$. The caustic develops at the intersection point of the two perturbed rays.*

Snieder and Sambridge (1992) show how the perpendicular ray deflection $q(x_0)$ from the reference ray can be computed given the slowness perturbation u_1;

$$q(x_0) = \int_0^{x_0} G(x_0, x) \left[\partial_\perp \left(\frac{u_1}{u_0} \right) \right](x) dx, \tag{2.3}$$

with $\partial_\perp$ the component of the gradient perpendicular to the reference ray so that

$$q(x_0) = \int_0^{x_0} G(x_0, x) \frac{\partial}{\partial z} \left(\frac{u_1}{u_0} \right)(x) dx, \tag{2.4}$$

for a horizontal reference ray. The Green's function

$$G(x_0, x) = \begin{cases} 0 & \text{if } x_0 < x \\ x_0 - x & \text{if } x_0 > x \end{cases}, \tag{2.5}$$

has the boundary conditions, $G(0, x) = \dot{G}(0, x) = 0$. The condition for caustics in Eq. (2.2) contains the partial derivative of $q(x_0)$ with respect to z. Using Eq. (2.4) together with the condition for caustics in Eq. (2.2) at given z, we find that caustics are formed at x_0 when

$$\int_0^{x_0} G(x_0, x) \frac{\partial^2}{\partial z^2} \left(\frac{u_1}{u_0} \right)(x) dx = -1. \tag{2.6}$$

Second, the point source case is considered. We investigate the generation of caustics developing for rays that leave a point source with the azimuth φ. Assume again that two reference rays with slightly different initial positions are emitted from the source. One reference ray is sent in the direction $\varphi + \delta\varphi/2$, while the other reference ray is emitted in the direction $\varphi - \delta\varphi/2$. The distance between the reference rays is given by $x_0 \delta\varphi$. The condition that the two perturbed rays cross each other leads to the following equation:

$$q(x_0, \varphi + \frac{1}{2}\delta\varphi) + x_0 \delta\varphi - q(x_0, \varphi - \frac{1}{2}\delta\varphi) = 0, \tag{2.7}$$

or

$$\frac{1}{x_0}\frac{\partial q}{\partial \varphi}(x_0) = \frac{1}{x_0}\lim_{\delta\varphi\to 0}\frac{q(x_0,\varphi+\frac{1}{2}\delta\varphi)-q(x_0,\varphi-\frac{1}{2}\delta\varphi)}{\delta\varphi} = -1. \qquad (2.8)$$

Using $\partial_\perp = (1/x)(\partial/\partial\varphi)$ in Eq. (2.3) the perpendicular ray deflection to the reference ray is derived. Hence

$$q(x_0) = \int_0^{x_0} G(x_0,x)\frac{1}{x}\frac{\partial}{\partial\varphi}\left(\frac{u_1}{u_0}\right)(x)dx. \qquad (2.9)$$

The Green's function in Eq. (2.9) for the reference ray with the azimuth φ is the same as in the case of incoming plane waves which is stated in Eq. (2.5). With Eq. (2.9) combined with the condition of caustics in Eq. (2.8) at given z, we get that caustics generate at x_0 when

$$\frac{1}{x_0}\int_0^{x_0} G(x_0,x)\frac{1}{x}\frac{\partial^2}{\partial\varphi^2}\left(\frac{u_1}{u_0}\right)(x)dx = -1. \qquad (2.10)$$

The second derivative of u_1/u_0 with respect to the transverse coordinate is an important quantity. It reflects that it is the curvature of the relative slowness perturbation that generates caustics. For example, negative $\partial^2/\partial z^2(u_1/u_0)$ and $\partial^2/\partial\varphi^2(u_1/u_0)$ lead to focusing of wavefields, whereas in areas with defocusing effects the two quantities are positive.

2.2.2   A medium with 1-D slowness perturbations

The focus position of a plane wave propagating in a medium with a constant reference slowness field u_0 and 1-D slowness perturbations $u_1(z)$ can be computed analytically. The reference ray in such a medium is a straight at given z. The condition for caustics in the case of incident plane waves given by Eq. (2.6) can be used to determine when caustics start to generate at the offset x_{caus}^{plw} at given z. The integration in Eq. (2.6) is carried out from 0 to x_{caus}^{plw}. Hence

$$x_{caus}^{plw}(z) = \sqrt{\frac{-2}{\frac{\partial^2}{\partial z^2}(\frac{u_1}{u_0})(z)}}. \qquad (2.11)$$

The focal distance x_{caus}^{ps} of wavefields emitted by point sources is easily derived from the condition for caustics in Eq. (2.10). The second derivative $\partial^2/\partial\varphi^2 = x^2\partial^2/\partial z^2$ which permits an evaluation of the integration in Eq. (2.10) in the range from 0 to x_{caus}^{ps}. Thus

$$x_{caus}^{ps}(z) = \sqrt{\frac{-6}{\frac{\partial^2}{\partial z^2}(\frac{u_1}{u_0})(z)}}. \qquad (2.12)$$

The distance between the source and receiver is denoted L. If $x_{caus}^{plw/ps}(z) < L$, triplications will be present in the recorded wavefield.

2.2.3 Gaussian random media

Secondly, we discuss the formation of caustics in Gaussian random media. The auto-correlation function $F(r)$ of a Gaussian random medium is given by

$$
\begin{aligned}
F(r) &= \ <u_1(\mathbf{r}_1)u_1(\mathbf{r}_2)> \\
&= \ (\varepsilon u_0)^2 \exp\left(-\left(\frac{r}{a}\right)^2\right),
\end{aligned}
\tag{2.13}
$$

where ε is the rms value of the relative slowness perturbations, a denotes the correlation length (or roughly the length-scale of slowness perturbations) and $r = |\mathbf{r}_1 - \mathbf{r}_2|$. Notice that the reference slowness is biased in a realisation of a finite Gaussian random model (e.g. Müller *et al*., 1992). However, this artifact does not affect derivatives of the slowness.

According to Eq. (2.2) caustics develop in a plane wavefield when $\partial q/\partial z = -1$. This implies that on average in a random medium caustics develop when

$$
< \left(\frac{\partial q}{\partial z}\right)^2 (x_0) >= 1,
\tag{2.14}
$$

where $< \ldots >$ is the expectation value. For this reason the following quantity is used to monitor the formation of caustics.

$$
\begin{aligned}
H^{plw}(x_0) &\equiv \ < \left(\frac{\partial q}{\partial z}\right)^2 (x_0) >, \\
&= \ \frac{1}{u_0^2} \int_0^{x_0} \int_0^{x_0} G(x_0,x')G(x_0,x'') \\
&\quad \times < \frac{\partial^2}{\partial z^2}u_1(x')\frac{\partial^2}{\partial z^2}u_1(x'') > dx'dx''.
\end{aligned}
\tag{2.15}
$$

The monitor is zero at the source position and $H^{plw}(x_0) = 1$ when caustics start to develop at the offset x_0 according to Eq. (2.14)

We follow the same method as used in Roth *et al*. (1993) to evaluate the right-hand side of Eq. (2.15). First, the expectation value of the slowness perturbation field differentiated with respect to z twice at the offset x' and x'', respectively, in Eq. (2.15) is expressed in a simple form containing the characteristic parameters for the Gaussian random medium. The following expression is evaluated on the horizontal reference ray z_0.

$$
< \frac{\partial^2}{\partial z^2}u_1(x',z)\frac{\partial^2}{\partial z^2}u_1(x'',z) > \Big|_{z=z_0} = \ < \frac{\partial^4}{\partial z'^2 \partial z''^2}u_1(x',z')u_1(x'',z'') > \Big|_{z'=z''=z_0}
$$

$$
= \ \frac{\partial^4 F(r)}{\partial z'^2 \partial z''^2}\Big|_{z'=z''=z_0}.
\tag{2.16}
$$

The auto-correlation function $F(r)$ is differentiated twice with respect to z' and z'' in Eq. (2.16), which gives

$$
\frac{\partial^4 F(r)}{\partial z'^2 \partial z''^2}\Big|_{z'=z''=z_0} = \frac{3}{r^2}\left(F''(r) - \frac{F'(r)}{r}\right)\Big|_{z'=z''=z_0}.
\tag{2.17}
$$

The prime and double prime of $F(r)$ signifies a single and double differentiation with respect to r. Using the auto-correlation function $F(r)$ in Eq. (2.13) for Gaussian random media the left-hand side of Eq. (2.16) is finally written as

$$< \frac{\partial^2}{\partial z^2} u_1(x',z) \frac{\partial^2}{\partial z^2} u_1(x'',z) > \Big|_{z=z_0} = 12 \frac{(\varepsilon u_0)^2}{a^4} \exp(-\left(\frac{r}{a}\right)^2). \qquad (2.18)$$

The right-hand side of the monitor for plane waves in Eq. (2.15) can be simplified further. Define

$$f(r) \equiv < \frac{\partial^2}{\partial z^2} u_1(x',z) \frac{\partial^2}{\partial z^2} u_1(x'',z) > \Big|_{z=z_0}, \qquad (2.19)$$

where $r = |x' - x''|$ and

$$\begin{aligned} \eta(x',x'') &= G(x_0,x')G(x_0,x'') \\ &= x_0^2 + x'x'' - x_0(x' + x''). \end{aligned} \qquad (2.20)$$

We then derive from Eq. (2.15) that

$$\int_0^{x_0} \int_0^{x_0} G(x_0,x')G(x_0,x'') < \frac{\partial^2}{\partial z^2} u_1(x') \frac{\partial^2}{\partial z^2} u_1(x'') > \Big|_{z=z_0} dx'dx'' =$$
$$\int_0^{x_0} \int_0^{x_0} \eta(x',x'')f(|x'-x''|)dx'dx'', \qquad (2.21)$$

for x' and x'' smaller than x_0. Using the integration technique in Roth *et al.* (1993) the expression for the monitor in Eq. (2.15) is simplified further. The details of this integration method are explained in appendix A; here we just give the results. The double integration in Eq. (2.21) from 0 to x_0 is changed to an integration from 0 to x_0 of the function $f(r)$ in Eq. (2.19) multiplied by a summation of two integrations of $\eta(x',x'')$ in Eq. (2.20) from r to x_0 and from 0 to $x_0 - r$, respectively. In brief, the right-hand side of Eq. (2.21) is written as

$$\int_0^{x_0} dr f(r) \left[\int_r^{x_0} \eta(x',x'-r)dx' + \int_0^{x_0-r} \eta(x',x'+r)dx' \right]. \qquad (2.22)$$

The solution to the two integrations of $\eta(x',x'')$ inside the rectangular brackets are computed analytically.

$$\int_r^{x_0} \eta(x',x'-r)dx' = \int_0^{x_0-r} \eta(x',x'+r)dx' = \frac{1}{3}x_0^3 - \frac{1}{2}x_0^2 r + \frac{1}{6}r^3. \qquad (2.23)$$

The expression for the function $f(r)$ in Eq. (2.19) and for the integration of $\eta(x',x'')$ in Eq. (2.23) are used together with the expression for the monitor in Eq. (2.15). Hence the monitor for plane waves propagating in a Gaussian random medium simplifies to

$$H^{plw}(x_0) = 12 \frac{\varepsilon^2}{a^4} \int_0^{x_0} (\frac{2}{3}x_0^3 - x_0^2 r + \frac{1}{3}r^3) \exp(-\left(\frac{r}{a}\right)^2) dr. \qquad (2.24)$$

By letting x_0 go to zero in Eq. (2.24) it is easy to verify that $H^{plw}(0) = 0$.

Assume first that the propagation length is less than the correlation length, i.e. $x_0/a < 1$. The exponential function is set to unity in this regime and the integration of the right-hand side of Eq. (2.24) is carried out directly. Hence

$$H^{plw}(x_0) = 3\varepsilon^2 \left(\frac{x_0}{a}\right)^4 \ll 1, \tag{2.25}$$

which reflects that caustics are not formed in this regime.

Suppose instead that the propagation distance is much greater than the correlation length, i.e. $x_0/a \gg 1$. We can then compute the analytical solution of the monitor in Eq. (2.24) by letting the range of integration go to infinity because the exponential in the integrand approaches zero for $r \gg a$. Thus

$$
\begin{aligned}
H^{plw}(x_0) &\approx 12\frac{\varepsilon^2}{a^4} \int_0^\infty (\frac{2}{3}x_0^3 - x_0^2 r + \frac{1}{3}r^3) \exp\left(-\left(\frac{r}{a}\right)^2\right) dr \\
&= 12\frac{\varepsilon^2}{a^4} \left(\frac{\sqrt{\pi}a x_0^3}{3} - \frac{a^2 x_0^2}{2} + \frac{a^4}{6}\right) \\
&\approx 4\sqrt{\pi}\varepsilon^2 \left(\frac{x_0}{a}\right)^3.
\end{aligned}
\tag{2.26}
$$

We have made use of the assumption that $x_0/a \gg 1$ to eliminate the last two terms in the brackets of Eq. (2.26). Let L denote the source-receiver offset. We then derive the non-dimensional number L/a from Eq. (2.26) in the case that caustics develop at $x_0 < L$. Hence by using $H^{plw}(L) \geq 1$, we get that

$$\frac{L}{a} \geq \frac{\varepsilon^{-2/3}}{(4\sqrt{\pi})^{1/3}} = 0.52\varepsilon^{-2/3}. \tag{2.27}$$

For a point source the generation of caustics can be evaluated along similar lines. The monitor $H^{ps}(x_0)$ is defined in the same way as the monitor for plane waves except that the condition for caustics formation in Eq. (2.8) for point sources is applied. Thus

$$
\begin{aligned}
H^{ps}(x_0) &\equiv \left< \left(\frac{1}{x_0}\frac{\partial q}{\partial \varphi}\right)^2 (x_0) \right> \\
&= \frac{1}{x_0^2 u_0^2} \int_0^{x_0} \int_0^{x_0} G(x_0, x')G(x_0, x'')\frac{1}{x'x''} \\
&\quad \times \left< \frac{\partial^2}{\partial \varphi^2}u_1(x') \frac{\partial^2}{\partial \varphi^2}u_1(x'') \right> dx'dx''.
\end{aligned}
\tag{2.28}
$$

According to Eq. (2.8) caustics develop at the offset x_0 when the monitor in Eq. (2.28) is equal to one. The mean value $\left< \frac{\partial^2}{\partial \varphi^2}u_1(x') \frac{\partial^2}{\partial \varphi^2}u_1(x'') \right>$ is related to $\left< \frac{\partial^2}{\partial z^2}u_1(x') \frac{\partial^2}{\partial z^2}u_1(x'') \right>$ by using the chain rule that

$$\frac{\partial}{\partial z} = \frac{\partial \varphi}{\partial z}\frac{\partial}{\partial \varphi} = \frac{1}{x}\frac{\partial}{\partial \varphi}, \tag{2.29}$$

because $z = x\varphi$ for small values of φ. Thus

$$< \frac{\partial^2}{\partial\varphi^2}u_1(x')\frac{\partial^2}{\partial\varphi^2}u_1(x'') >= (x'x'')^2 < \frac{\partial^2}{\partial z^2}u_1(x',z)\frac{\partial^2}{\partial z^2}u_1(x'',z) > \bigg|_{z=z_0} \qquad (2.30)$$

The procedure used for the derivation of the monitor for plane waves is repeated for the monitor for point sources. The only difference from the previous example is that the function $\eta(x',x'') = G(x_0,x')G(x_0,x'')x'x'' = x_0^2 x'x'' + (x'x'')^2 - x_0(x' + x'')x'x''$. The final result of the rather long derivation of the monitor for caustic formation in the point source case is given by

$$H^{ps}(x_0) = 12\frac{\varepsilon^2}{a^4}\int_0^{x_0}(\frac{1}{15}x_0^3 - \frac{4}{3}x_0r^2 + \frac{4}{3}r^3 + \frac{7}{15}\frac{r^5}{x_0^2})\exp\left(-\left(\frac{r}{a}\right)^2\right)dr. \qquad (2.31)$$

By letting x_0 go to zero it can be shown that $H^{ps}(0) = 0$.

Similar to Eq. (2.25), it can easily be shown that triplications due to point source wavefields do not generate when the length-scale of heterogeneity is greater than the source-receiver distance. Assume instead that $x_0/a \gg 1$ and carry on exactly as in the case of incident plane waves. The analytical expression of the right-hand side of Eq. (2.31) is given by

$$H^{ps}(x_0) = \frac{2\sqrt{\pi}}{5}\varepsilon^2\left(\frac{x_0}{a}\right)^3. \qquad (2.32)$$

The non-dimensional number L/a for the condition that caustics develop in the recorded wavefield is derived from Eq. (2.32), thus the condition that $H^{ps}(L) \geq 1$ gives that

$$\frac{L}{a} \geq \left(\frac{5}{2\sqrt{\pi}}\right)^{1/3}\varepsilon^{-2/3} = 1.12\varepsilon^{-2/3}. \qquad (2.33)$$

It is instructive to compare Eq. (2.27) for plane waves and Eq. (2.33) for point sources with estimates obtained by White *et al.* (1988). They use limit theorems for stochastic differential equations on the equation of dynamic ray tracing in Gaussian random media to calculate the probability that a caustic occurs at a certain propagation distance. In Fig. 4 and 5 of White *et al.* (1988), they demonstrate universal curves for the probability of caustic formation as a function of the universal distance defined as

$$\tilde{\tau} = (8\pi)^{1/6}\varepsilon^{2/3}\frac{L}{a}, \qquad (2.34)$$

where we have made a change of symbol from White *et al.* (1988) by using ε for the rms value of relative slowness perturbations and L for the propagation distance of the wavefield. This means that in the theory of White *et al.* (1988) caustics develop when the non-dimensional number L/a is given by

$$\frac{L}{a} = \frac{\tilde{\tau}}{(8\pi)^{1/6}}\varepsilon^{-2/3}. \qquad (2.35)$$

This expression has the same dependence on ε as the condition for caustics in Eq. (2.27) and (2.33).

According to Fig. 4 and 5 of White *et al.* (1988) the highest probability for generation of caustics for plane waves is found for $\tilde{\tau} = 0.9$ and for point sources $\tilde{\tau} = 1.9$. By inserting the appropriate value of $\tilde{\tau}$ into the factor $\tilde{\tau}/(8\pi)^{1/6}$ from Eq. (2.35), we find that the factor is 0.53 and 1.11 for the case of plane waves and point sources, respectively. Comparing these two numbers with the corresponding factors in Eq. (2.27) and (2.33), we see that there is a good agreement between the work of White *et al.* (1988) and our work.

Although we have derived the condition for caustics due to plane waves and point sources in two dimensions, the theory for caustics can be generalised to three dimensions. In 3-D, the equation for the ray perturbations q_1 and q_2 in the directions perpendicular to the ray decouples for a homogeneous reference model and a coordinate system that does not rotate around the reference ray (see Eq. (50) of Snieder and Sambridge, 1992). The condition for caustics in Eq. (2.2) and (2.8) for plane waves and point sources, respectively, can be applied to the ray perturbation in two orthogonal directions separately. For example as it is shown in appendix B, the non-dimensional number L/a for the point focus in 3-D Gaussian random media is given by Eq. (2.27) for plane waves and by Eq. (2.33) for point sources. Notice that in 3-D a caustic is not necessarily the same as a point focus. A caustic can in that case also be a line of focus points, whereas a focus point, as the word says, is located at a point.

2.3   Numerical examples

In this section, numerical examples of caustic formation of plane wavefields are shown for two distinct media; A 1-D medium with the slowness perturbation field described by $u_1(z) = \sqrt{2}\varepsilon u_0 \sin((z+z_0)^4/k)$, and a 2-D Gaussian random medium with the slowness perturbation field described by Eq. (2.13). The quantity u_0 is the reference slowness which is constant for all numerical experiments shown in this paper. The rms value of relative slowness fluctuations is denoted by ε. The parameters z_0, k and ε are adjusted such that the development of triplications in the media is significant.

In Fig. 2.2a, the 1-D slowness medium with $z_0 = 350$ m, $k = 1.5 \times 10^{10}$ m^4, $u_0 = 2.5 \times 10^{-4}$ s/m and $\varepsilon = 0.035$ is plotted. It is seen in that figure that the slowness field changes more and more rapidly with increasing z. In Fig. 2.2b, the focal distance of a plane wavefield propagating in the 1-D slowness medium as shown in Fig. 2.2a is computed by using Eq. (2.11). The offset from the source position is plotted on the abscissa while the depth at which caustics start to develop is plotted on the ordinate. The focal distance of the converging, plane wavefield is shown with the solid line. Notice that there are zones with defocusing of the plane wavefield which is manifested in Fig. 2.2b between 120 m and 205 m, between 265 m and 305 m, between 350 m and 380 m, etc... In these zones the wavefield propagates through a zone with a positive curvature of the relative slowness perturbation, so caustics do not develop. Thus the focal distance is infinite. The curvature of the relative slowness fluctuations increases with increasing z, so the focal distance of the converging wavefield decreases as depth increases.

a)   Slowness (10^{-4} s/m)   b)   Focal distance (m)
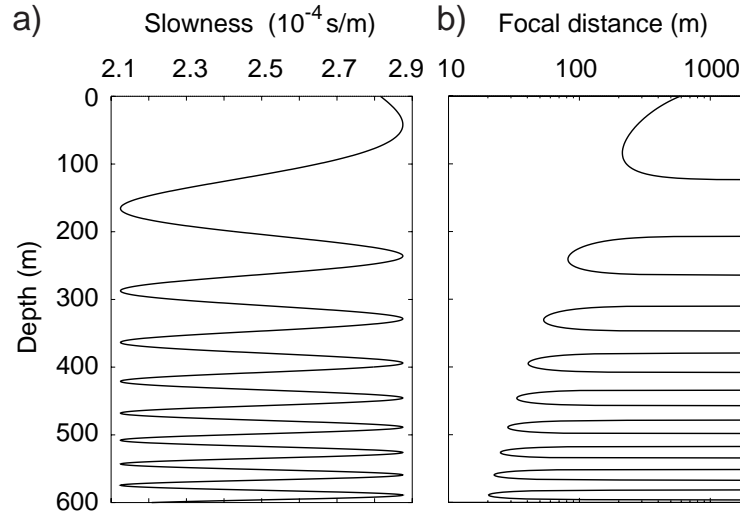
Figure 2.2: *The 1-D slowness field with ε = 0.035 is shown in a). The focal distance (solid line) of a plane wavefield is calculated as function of depth in b). Notice that the incoming plane wavefield is focusing in regions with positive slowness perturbations and it is being defocused when the slowness perturbation is negative.*

In Fig. 2.3, snapshots of a plane wavefield propagating through the 1-D slowness per-turbation field with the same value of z_0, k, u_0 and ε as for the 1-D medium in Fig. 2.2a are shown. The snapshots are produced with a finite difference solution of the acoustic wave equation. The central frequency is 1000 Hz, and the applied source function is a Ricker wavelet. The snapshots are taken for every 5 ms with the first snapshot at the source position and the last snapshot at about 100 m offset. Positive amplitudes are dark while negative amplitudes are bright. The first triplications are visible in the snapshot at $t = 10$ ms (~ 40 m) at depths below 500 m as the wavefield contains large positive amplitudes. In the snapshots for $t = 15$ ms (~ 60 m), 20 ms (~ 80 m) and 25 ms (~ 100 m), the trip-lications generated in the wavefield are very clear as they give rise to a half bowtie-form wave after the ballistic wavefront. Comparing the theoretically predicted minimum focal distance of the converging wavefield in Fig. 2.2b with the offset at which triplications start to develop in the wavefield in Fig. 2.3, we find that there is good agreement between the presented theory for caustic formation and the numerical 1-D experiment.

In Fig. 2.4, snapshots of a plane wave propagating in a 2-D Gaussian random medium with the reference slowness $u_0 = 2.5 \times 10^{-4}$ s/m, the relative slowness fluctuation ε = 0.025 and the correlation length $a = 7.1$ m are presented. The central frequency is 1000 Hz, while the Ricker wavelet is applied as source impulse. The 10 snapshots are com-puted for every 2.5 ms, where the first snapshot is taken at the initial wavefront and the last snapshot is taken at about 90 m offset. In the upper and lower part of the plane wave-
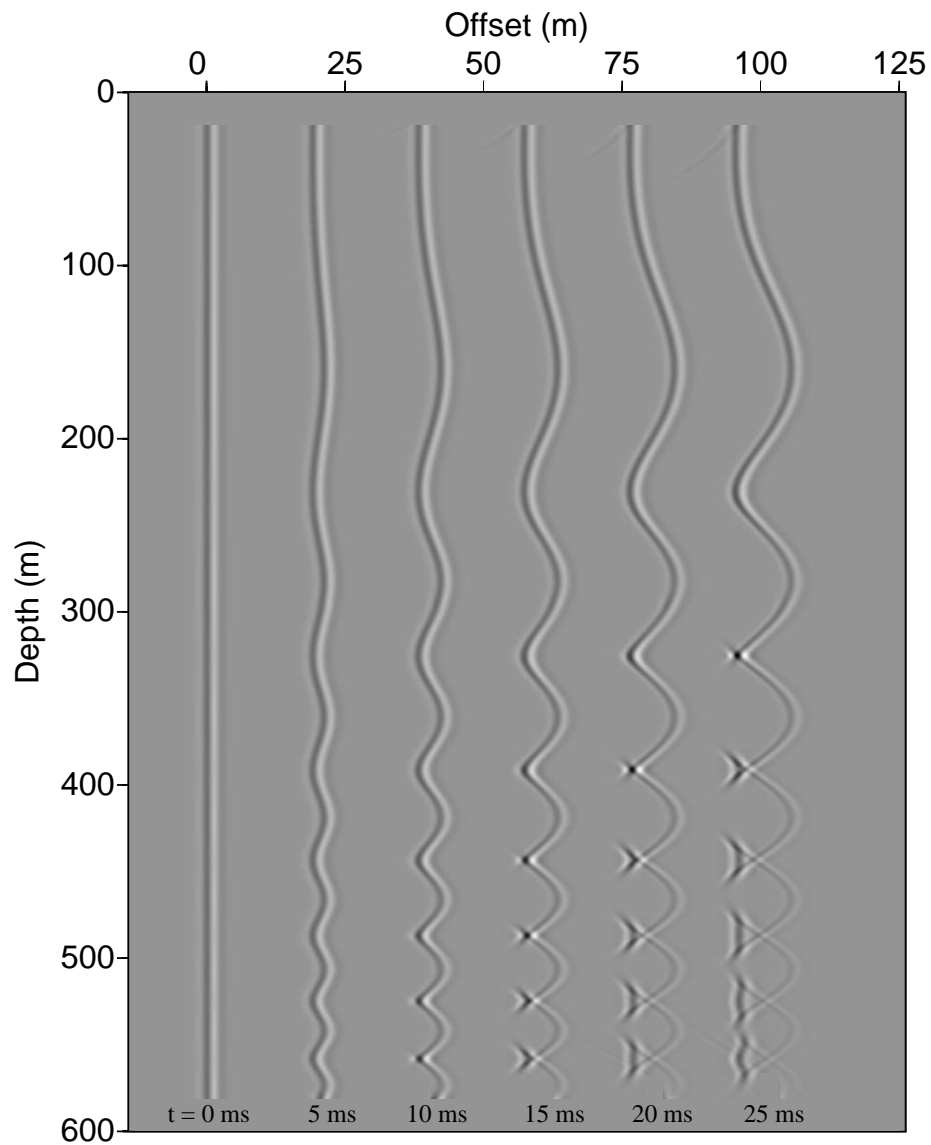
Figure 2.3: *Snapshots of plane wave propagation in the 1-D slowness perturbation model with ε = 0.035. The absolute travel times t = 0, 5, 15, 20, 25 ms are marked at the respective wavefronts. Caustics become very clear after the ballistic wavefronts for t = 15, 20, 25 ms.*

Offset (m)
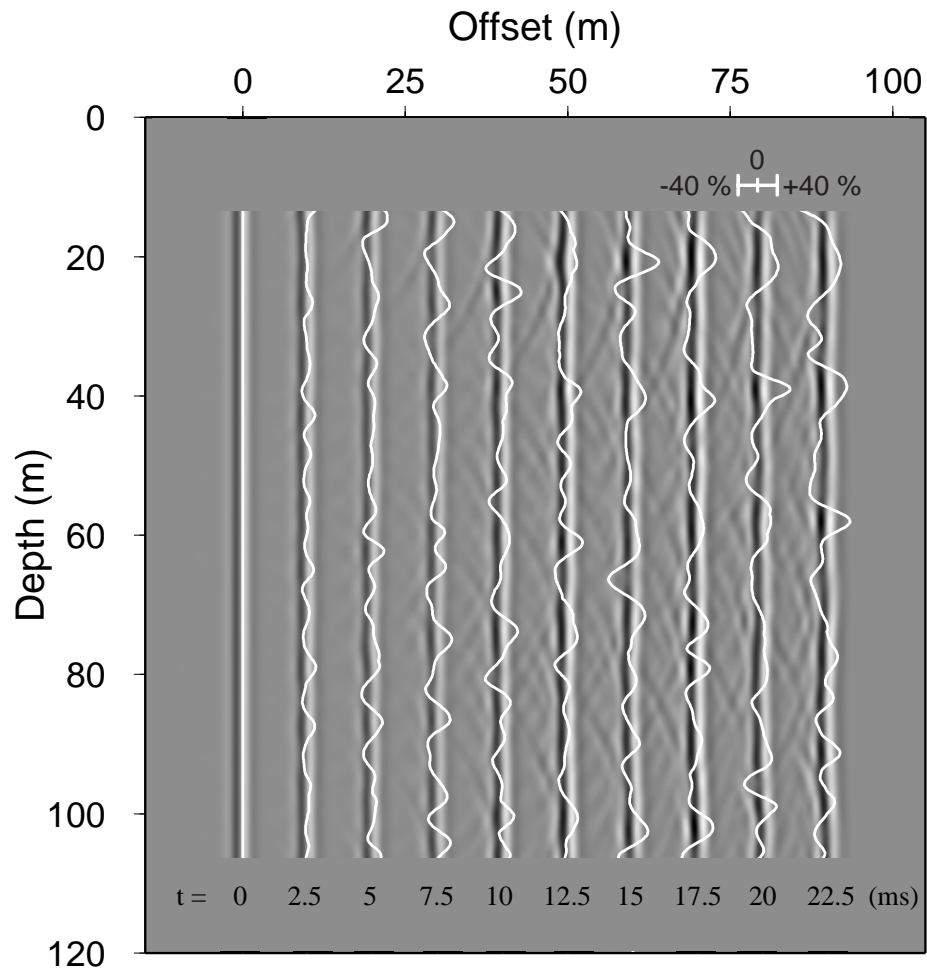
Figure 2.4: *Snapshots of plane wave propagation in the 2-D Gaussian random model with ε = 0.025 and a = 7.1 m. The absolute travel times t = 0, 2.5, 5, 7.5, 10, 12.5, 15, 17.5, 20, 22.5, 25 ms are marked at the respective wavefronts. Caustics develop in the wavefields for t larger than or equal to 7.5 ms. The maximum amplitude variation along the wavefield for each wavefront is shown with the white solid line. Notice that the colour in the wavefronts gets darker when the maximum amplitude is at a peak. The bar in the upper right corner shows the percentage variation of the maximum amplitude in the perturbed slowness model compared with the reference amplitude computed in the constant reference slowness model.*

fronts in Fig. 2.4, a circular wave due to diffraction at the edge of the numerical grid can be seen. Inserting the appropriate value for ε into Eq. (2.27) the non-dimensional number $L/a = 6.1$ for the development of triplications in the Gaussian random medium is found. The expectation value of the offset at which caustics start to generate is then $L = 43$ m for $a = 7.1$ m. In Fig. 2.4, no triplications are observed in the wavefront at $t = 0$ ms, 2.5 ms and 5 ms, i.e. at approximately 0 m, 10 m, and 20 m, respectively. Then for $t = 7.5$ ms (~ 30 m) and 10 ms (~ 40 m) the multipathing that is associated with the formation of caustics can be seen as a minor wavefield after the ballistic wavefront. This generation of minor wavefields delayed compared to the ballistic wavefront is neither due to uncertainties in the FD-code or due to scattering effects (for the employed wave $\lambda/a \approx 0.5$) but because of caustic formation. For the last 5 snapshots at $t = 12.5$ ms (~ 50 m), 15 ms (~ 60 m), 17.5 ms (~ 70 m), 20 ms (~ 80 m) and 22.5 ms (~ 90 m) triplications are developing rather strongly after the wavefront. The maximum amplitude variation along the wavefield for each wavefront is plotted with the white solid line in Fig. 2.4. For the initial wavefront at $t = 0$ ms, the amplitude is constant, while the maximum amplitude along the wavefield varies with increasing extrema for the wavefronts for larger t. The bar in the upper right corner of Fig. 2.4 shows the relative percentage of the amplitude variations in the perturbed slowness model compared with the reference amplitude computed for the homogeneous reference slowness model. Notice that the largest positive values of the maximum amplitude along the wavefronts correspond to the parts of the wavefronts with darkest colour while the negative amplitude variations are shown with bright colours.

Witte *et al.* (1996) use the kinematic ray-tracing equation to construct a ray-diagram for a Gaussian random medium with fixed $\varepsilon = 0.03$, but with different values of the correlation length a. Using Eq. (2.27) with $\varepsilon = 0.03$, gives the non-dimensional number $L/a = 5.4$. Looking at the top panel in Fig. 4 of Witte *et al.* (1996) for $L/a = 10$, it is seen that the first caustics generate at $z \approx 5\text{-}6$ which corresponds well with the theoretical value computed with Eq. (2.27).

2.4   Conclusions

In this paper, we develop a theory for the formation of caustics. The theory is based on ray perturbation theory, but is equivalent to a similar approach by White *et al.* (1988) where the equation of dynamic ray tracing is used to predict when triplications develop in Gaussian random media.

We have applied the theory for the generation of caustics in two case studies (i.e. 1-D slowness perturbations fields and 2-D Gaussian random media) where the plane wave source and the point source are taken into account. The theory for caustic formation can be generalised to wavefields propagating in 3-D. We find that the formation of caustics for 1-D slowness perturbation fields depends on the inverse of the square root of the second derivative of the relative slowness perturbation, while for Gaussian random media the formation of caustics is dependent upon the relative slowness perturbation in a power of minus two thirds.

References

Aki K. and Richards P. G. (**1980**). *Quantitative seismology: theory and methods* (W. H. Freeman, San Francisco.).

Brown M. and Tappert F. D. (**1986**). Causality, caustics, and the structure of transient wavefields, J. Acoust. Soc. Am. **80**, 251-255.

Kravtsov Y. A. (**1988**). 'Rays and caustics as physical objects' in *Prog. in Optics*, XXVI, Edited by Wolf E. (Elsevier, Amsterdam), 227-348.

Menke W. and Abbot D. (**1990**). *Geophysical theory* (Columbia University Press, NY.).

Müller G., Roth M. and Korn M. (**1992**). Seismic-wave traveltimes in random media, Geophys. J. Int. **110**, 29-41.

Pulliam J. and Snieder R. (**1998**). Ray perturbation theory, dynamic ray tracing and the determination of Fresnel zones, Geophys. J. Int. **135**, 463-469.

Roth M., Müller and Snieder R. (**1993**). Velocity shift in random media, J. Geophys. Res. **115**, 552-563.

Snieder R. and Sambridge M. (**1992**). Ray perturbation theory for travel times and ray-paths in 3-D heterogeneous media, Geophys. J. Int. **109**, 294-322.

Witte O., Roth M. and Müller G. (**1996**). Ray tracing in random media, Geophys. J. Int. **124**, 159-169.

White B., Nair B. and Baylies A. (**1988**). Random rays and seismic amplitude anomalies, Geophysics. **53**, 903-907.

2.5   Appendix A: Derivation of Eq. (2.22)

In this appendix, the step from Eq. (2.21) to Eq. (2.22) is demonstrated. The right-hand side of Eq. (2.21) is written as

$$\int_0^{x_0} \int_0^{x_0} \eta(x', x'') f(|x' - x''|) dx' dx'', \tag{2.36}$$

where

$$f(|x' - x''|) = < \frac{\partial^2}{\partial z^2} u_1(x', z) \frac{\partial^2}{\partial z^2} u_1(x'', z) > \Big|_{z=z_0}, \tag{2.37}$$
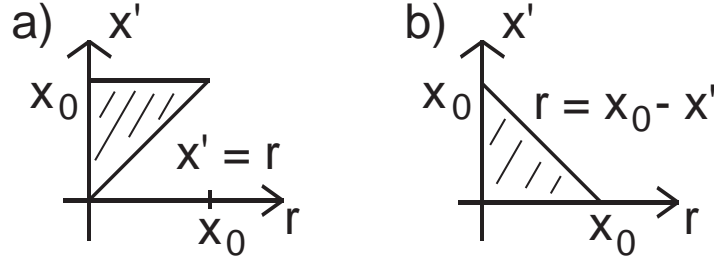
Figure 2.5: *The integration technique which is found in Roth et al. (1993). The area of integration for $\int_0^{x_0} dx' \int_0^{x'} \eta(x',x'-r)f(r)dr$ and $\int_0^{x_0} dx' \int_0^{x_0-x'} \eta(x',x'+r)f(r)dr$ in Eq. (2.41) is shown in a) and b), respectively.*

and

$$\eta(x',x'') = G(x_0,x')G(x_0,x''). \tag{2.38}$$

The integration over x'' in Eq. (2.36) is split into one integration over x'' from 0 to x' and another integration over x'' from x' to x_0. Thus Eq. (2.36) is rewritten as

$$\int_0^{x_0} dx' \left[\int_0^{x'} \eta(x',x'')f(x'-x'')dx'' + \int_{x'}^{x_0} \eta(x',x'')f(x''-x')dx'' \right]. \tag{2.39}$$

Define now $r = x' - x''$ and $r = x'' - x'$ for the first and second integration over x'' in the brackets of Eq.(2.39) and carry out a change of variables in the two integrations over x'' inside the brackets. The result is given by

$$\int_0^{x_0} dx' \left[-\int_{x'}^0 \eta(x',x'-r)f(r)dr + \int_0^{x_0-x'} \eta(x',x'+r)f(r)dr \right]. \tag{2.40}$$

or

$$\int_0^{x_0} dx' \left[\int_0^{x'} \eta(x',x'-r)f(r)dr + \int_0^{x_0-x'} \eta(x',x'+r)f(r)dr \right]. \tag{2.41}$$

The integration over x' multiplied with the first and second integration over r in the brackets of Eq. (2.41) corresponds to the triangle in the r-x' plane as shown in Fig. 2.5a and 2.5b, respectively. By changing the order of integration in Eq. (2.41), but still keeping in mind that the double integration over r and x' must be over the triangles as shown in Fig. 2.5a and 2.5b, it is possible to rewrite the Eq. (2.41) in the following way

$$\int_0^{x_0} dr \left[\int_r^{x_0} \eta(x',x'-r)f(r)dx' + \int_0^{x_0-r} \eta(x',x'+r)f(r)dx' \right]. \tag{2.42}$$
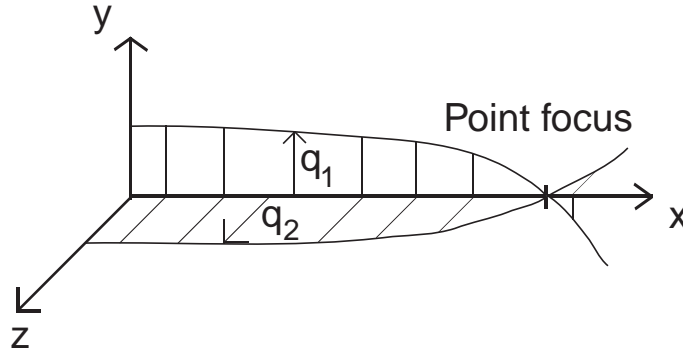
Figure 2.6: *Estimation of the point focus in a 3-D medium.*

After rearranging the term $f(r)$ outside the integration over x', the result is finally given by

$$\int_0^{x_0} dr f(r) \left[\int_r^{x_0} \eta(x', x'-r) dx' + \int_0^{x_0-r} \eta(x', x'+r) dx' \right], \tag{2.43}$$

which is the equation that is stated in Eq. (2.22).

2.6 Appendix B: Caustic formation in three dimensions

Imagine that a plane wavefield is propagating along the x-axis with the decoupled ray deflections q_1 and q_2 parallel to the y-axis and z-axis, respectively. See Fig. 2.6 for the experimental setup. Using the results from Snieder and Sambridge (1992), the decoupled differential equations for the ray deflection coordinates are then given by

$$\frac{d^2}{dx^2} q_i = \hat{q}_i \cdot \nabla \left(\frac{u_1}{u_0} \right), \tag{2.44}$$

where $i = 1, 2$. The ray deflections are gathered together in the ray deflection vector $\mathbf{q} = (0, q_1, q_2)$. The condition for caustic formation in Eq. (2.2) is applied on each ray deflection coordinate. Hence,

$$\nabla \mathbf{q}(x_0) = \begin{pmatrix} 0 \\ -1 \\ -1 \end{pmatrix}, \tag{2.45}$$

for a point focus at the offset x_0. In order to determine when caustics develop in a 3-D Gaussian random medium, the expectation value of $\nabla \mathbf{q}(x_0) \cdot \nabla \mathbf{q}(x_0)$ is computed. Thus

according to Eq. (2.45) for a point focus, caustics develop when

$$
\begin{aligned}
< \nabla \mathbf{q} \cdot \nabla \mathbf{q} > (x_0) \quad &= \quad < \left(\frac{\partial q_1}{\partial y} \right)^2 (x_0) + \left(\frac{\partial q_2}{\partial z} \right)^2 (x_0) > \\
&= \quad < \left(\frac{\partial q_1}{\partial y} \right)^2 (x_0) > + < \left(\frac{\partial q_2}{\partial z} \right)^2 (x_0) > = 2, \quad (2.46)
\end{aligned}
$$

at the offset x_0. For 2-D Gaussian random media, the following result is derived;

$$
H^{plw}(x_0) \equiv < \left(\frac{\partial q}{\partial z} \right)^2 (x_0) > = 1, \qquad (2.47)
$$

when a caustic develops at the offset x_0. According to Eq. (2.26), $H^{plw}(x_0) = 4\sqrt{\pi}\,\varepsilon^2$ $(x_0/a)^3$ for $x_0/a \gg 1$. This result can be used for each ray deflection q_i separately, so the monitors $H_1^{plw}(x_0)$ and $H_2^{plw}(x_0)$ for q_1 and q_2, respectively, are defined as

$$
H_1^{plw}(x_0) \equiv < \left(\frac{\partial q_1}{\partial y} \right)^2 (x_0) > \qquad \text{and} \qquad H_2^{plw}(x_0) \equiv < \left(\frac{\partial q_2}{\partial z} \right)^2 (x_0) >, \quad (2.48)
$$

where $H_1^{plw}(x_0) = H_2^{plw}(x_0) = 4\sqrt{\pi}\varepsilon^2 (x_0/a)^3$. Combining Eq. (2.46) with the monitors defined in Eq. (2.48), we compute

$$
H_1^{plw}(x_0) + H_2^{plw}(x_0) = 2, \qquad (2.49)
$$

or

$$
4\sqrt{\pi}\varepsilon^2 \left(\frac{x_0}{a} \right)^3 = 1, \qquad (2.50)
$$

for a caustic at the offset x_0 in a 3-D Gaussian random medium which is also the result found for 2-D Gaussian random media. Similarly, the result for caustic formation due to a point source in 3-D Gaussian random media is unaltered from the result in the 2-D case.

Chapter 3

The effect of small-scale heterogeneity on the arrival time of waves

Abstract.

Small-scale heterogeneity alters the arrival time of waves in a way that cannot by explained by ray theory. This is because ray theory is a high-frequency approximation that does not take the finite-frequency of wavefields into account. We present a theory based on the first-order Rytov approximation that predicts well the arrival time of waves propagating in media with small-scale inhomogeneity with a length-scale smaller than the width of Fresnel zones. In the regime for which scattering theory is relevant we find that caustics are easily generated in wavefields, but this does not influence the good prediction of finite-frequency arrival times of waves by scattering theory. The regime of scattering theory is relevant when the characteristic length of heterogeneity is smaller than the width of Fresnel zones. The regime of triplications is independent of frequency but it is more significant the greater the magnitude of slowness fluctuations.

3.1 Introduction

Ray theory is valid only if the wavelength of the waves and the associated widths of Fresnel zones are much smaller than the characteristic length of heterogeneity. For example, in geophysics when working with surface wave tomography it is common to use ray theoretical schemes, which offer a computational effective solution of the forward problem. This approximation, however, poses a problem from a theoretical point of view because the length-scale of inhomogeneity in high-resolution models is comparable to the widths

---

This chapter has been accepted for publication in *Geophys. J. Int.*, 2001.

of Fresnel zones (Passier and Snieder, 1995). Other domains where scattering is considered to be important are ocean acoustics (Kuperman *et al.*, 1998), medical imaging (Baba *et al.*, 1989; King and Shao, 1990) and non-destructive testing experiments (Haque *et al.*, 1999).

Several different approaches to scattering theory are reported in the literature. Marquering *et al.* (1998) describe how to calculate sensitivity kernels based on the first-order Born approximation and surface wave mode coupling. Marquering *et al.* (1999) develop a sensitivity kernel formulation of the perturbed traveltime starting with the cross-correlation function. Jensen and Jacobsen (1997) explain how a linearised inversion of time-distance helioseismic data is established by introducing an approximate Gaussian sensitivity kernel. Yomogida (1992) utilises the Born approximation and then the Rytov approximation to derive the sensitivity kernel. Woodward (1992) introduces the finite-frequency effect on wavepaths, and the concept of Rytov and Born wavepaths for transmitted, reflected and refracted wavefields are explained. Snieder and Lomax (1996) compute a frequency averaging function from the first-order Rytov approximation. Fehler *et al.* (2000) apply the Rytov approximation to simulate multiple forward wave scattering in Gaussian random media, and the results are compared with the ones from finite-difference solutions of the wave equation.

We follow the idea from Snieder and Lomax (1996) that the phaseshift of the scattered wavefield due to a perturbation of the medium can be expressed as the integration of a sensitivity kernel multiplied by the slowness perturbations over the complete model space. In addition to this, we transform the obtained phaseshift expression into a timeshift expression so that scattering theory is directly applicable to the interpretation of arrival time data.

Scattering theory includes non-ray-geometrical phenomena. In brief, time residuals due to scattering theory are altered by slowness perturbations surrounding the geometrical ray, and the maximum sensitivity to slowness perturbations is largest just besides the geometrical ray. In contrast, ray theoretical time delays are only sensitive to the slowness field on the ray path.

The regime of scattering theory is determined from a 2-D numerical experiment wherein the frequency of the waves, the magnitude of slowness perturbations, the offset of the receivers and the length-scale of the slowness perturbation field are controlled. We compare the residual times for ray theory and scattering theory with time delays computed with a finite-difference solution of the acoustic wave equation. Because we have control over the parameters in the numerical experiment, the regimes of ray theory, scattering theory and triplications are investigated. Furthermore, we show with another 2-D numerical experiment that the regimes of scattering theory and triplications remain valid in a more complex medium (namely Gaussian random media).

In addition, we show that triplications are easily generated in wavefields if the slowness perturbations are sufficiently large. Though the scattering approach is based on a linearisation of the phase (i.e. the first-order Rytov approximation), the 'observed' time delays estimated from wavefields with caustics are well predicted by scattering theory.

In section 3.2, we explain how to derive the width of Fresnel zones, the focal length of converging 2-D wavefields, and the timeshifts due to ray theory and scattering theory.

In section 3.3, we go through the numerical experiment that is used to determine the regime for scattering theory, and present the experiment for models of Gaussian random media. In section 3.4, we summarise the results of the numerical experiments and define the different regimes of ray theory, scattering theory and triplications. In section 3.5, we give examples, taken from global seismology, ocean acoustic and medical imaging, where scattering theory is important. Conclusions are drawn in section 3.6.

3.2   Theory

In this section, we present the theory applied to investigate the influence of small-scale heterogeneity on travel times. The theory is derived for two distinct source geometries: the plane wave (plw) source, and the point source (ps). First, we derive the width of Fresnel zones. Then we discuss the focal length of converging wavefields in 2-D slowness perturbation fields. Finally, we deduce the first-order and second-order linearised ray theory and the first-order linearised scattering theory for 2-D experiments.

3.2.1   The width of Fresnel zones

Fresnel zones are defined in terms of the difference in propagation path lengths for rays with nearby paths. All points of a ray taking a detour compared with the ballistic ray are inside the Fresnel zone if the difference in length of propagation paths for the ballistic ray and the detour ray is less or equal than a certain fraction of the wavelength λ (e.g. Kravtsov, 1988). This is the first Fresnel zone, which physically signifies constructive interference of the scattered wavefield produced by single-point scatterers inside the Fresnel zone. We prefer to keep the formulas as general as possible, so the Fresnel zone is defined as the set of points that give single scattered waves with a detour smaller than the wavelength divided by a number n.

Let $x \in [0;L]$ denote the ballistic propagation distance between the source and the receiver, with the source-receiver separation indicated by L. For a plane wave in a homogeneous medium, the detour d is

$$d = \sqrt{(L-x)^2 + q^2(x)} + x - L, \tag{3.1}$$

where $q(x)$ is the perpendicular distance to the geometrical ray at position x along the ray. The Fresnel zone condition is that $d \leq \lambda/n$. To estimate the boundary of Fresnel zones, we use the sign of equality in the Fresnel zone condition. To leading order in $q(x)/(L-x)$, the perpendicular distance from the ballistic ray is then isolated from Eq. (3.1) as

$$q(x) = \sqrt{\frac{2\lambda(L-x)}{n}}. \tag{3.2}$$

The width W^{plw} of the Fresnel zone is twice the perpendicular distance from the ballistic

ray. Hence,

$$W^{plw}(x) = \sqrt{\frac{8\lambda(L-x)}{n}}.$$ (3.3)

The maximum width $L_F^{plw} = \sqrt{8\lambda L/n}$ is obtained at the initial wavefront ($x = 0$), while the width of Fresnel zones for plane waves to first order of approximation goes to zero at the receiver position ($x = L$).

The width of Fresnel zones for point sources in homogeneous media is calculated in the same way as in the plane wave case. The detour is

$$
\begin{aligned}
d &= \sqrt{(L-x)^2 + q^2(x)} + \sqrt{x^2 + q^2(x)} - L \\
&\approx \frac{1}{2}q^2(x)\frac{L}{(L-x)x}.
\end{aligned}
$$ (3.4)

The Fresnel zone condition is again used to compute the width of Fresnel zones. Hence,

$$W^{ps}(x) = \sqrt{\frac{8\lambda x(L-x)}{nL}},$$ (3.5)

which is maximum at $x = L/2$. The maximum width $L_F^{ps} = \sqrt{2\lambda L/n}$. Notice that $L_F^{ps} = L_F^{plw}/2$.

For Eq. (3.3) and (3.5), the reference medium is homogeneous which means that ray bending is not taken into account. However, it is possible to compute the boundary of Fresnel zones in heterogeneous media as well (Pulliam and Snieder, 1998). In addition, the formulas for the Fresnel zone in Eq. (3.3) and (3.5) are obtained by using first order perturbation theory. The exact solution of the Fresnel zone in a homogeneous medium for a point source is an ellipse with the source and the receiver in the two foci, and for a plane wave the Fresnel zone is a semi-ellipse with the receiver in the focus point. For low-frequency waves, the backscattering field near the source and receiver may be rather large, so Eq. (3.3) and (3.5) are inaccurate close to these points.

3.2.2   Estimation of caustics in 2-D slowness perturbation fields

We discuss in this section at which point caustics, also called triplications, start to develop in the special case of a slab with a perturbed slowness field depending only on depth and in the general case of Gaussian random media. The general theory for the formation of caustics is explained thoroughly in Spetzler and Snieder (2001).

First, we consider the case that caustics develop when an initially plane wave propagates in the x-direction through a slab with a depth-dependent slowness field $u_1(z)$. The setup of this experiment is shown in Fig. 3.1. The vertical slab is at the offset x_l from the source, and the slab width is denoted W. The slowness field to the left of and to the right of the slab is set to the constant reference slowness field u_0.

First of all, it is assumed that caustics are developing before the ballistic wavefield leaves the slab. We use Eq. (6) in Spetzler and Snieder (2001), where the integration
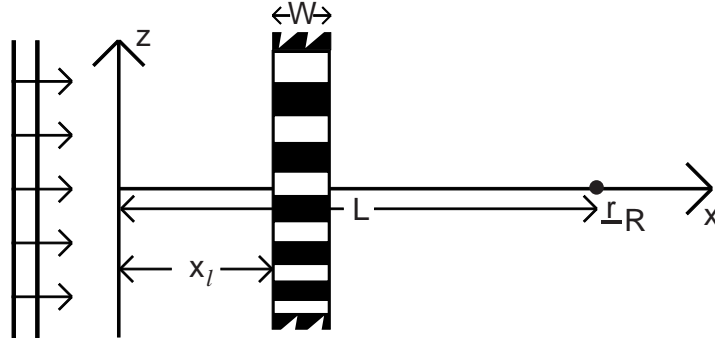
Figure 3.1: *Explanation of the variables used in the experiment with a vertical slab of heterogeneity. A plane wave is incident from the left.*

along the reference ray is carried out from x_l to x_{caus} (for $x_{caus} - x_l \leq W$), to determine when caustics form inside the slab. Hence,

$$x_{caus}(z) \quad = \quad x_l + \sqrt{\frac{-2}{\frac{\partial^2}{\partial z^2}\left(\frac{u_1}{u_0}\right)(z)}}. \qquad \text{(Inside slab)} \qquad (3.6)$$

If triplications develop after the waves pass the slab (i.e. $x_{caus} > x_l + W$), then the propagation length of plane wavefields at which caustics start to occur is

$$x_{caus}(z) = x_l + \frac{1}{2}W - \frac{1}{W\frac{\partial^2}{\partial z^2}\left(\frac{u_1}{u_0}\right)(z)}. \qquad \text{(After slab)} \qquad (3.7)$$

Let the distance between the source and receiver be denoted L. If $x_{caus}(z) < L$, triplications will be present in the recorded wavefield.

Next, we discuss the formation of triplication in Gaussian random media. The auto-correlation function of a Gaussian random medium is given by

$$< u_1(\mathbf{r}_1)u_1(\mathbf{r}_2) > = (\varepsilon u_0)^2 e^{-(r/a)^2}, \qquad (3.8)$$

where ε is the rms value of the relative slowness perturbation fluctuations, a denotes the auto-correlation length (or roughly the length-scale of slowness perturbations) and $r = |\mathbf{r}_1 - \mathbf{r}_2|$.

Spetzler and Snieder (2001) show for an incoming plane wave in Gaussian random media that the formation of caustics is significant when

$$\frac{L}{a} \geq 0.52\varepsilon^{-2/3}, \qquad (3.9)$$

with the source-receiver distance denoted L. For wavefields emitted by point sources in Gaussian random media, the non-dimensional number L/a for the condition that triplications develop in the recorded wavefield is given by

$$\frac{L}{a} \geq 1.12\varepsilon^{-2/3}, \tag{3.10}$$

(see Spetzler and Snieder, 2001).

   The conditions for the formation of caustics in Eq. (3.9) and (3.10) are independent of the wavelength but they depend on the rms value of relative slowness fluctuations.

3.2.3   Timeshift derivations

We apply two approaches to derive the residual times in a 2-D isotropic, perturbed slowness medium. First, we explain how the time delay due to first-order and second-order ray perturbation theory is estimated. Second, we show how the timeshift based on first-order linearised scattering theory can be written as a linear function of the 2-D slowness perturbation field. Third, we discuss the properties of the scattering theory.

The ray geometrical timeshift

According to second-order ray perturbation theory (e.g. Snieder and Sambridge, 1992), the travel time is the sum of three components, namely

$$T = T_0 + T_1 + T_2. \tag{3.11}$$

T_0 is the contribution from the reference ray in the reference medium, T_1 is the timeshift due to the slowness perturbation field along the reference ray (based on Fermat's principle) and the term T_2 is a more complicated expression that accounts for the deflection of the ray by the slowness perturbation. A complete explanation of how to calculate T_2 is given in Snieder and Sambridge (1992).

   In the numerical experiment presented here, we compute the ray-theoretical time delay δt due to a perturbed slowness medium to first order. This implies that the timeshift is expressed as a linear function of the slowness anomaly $u_1(\mathbf{r})$ along the reference ray. Hence

$$\begin{aligned} \delta t &= T_1 \\ &= \int_{\text{Ref ray}} u_1(\mathbf{r})ds. \end{aligned} \tag{3.12}$$

In our experiment the reference slowness is constant, so the reference ray is a straight line between the source and receiver.

   In the numerical examples shown here the second-order travel-time perturbation T_2 is much smaller than the first-order travel time perturbation T_1. For this reason the first-order travel time perturbation is used for the ray-geometrical travel time.

Ray theory is valid when the characteristic length a of heterogeneity is much larger than both the wavelength λ and the width of Fresnel zones L_F. Hence in non-dimensional numbers, the condition for ray theory is written as

$$\frac{\lambda}{a} \ll 1, \qquad \text{and} \qquad \frac{L_F}{a} \ll 1. \tag{3.13}$$

See Menke and Abbot (1990).

Single-scattering theory

We show that the time perturbation $\langle \delta t \rangle(L)$ for the receiver at the offset L is written as an integration over the slowness perturbation field $u_1(x,z)$ multiplied by a sensitivity kernel $K(x,z)$:

$$\langle \delta t \rangle(L) = \int_{-\infty}^{\infty} \int_{0}^{L} u_1(x,z) K(x,z) dx dz. \tag{3.14}$$

The first-order perturbation of the phase of the wavefield follows from the Rytov approximation. The unperturbed wavefield is denoted by p_0. The Born approximation gives the first-order perturbation p_1 of the wavefield. According to Beydoun and Tarantola (1988) and Snieder and Lomax (1996), the phaseshift $\delta \varphi$ in the frequency-domain is given by

$$\delta \varphi = Im\{\frac{p_1}{p_0}\}, \tag{3.15}$$

The condition for the validity of the Rytov approximation for transmitted waves is that $k_0 L (u_1/u_0)^2 \ll 1$, where k_0 is the wavenumber. Comparing this condition with the condition for the Born approximation for transmitted waves $k_0 L u_1/u_0 \ll 1$ (Snieder and Lomax, 1996), we see that the Rytov approximation has validity for a larger slowness perturbation parameter than does the Born approximation for transmitted waves.

Snieder and Lomax (1996) demonstrated that the Born approximation to the solution of the acoustic wave equation with constant density is

$$p_1(\underline{r}_R, \omega) = \omega^{3/2} \sqrt{\frac{u_0}{2\pi}} e^{i\frac{\pi}{4}} \int_{V} \frac{u_1(\underline{r})}{\sqrt{|\underline{r}_R - \underline{r}|}} p_0 e^{ik_0 |\underline{r}_R - \underline{r}|} d^2\underline{r}, \tag{3.16}$$

for an incident plane wave that is given by $p_0 = \exp(ik_0 x)$. The volume for the integration in Eq. (3.16) is denoted by V. The receiver is at the position (L, z_j). We assume that $(z - z_j)/(L-x) \ll 1$, and set $|\underline{r}_R - \underline{r}|$ and $1/\sqrt{|\underline{r}_R - \underline{r}|}$ to the first order and zeroth order Taylor approximation, respectively (Snieder and Lomax, 1996), see Fig. 3.2 for a definition of the geometric variables.

$$|\underline{r}_R - \underline{r}| \approx (L-x) + \frac{(z-z_j)^2}{2(L-x)}, \qquad \text{and} \qquad \frac{1}{\sqrt{|\underline{r}_R - \underline{r}|}} \approx \frac{1}{\sqrt{L-x}}. \tag{3.17}$$
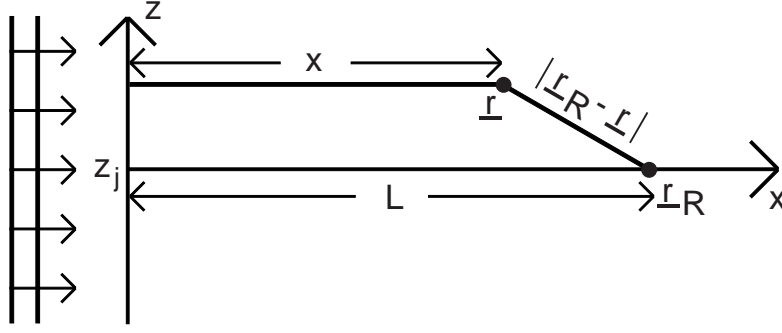
Figure 3.2: *Definition of the geometric variables for an incoming plane wave in a 2-D medium with a constant reference slowness.*

We insert these two small-angle approximations in Eq. (3.16), and define the full-space integration as a double integration going from 0 to L for the offset x and from $-\infty$ to ∞ for the perpendicular distance z from the geometrical ray.

$$p_1(\underline{r},\omega) = \omega^{3/2}\sqrt{u_0/(2\pi)}\,e^{i\pi/4}e^{ik_0L}\int_0^L \frac{1}{\sqrt{L-x}}\int_{-\infty}^{\infty} u_1(x,z)e^{ik_0\frac{(z-z_j)^2}{2(L-x)}}\,dzdx. \quad (3.18)$$

Using Eq. (3.15) the phaseshift at the receiver position (L,z_j) is then given by

$$\delta\varphi(L,\omega) = \omega^{3/2}\sqrt{\frac{u_0}{2\pi}}\int_{-\infty}^{\infty}\int_0^L u_1(x,z)\frac{\sin\left(k_0\frac{(z-z_j)^2}{2(L-x)}+\frac{\pi}{4}\right)}{\sqrt{L-x}}\,dxdz. \quad (3.19)$$

So far all the calculations in this section are done in the frequency domain. In spite of this, we can express the linearised phase perturbation as a linearised time delay, supporting this statement by mathematically representing waves as $A(\omega)\exp(i\varphi(\omega))$, where the amplitude $A(\omega)$ and the phase $\varphi(\omega) = \omega t$ depend on the angular frequency ω. The phaseshift is then expressed as

$$\delta\varphi = \omega\delta t, \quad (3.20)$$

where δt is the time perturbation which is a function of frequency. Hence, the theoretical timeshift due to single-scattering is

$$\delta t(L,\omega) = \sqrt{\frac{u_0\omega}{2\pi}}\int_{-\infty}^{\infty}\int_0^L u_1(x,z)\frac{\sin\left(k_0\frac{(z-z_j)^2}{2(L-x)}+\frac{\pi}{4}\right)}{\sqrt{L-x}}\,dxdz. \quad (3.21)$$

Wavefields are never monochromatic so we need to frequency-average the timeshift. For example, the time perturbation can be calculated for a frequency-band in the range

from $\nu_0 - \Delta\nu$ to $\nu_0 + \Delta\nu$, where ν_0 is the central frequency and $\Delta\nu$ is the half width of the frequency-band. Moreover to account for the variation of the frequency spectrum in the range of frequency integration, we introduce the normalised amplitude spectrum $A(\nu)$ of the recorded wavefield. The normalisation condition for the amplitude spectrum is that $\int_{\nu_0-\Delta\nu}^{\nu_0+\Delta\nu} A(\nu)d\nu = 1$. The frequency-band averaged timeshift is calculated as

$$
\begin{aligned}
\langle \delta t \rangle (L) &= \int_{\nu_0-\Delta\nu}^{\nu_0+\Delta\nu} A(\nu)\delta t(L,\nu)d\nu \\
&= \int_{-\infty}^{\infty} \int_0^L u_1(x,z)\sqrt{u_0} \int_{\nu_0-\Delta\nu}^{\nu_0+\Delta\nu} A(\nu)\sqrt{\nu} \\
&\quad \times \frac{\sin\left(\pi\nu u_0 \frac{(z-z_j)^2}{(L-x)} + \frac{\pi}{4}\right)}{\sqrt{L-x}}d\nu dx dz.
\end{aligned}
\tag{3.22}
$$

Comparing Eq. (3.22) with Eq. (3.14), we identify the sensitivity kernel for an incoming, plane wave as

$$
K^{plw}(x,z) = \sqrt{u_0} \int_{\nu_0-\Delta\nu}^{\nu_0+\Delta\nu} A(\nu)\sqrt{\nu} \frac{\sin\left(\pi u_0\nu \frac{(z-z_j)^2}{(L-x)} + \frac{\pi}{4}\right)}{\sqrt{L-x}}d\nu.
\tag{3.23}
$$

For point sources, the sensitivity kernel in Eq. (3.23) is modified by taking the point-source geometry into account. For a point source in a 2-D medium, the solution to the zeroth-order wavefield using the far-field approximation is given by $p_0 = -(1/\sqrt{8\pi kr})\exp i(kr + \pi/4)$, where k is the wavenumber and r is the propagation length. This solution for the source geometry contains the geometrical spreading factor $1/\sqrt{r}$ yielding the sensitivity kernel for a point source,

$$
K^{ps}(x,z) = \sqrt{u_0 L} \int_{\nu_0-\Delta\nu}^{\nu_0+\Delta\nu} A(\nu)\sqrt{\nu} \frac{\sin\left(\pi u_0\nu L \frac{(z-z_j)^2}{x(L-x)} + \frac{\pi}{4}\right)}{\sqrt{x(L-x)}}d\nu.
\tag{3.24}
$$

The properties of the sensitivity kernel

The sensitivity kernels for plane waves in Eq. (3.23) and for point sources in Eq. (3.24), assuming a constant frequency spectrum over the range of integration, are shown in Fig. 3.3. The perpendicular distance to the geometrical ray is plotted on the horizontal axis and the sensitivity to slowness perturbations is plotted on the vertical axis. The figure shows that the maximum sensitivity to the slowness perturbation field is off the path of the geometrical ray. This phenomenon is observed by several other authors (viz. Marquering *et al.*, 1998; Marquering *et al.*, 1999; Snieder and Lomax, 1996; Yomogida, 1992). Thus, scattering theory deviates from ray theory, which predicts that the travel time is sensitive to only the slowness field on the ray. We see furthermore that the sensitivity kernel has sidelobes with a decreasing amplitude away from the ray path. This means that finite-frequency time perturbations are sensitive to slowness perturbations surrounding the ray
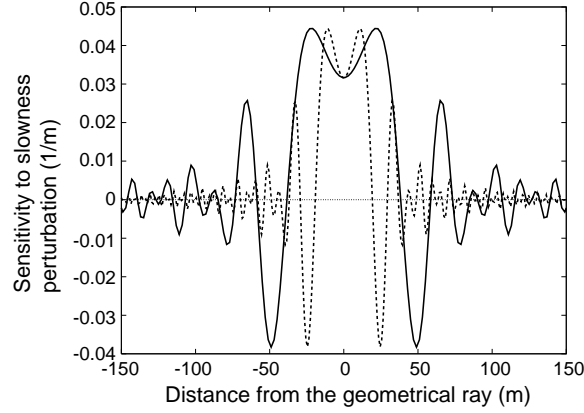
Figure 3.3: *The sensitivity kernel for an incident plane wave (solid line) and for a point source (dashed line). The reference slowness is 2.5×10^{-4} s/m, the constant frequency-band is between 150 Hz and 250 Hz, and the offset is 100 m. The sensitivity kernel for a plane wave is computed at the initial wavefront, whereas the sensitivity kernel for a point source is evaluated at the half distance between the source and receiver. The maximum width of the positive, central lobe of the sensitivity kernel for a plane wave is twice the maximum width of the positive, central lobe of the sensitivity kernel for a point source.*

path. In 3-D, the sensitivity kernel is even zero on the ray, which is well-illustrated in Marquering *et al.* (1999).

The width of the positive, central lobe of the sensitivity kernel for plane waves is computed by setting the sine-function in Eq. (3.23) equal to zero. Hence

$$\sin\left(\pi u_0 v \frac{(z-z_j)^2}{(L-x)} + \frac{\pi}{4}\right) = 0. \tag{3.25}$$

We isolate $z - z_j$ and multiply by two in order to calculate the width $W_{sens}^{plw}(x)$ of the positive, central lobe:

$$W_{sens}^{plw}(x) = \sqrt{3\lambda(L-x)}, \tag{3.26}$$

In the same manner, we derive from Eq. (3.24) the width $W_{sens}^{ps}(x)$ of the positive central lobe of the sensitivity kernel for point sources.

$$W_{sens}^{ps}(x) = \sqrt{\frac{3\lambda x(L-x)}{L}}. \tag{3.27}$$

Next we compare the widths $W_{sens}^{plw}(x)$ and $W_{sens}^{ps}(x)$ with the width of Fresnel zones in Eq. (3.3) and (3.5), respectively. Except for different factors 3 and $8/n$, the two kinds of expressions have the same dependence on λ, x and L. Equating these factors enables us

to get an estimate of the number n in Eq. (3.3) and (3.5) for the width of Fresnel zones. We find that

$$n = \frac{8}{3},\tag{3.28}$$

in two dimensions. In 3-D, $n = 2$, which can by derived by comparing the width of the positive, central lobe of 3-D sensitivity kernels with the width of Fresnel zones. The value of n is important because Fresnel zones are physically interpreted as positive interference of waves with a detour less that λ/n. In 2-D, this difference in propagation length must not exceed $3\lambda/8$ for the first Fresnel zone. We interpret the width of the positive, central lobe of sensitivity kernels as the width of Fresnel zones.

Finally, we show with the stationary-phase approximation (Bleistein, 1984) that the integration of the product of the slowness perturbation field and the sensitivity kernel for plane waves over space is equivalent to Eq. (3.12) which is valid for first-order ray perturbation theory. Although we use the sensitivity kernel for plane waves in Eq. (3.23) in the derivation, the result is also valid for the sensitivity kernel for point sources in 2-D as well as for a point source or a plane incoming wave in 3-D. We assume that the slowness perturbation field depends only on the propagation distance from the source. Thus, by making use of the 2-D sensitivity kernel for plane waves, it follows that, for $z_j = 0$,

$$
\begin{aligned}
\int_0^L \int_{-\infty}^{\infty} u_1(x) K^{plw}(x,z) dz dx &= \sqrt{u_0} \int_{v_0-\Delta v}^{v_0+\Delta v} A(v)\sqrt{v} \int_0^L \frac{u_1(x)}{\sqrt{L-x}} \\
&\quad \times \int_{-\infty}^{\infty} \sin\left(v\pi u_0 \frac{z^2}{(L-x)} + \frac{\pi}{4}\right) dz dx dv \\
&= \frac{\sqrt{u_0}}{2i} \int_{v_0-\Delta v}^{v_0+\Delta v} A(v)\sqrt{v} \int_0^L \frac{u_1(x)}{\sqrt{L-x}} \\
&\quad \times \int_{-\infty}^{\infty} \left(e^{i(v\pi u_0 \frac{z^2}{(L-x)} + \frac{\pi}{4})} - e^{-i(v\pi u_0 \frac{z^2}{(L-x)} + \frac{\pi}{4})} \right) dz dx dv \\
&\approx \frac{\sqrt{u_0}}{2i} \int_{v_0-\Delta v}^{v_0+\Delta v} A(v)\sqrt{v} \int_0^L \frac{u_1(x)}{\sqrt{L-x}} \left(2i\sqrt{\frac{L-x}{v u_0}}\right) dx dv \\
&= \int_{v_0-\Delta v}^{v_0+\Delta v} A(v) dv \int_0^L u_1(x) dx \\
&= \int_0^L u_1(x) dx,\tag{3.29}
\end{aligned}
$$

which is directly comparable to the result for ray theory in Eq. (3.12).

3.3   Setup of the numerical experiment

In order to scrutinise the discrepancy between ray theory and scattering theory, we have constructed a 2-D, numerical experiment with a slab of slowness perturbations that varies

increasingly rapidly as a function of depth. The wavefield is initialised by a plane wave source. The name of this experiment is the 'sweep-experiment' because the function of the slowness perturbation field resembles the sweep source function used in exploration seismology. The heterogeneous slab has the width W with its left hand-side at offset x_l from the source as shown in Fig. 3.1. The slowness field is defined as

$$u(z) = \begin{cases} u_0 & \text{outside the slab,} \\ u_0 + \sqrt{2}\varepsilon u_0 \sin\left(\frac{(z+z_0)^4}{k}\right) & \text{inside the slab,} \end{cases} \tag{3.30}$$

where u_0 is the reference slowness and ε is the rms value of slowness perturbation fluctuations. The two parameters $z_0 = 300$ m and $k = 1.5 \times 10^{10}$ m^4 are used to adjust the sweep-function to the situation in which scattering theory becomes significant. In every sweep-experiment, $u_0 = 2.5 \times 10^{-4}$ s/m, $x_l = 20$ m and $W = 20$ m. The size of this experiment is 100 m $\times$ 600 m, with the horizontal source position at zero-offset, and the vertical receiver array is at $L = 100$ m offset. In the sweep-experiment in Fig. 3.4A and 3.4B, $\varepsilon = 0.017$ and 0.035, respectively.

In addition to the sweep-experiment, with another numerical experiment we demonstrate the validity of our scattering theory in a realisation of the Gaussian random model. The auto-correlation function for Gaussian media is given in Eq. (3.8). For one case, we applied the plane wave source as in the sweep-experiment, and in the other case we used a point source to verify that the sensitivity kernel due to point sources in Eq. (3.24) is correct. The Gaussian random media experiments in Fig. 3.5A and 3.5B measure 200 m $\times$ 230 m and 100 m $\times$ 130 m for the plane wave source and the point source, respectively. For the incident plane wave, the initial wavefront is at $x = 0$, and the offset of the vertical array receivers is $L = 200$ m. For the point source, the source at zero-offset is located at 65 m depth, and the vertical receiver array is at $L = 100$ m offset.

Because the mean value of slowness perturbations in finite-sized realisations of Gaussian random media is not necessary zero, the value of the constant reference slowness u_0 differs in the two Gaussian random media experiments. It can be proven that

$$\text{If} \quad \int N(\mathbf{r})d\mathbf{V} \neq 0 \quad \text{then} \quad <u_1> \neq 0, \tag{3.31}$$

where $N(\mathbf{r})$ is the autocorrelation of the random medium (Müller *et al.*, 1992). We have chosen the reference slowness field to be equal to the mean value of the slowness field in the two Gaussian, random media, e.g. $u_0 = <u>$. Due to the more severe grid condition for using a point source than an incoming plane wave in the numerical experiment, we used different realisations of a Gaussian, random medium in the two Gaussian experiments. As a result, the reference slowness is given by $u_0 = 2.470 \times 10^{-4}$ s/m for the test with an incoming plane wave, and 2.456×10^{-4} s/m for that with a point source. However, $\varepsilon = 0.025$ in both experiments.

To ascertain whether ray theory or scattering theory is dominant, we compare the theoretical residual times for ray theory and scattering theory with the 'observed' data determined in the following way. First, synthetic data for a reference model and a perturbed model are computed with a finite-differences solution of the wave equation (FD-code).

A) Plane wave

B) Plane wave
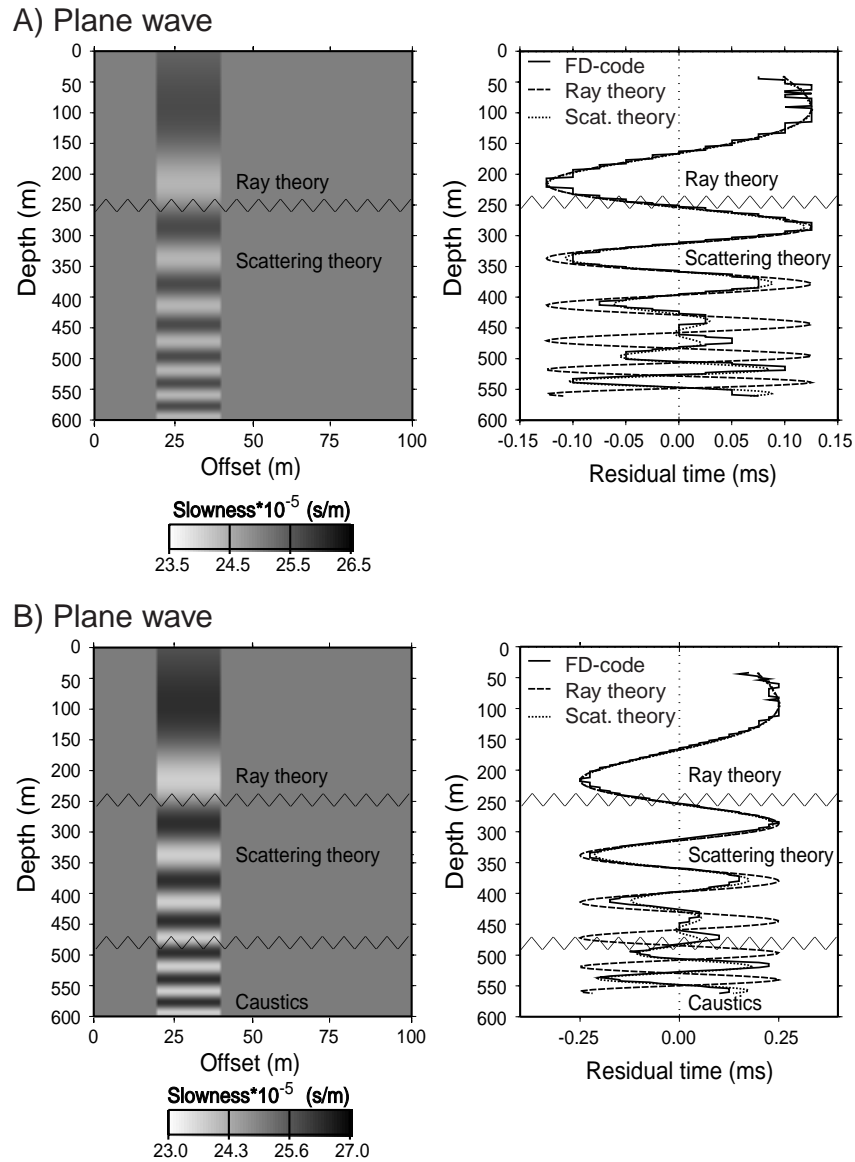
Figure 3.4: *Performance of ray theory versus scattering theory in the numerical experiments. The slowness field is shown with grey-scale colours. Time residuals for first-order ray perturbation theory (dashed line) and for scattering theory (dotted line) are compared with the 'observed' timeshifts (solid line). A) The sweep-experiment using a plane wave with $\varepsilon = 0.017$. B) The sweep-experiment using a plane wave with $\varepsilon = 0.035$.*

A) Plane wave

B) Point source
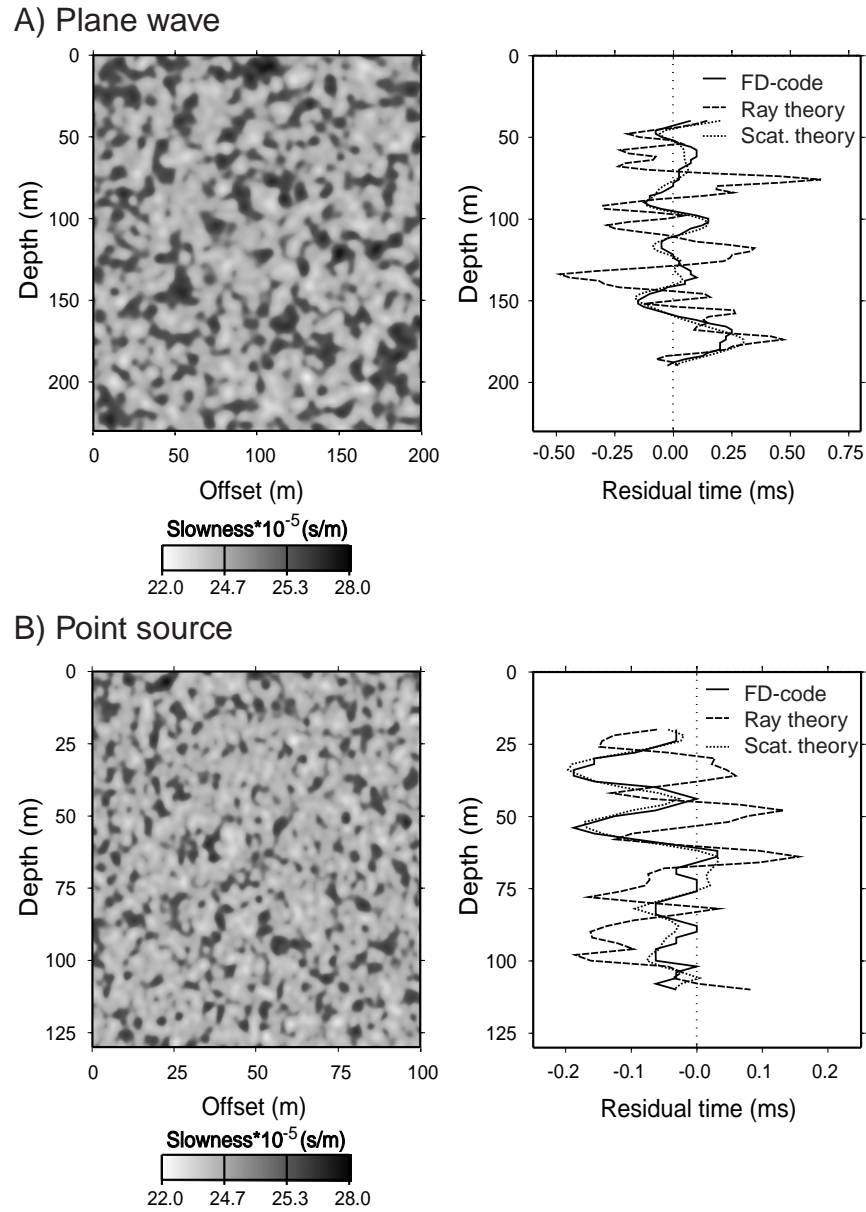
Figure 3.5: *As in Fig. 3.4. A) The Gaussian random media experiment with $\varepsilon = 0.025$ and $a = 7$ m. The wavefield is initialised by a plane wave source. B) The Gaussian random media experiment with $\varepsilon = 0.025$ and $a = 3$ m, but with a different slownesss medium than that in Fig. 3.5A. The wavefield is initiated by a point source.*

For the reference model, the slowness field is set to the constant u_0, and, for the perturbed model, the sweep-model or the Gaussian random medium is applied. The 'observed' residual times are then obtained by comparing the waveforms in the filtered reference wavefields with the waveforms in the filtered perturbed wavefields. By filtering is meant that the FD-data are band-pass filtered in the same frequency-range over which the sensitivity kernels are averaged. The first extremum of the waveform is used as a markpoint to get the absolute travel time for each set of filtered waveforms. The 'observed' delay time is then defined as the difference between the absolute travel time for the filtered reference wavefields and for the filtered perturbed wavefields.

3.4   Results

In Fig. 3.4A and 3.4B we show the traveltime changes for the sweep-experiment due to an incident plane wave. The frequency-band of the recorded wavefield is in the range [150;250] (Hz). The 2-D slowness field is shown with grey-scale colours in both figures. The time delays due to first-order ray perturbation theory are plotted with the dashed line, residual times computed with the Rytov approximation are shown with the dotted line, and the 'observed' timeshifts are shown with the solid line. In both examples of the sweep experiment we used the sensitivity kernel in Eq. (3.23). It is observed in Fig. 3.4A and 3.4B that the FD-time delays have some small, but abrupt, oscillations that are due to errors in the picking of the 'observed' data.

In Fig. 3.4A and 3.4B, we mark with a jagged, black line the transition zone where ray theory breaks down in favour of scattering theory based on the condition for ray theory in Eq. (3.13) that the width of Fresnel zones in Eq. (3.26) is less than the local length-scale a of slowness perturbations in the sweep-experiment. For a central wavelength $\lambda = 20$ m, and $x = 70$ m (the central distance of the heterogeneous slab from the receiver), we have that $W_{sens}^{plw} = 65$ m. For comparison, in the center of the transition zone ($z = 250$ m) the half wavelength of the sweep-function in Eq. (3.30) is about 61 m. We conclude from these two experiments that, in general the non-dimensional number L_F^{plw}/a for the regime of scattering theory is

$$\frac{L_F^{plw}}{a} > 1, \tag{3.32}$$

where L_F^{plw} is the maximum width of Fresnel zones for plane waves.

In Fig. 3.4A and 3.4B, below the transition zone from ray theory to scattering theory the timeshifts computed with first-order ray perturbation theory cannot fit the 'observed' residual times; moreover, these ray-theoretical time delays are even out off phase with both the 'observed' timeshifts and the finite-frequency time delays for depths between 450 m and 560 m. The time delays due to single-scattering theory predict the FD-timeshifts rather well. The scattering theory predicts not only the order of magnitude of the 'observed' time delays, but it also gives the correct result for depths below 450 m in the sweep-experiment, where the FD-timeshifts are anti-correlated with the ray-theoretical residual times.

Offset (m)
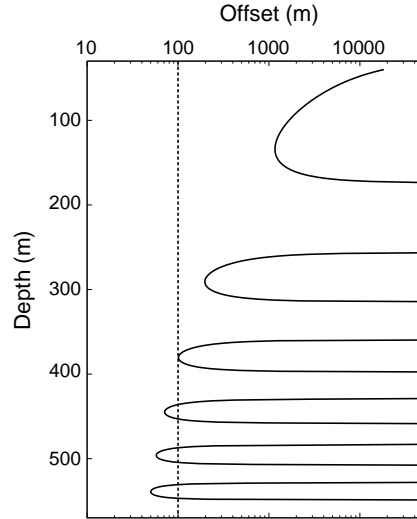
Figure 3.6: *The focal length of a plane wavefield is calculated for the case of the sweep-experiment with ε = 0.071. If the focal length (solid line) of the converging wavefield is to the left of the receiver position (dashed line) then caustics will occur in the recorded data.*

In Fig. 3.6, we show a plot that shows the focus position x_{caus} of a plane wavefield passing through the sweep-model with ε = 0.071, which is on purpose a larger value than that applied in the sweep-experiments in Fig. 3.4A and 3.4B. Given a depth z, the focal length (solid line) in Fig. 3.6 is computed with Eq. (3.6) and (3.7), while the dashed line marks the source-receiver distance. Where the focal length of the converging wavefield is smaller than the distance between the source and receiver, caustics develop before measuring the wavefield at the receivers. Additionally, in Fig. 3.7 we show six snapshots (taken at the absolute travel time t = 0 ms, 5 ms, 10 ms, 15 ms, 20 ms and 25 ms) of the wavefield that propagates through the sweep-model for ε = 0.071. The thin slab of inhomogeneity is marked in the figure with a black box and black stripes. For the earliest two snapshots, the wave propagates in a constant slowness field. For t = 10 ms, the wave has just passed through the slowness perturbation field, so the wavefront has been deflected by slowness heterogeneities. The first two triplications occur between 40 m and 60 m offset. Note the high energy density at the kinks in the wavefront; these kinks are associated with the caustics. In the latest two snapshots, for t = 20 ms and 25 ms, the caustics are much more clear as they give rise to half-bow-tie shaped wavefronts (triplications) behind the ballistic wavefield. The distances at which the caustics in Fig. 3.7 start to generate correspond well with the focal lengths that are predicted in Fig. 3.6.

For the sweep-experiment with ε = 0.017, no caustics are produced in the wavefield, while for ε = 0.035, triplications occur before recording the wavefield at receivers at

depths below 480 m. The zone with caustics is indicated in Fig. 3.4B. At this point, we must reconsider the validity of the Rytov approximation for transmitted waves where triplications are present in the recorded wavefield, such as in results of the sweep-experiment as shown in Fig. 3.4B. In comparing the Rytov approximation with the Born approximation, Beydoun and Tarantola (1988), Brown (1967), DeWolf (1967), Fried (1967), Hufnagel and Stanley (1964), Keller (1969), Sancer and Varvatsis (1970) and Taylor (1967) conclude that the Rytov approximation has validity for a larger range of the slowness perturbation parameter than does the Born approximation. They, however, do not investigate the validity of the Born and Rytov approximations when non-linear effects such as the development of triplications become operative. In this study, we have tested the validity of the Rytov approximation in the regime of caustics. We computed the perturbed wavefields for the sweep-experiment with $\varepsilon = 0.017, 0.035, 0.071, 0.11$ and 0.14, and estimated the FD-time delays by using the first extremum of the filtered waveforms. For the sweep-experiment with $\varepsilon = 0.017$, the theory for caustics in 1-D slowness perturbation fields predicts that triplications would not be recorded in the data, but for larger ε triplications would always occur in the measured wavefield. We have shown the sweep-experiment with the two lowest values of ε in Fig. 3.4A and 3.4B, but the sweep-experiment with larger ε are not shown here. In brief, we find that the Rytov approximation does a good job even in areas with a strong development of triplications. We therefore propose that the validity of the Rytov approximation of ballistic waves extends into the regime where caustics are present in data.

In order to demonstrate the validity of the single-scattering theory in more complex media, we use the Gaussian random media experiment, where scattering is significant. The rms value of relative slowness fluctuations ε is given by 0.025, and the length-scale of slowness anomalies $a = 7$ m for the incoming plane wave experiment and $a = 3$ m for the point source experiment. We use the same linetype convention as in the sweep-experiment for the residual times computed with ray theory, scattering theory and the FD-code. Results for this experiment, for an incident plane wave and a point source, respectively, are shown in Fig. 3.5A and 3.5B, where we make use of the sensitivity kernel formulation in Eq. (3.23) and (3.24) to compute the scattering theoretical timeshifts.

For an incident plane wave, the frequency is from 150 Hz to 250 Hz, so according to Eq. (3.32), ray theory breaks down when the characteristic length of slowness anomalies is smaller than $L_F^{plw} = 110$ m. In this case, the length-scale of slowness perturbations $a = 7$ m, so the 'observed' time delays should be strongly dominated by scattering. This is indeed what is observed in Fig. 3.5A. The finite-frequency residual times fit the 'observed' time delays correctly while ray theory does not account for the travel time deviations.

Fig. 3.5B shows results of the Gaussian random media experiment for a point source with frequencies ranging from 200 Hz to 400 Hz. Using the sensitivity kernel in Eq. (3.24) to compute the residual times due to scattering theory we compute the maximum width of Fresnel zones as $L_F^{ps} = 31.9$ m for $\lambda = 13.6$ m and $L = 100$ m. The length-scale of slowness anomalies $a = 3$ m, is thus about 10 % of L_F^{ps}. In Fig. 3.5B, scattering theory predicts the 'observed' residual times well but the ray-theoretical timeshifts do not fit the FD-time delays. As in the experiments in Fig. 3.4A, 3.4B and 3.5A where a plane wave
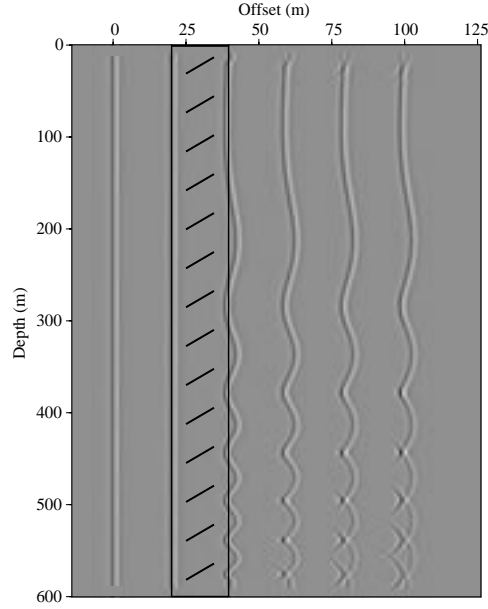
Figure 3.7: *Snapshots of plane wave propagation in the sweep-experiment with* $\varepsilon = 0.071$. *The slab of slowness heterogeneities is shown with the black box and black stripes. The absolute travel times t = 0, 5, 15, 20, 25 ms are marked at the respective wave fronts. The triplications become clear in the wavefronts for t = 15, 20, 25 ms.*

is applied, we conclude that the regime of scattering theory for wavefields emitted by a point source is significant when

$$\frac{L_F^{ps}}{a} > 1. \tag{3.33}$$

We have computed if the recorded wavefields for plane waves and point sources, respectively, in the Gaussian random media experiments contain triplications. By inserting $\varepsilon = 0.025$ in the condition for caustic formation in Eq. (3.9) and (3.10), we find that

$$\frac{L}{a} \geq \begin{cases} 6.1 & \text{for plane waves,} \\ 13.1 & \text{for point sources.} \end{cases} \tag{3.34}$$

With the auto-correlation length $a = 7$ m for the plane wave and $a = 3$ for the point source, this implies that caustics are present in the recorded wavefields in the Gaussian experiments in Fig. 3.5A (a plane wave with $L = 200$ m) and 3.5B (a point source with $L = 100$ m).

The non-dimensional numbers for the regime of ray theory, scattering theory and triplications are summarised in Table 3.1. Notice that four parameters determine when these three distinct regimes are significant. These four parameters are the wavelength λ,

Regime of;	λ/a	L_F/a	L/a	
Ray theory	$\ll 1$	$\ll 1$	$\times$	
Scattering theory	$\times$	> 1	$\times$	
Triplications	$\times$	$\times$	$> \begin{cases} 0.52\varepsilon^{-2/3} & \text{(plw)}, \\ 1.12\varepsilon^{-2/3} & \text{(ps)}. \end{cases}$	

Table 3.1: *The non-dimensional numbers λ/a, L_F/a and L/a which describe the regime of ray theory, scattering theory and triplications. The cross ($\times$) indicates that this parameter is not of relevance for the physical effect that is considered.*

the source-receiver distance L, the rms value of relative slowness fluctuations ε and the length-scale a of inhomogeneity.

3.5 Application of the regime of scattering theory

We consider implications for three examples taken from seismology, ocean acoustic and medical imaging for which scattering theory is important. The source in all three cases is a point source, so the condition for scattering theory due to point sources, Eq. (3.33), is that $L_F^{ps}/a > 1$. The example from seismology is global surface wave tomography where the surface waves propagate in two dimensions on a sphere, while in the case of ocean acoustic or medical imaging the wave propagation is in the three-dimensional Cartesian space. Thus the dimension of the wave propagation in each particular experiment must be considered.

The maximum width of Fresnel zones for point sources is at the half source-receiver distance. We find that

$$L_F^{ps} = \sqrt{\frac{3\lambda}{2}\tan\left(\frac{\Delta}{2}\right)} \quad \text{(a sphere)} \quad \text{and} \quad L_F^{ps} = \sqrt{\lambda L} \quad \text{(3-D Cartesian space).} \quad (3.35)$$

(See appendix A for a derivation of the width of Fresnel zones for surface waves.) For the width of the Fresnel zone on the sphere, we have used according to Eq. (3.28) that $n = 8/3$. On the sphere both the wavelength and the epicentral distance are measured in radians. The parameter Δ denotes the epicentral distance between the source and receiver. For L_F^{ps} in a 3-D Cartesian space, we applied Eq. (3.5) for $n = 2$.

In global surface wave tomography (Trampert and Woodhouse, 1995; Trampert and Woodhouse, 1996), a characteristic propagation distance is about 145 degrees, and the wavelength is about 700 km for Love waves at 150 s. For a high-resolution, global surface wave experiment, slowness anomalies have a length-scale as small as 1000 km. We find that $L_F^{ps} = 4600$ km, so scattering theory is important. Scattering theory will be even more significant for larger wavelengths and source-receiver distances.

In ocean acoustic, Hodgkiss *et al*. (1999) and Kuperman *et al*. (1998) carry out a time-reversed mirror experiment wherein the source-receiver distance is 6.3 km, and the characteristic wavelength $\lambda = 3.4$ m (the sound speed in sea water with 3.5 % salinity at

20 degrees celcius is 1522 m/s, and the characteristic frequency of acoustic waves in the experiment is 445 Hz). The width of Fresnel zones is then 146 m, which is larger than the surface-bottom depth in their experiment. This means that any heterogeneity within the region of the experiment is smaller than the width of Fresnel zones, so scattering theory is significant.

In medical imaging (Baba *et al*., 1989; King and Shao, 1990), ultrasound is applied to scan the chest, the heart, the foetus, the veins, etc... The velocity of the employed waves varies between 1440 m/s (fat) and 1675 m/s (collagen), while the frequency is in the MHz-range so let the frequency $\nu = 30$ MHz. The wavelength then varies between 48 μm and 56 μm and an average distance L between the transducer and receiver instrument is about 20 cm. The width of Fresnel zones $L_F^{ps} \approx 3$ mm, which is greater than the diameter of blood vessels and cell structures in the body. Thus scattering theory is important.

3.6   Conclusions

We have shown that first-order ray theory fails in favour of linearised scattering theory in predicting the travel timeshifts of waves in heterogeneous media when the length-scale of slowness heterogeneity is smaller than the width of Fresnel zones. The condition for the regime of scattering theory depends on the frequency content of the recorded wavefield and the propagation length of the ballistic wave between the source and receiver.

The scattering theory presented in this paper is based on the first-order Rytov approximation, so the scattering theoretical time delays are well-defined for finite-frequencies. Physically, this means that finite-frequency timeshifts have the maximum sensitivity to slowness fluctuations off the path of the ray and, moreover, is sensitive to the slowness fluctuation field in the whole space of wave propagation. In contrast, ray theoretical residual times are dependent on only the slowness fluctuation field which is on the geometrical ray.

Scattering theory can predict the travel residual times of waves in inhomogeneous media even if triplications are present in the recorded wavefield. We have presented a condition for the regime of caustics in heterogeneous media, both with a 1-D slowness field and with a Gaussian random medium for initially plane waves and point sources. This condition is independent of the frequency of the recorded wavefield. Not surprisingly, we have found that the greater the magnitude of the slowness fluctuations, the more easily triplications develop in the wavefields. However, the $\varepsilon^{-2/3}$-dependence for slowness fields described by Gaussian random media is nontrivial. Notice that in the numerical experiments the Rytov approximation provides an accurate estimate of the timeshift, regardless of the fact whether caustics have developed or not.

The numerical experiments carried out in this paper are kept as general as possible. The results for the regime of scattering theory and of triplications are therefore applicable to domains such as seismology, ocean acoustic, non-destructive testing and medical imaging where wave phenomena are important.

References

Baba K., Satch S., Sakamoto S., Okai T. and Shiego I. (**1989**). Development of an ultrasonic system for three-dimensional reconstruction of the foetus, J. Perinat Med. **17**, 19-24.

Beydoun W. B. and Tarantola A. (**1988**). First Born and Rytov approximations: modeling and inversion conditions in a canonical example, J. Acoust. Soc. Am. **83** (3), 1045-1055.

Bleistein N. (**1984**). *Mathematical methods for wave phenomena* (Academic Press, Orlanda, FL.).

Brown W. P. (**1967**). Validity of the Rytov approximation, J. Opt. Soc. Am. **57**, 1539-1543.

DeWolf D. A. (**1967**). Validity of Rytov's approximation, J. Opt. Soc. Am. **57**, 1057-1059.

Fehler M., Sato H. and Huang L. (**2000**). Envelope broadening of outgoing waves in 2D random media: a comparison between the markov approximation and numerical simulations, Bull. Seism. Soc. Am. **90**, 914-928.

Fried D. L. (**1967**). Test of the Rytov approximation, J. Opt. Soc. Am. **57**, 268-269.

Haque S., Lu G. Q., Goings J. and Sigmund J. (**1999**). Characterization of interfacial thermal resistance by acoustic micrography imaging, *Proceedings of the 1999 annual power electronics seminar at Virginia Tech, September 19-21*, 375-382.

Hodgkiss W. S., Song H. C., Kuperman W. A., Akal T., Farla C. and Jackson D. (**1999**). A long-range and variable focus phase-conjugation experiment in shallow water, J. Acoust. Soc. Am. **105**, 1597-1604.

Hufnagel R. P. and Stanley N. R. (**1964**). Modulation transfer function associated with image transmission through turbulent media, J. Opt. Soc. Am. **54**, 52-61.

Jensen J. M. and Jacobsen B. H. (**1997**). Rapid exact linearized inversion of time-distance helioseismic data in the periodic approximation, in *Proceedings of the Interdisciplinary inversion workshop 5, Methodology and applications in geophysics, astronomy, geodesy and physics*, Edited by Jacobsen B. H. (Århus University), 57-67.

Keller J. B. (**1969**). Accuracy and validity of the Born and Rytov approximation, J. Opt. Soc. Am. **59**, 1003-1004.

King D. L. and Shao M. Y. (**1990**). Three-dimensional spatial registration and interactive display of position and orientation of real-time ultrasound images, JUM. **9**, 525-532.

Kravtsov Y. A. (**1988**). 'Rays and caustics as physical objects' in *Prog. in Optics*, XXVI, Edited by Wolf E. (Elsevier, Amsterdam), 227-348.

Kuperman W. A., Hodgkiss W. S., Song H. C., Akal T., Farla C. and Jackson D. (**1998**). Phase conjugation in the ocean: experimental demonstration of an acoustic time-reversal mirror, J. Acoust. Soc. Am. **103**, 25-40.

Marquering H., Nolet G. and Dahlen F. A. (**1998**). Three-dimensional waveform sensitivity kernels, Geophys. J. Int. **132**, 521-534.

Marquering H., Dahlen F. A. and Nolet G. (**1999**). The body-wave travel-time paradox: bananas, doughnuts and 3-D delay-time kernels, Geophys. J. Int. **137**, 805-815.

Menke W. and Abbot D. (**1990**). *Geophysical theory* (Columbia University Press, NY.).

Müller G., Roth M. and Korn M. (**1992**). Seismic-wave traveltimes in random media, Geophys. J. Int. **110**, 29-41.

Passier M. L and Snieder R. (**1995**). Using differential waveform data to retrieve local S-velocity structure or path-averaged S-velocity gradients, J. Geophys. Res. **100**, 24061-24078.

Pulliam J. and Snieder R. (**1998**). Ray perturbation theory, dynamic ray tracing, and the determination of Fresnel zones, Geophys. J. Int. **135**, 463-469.

Sancer M. I. and Varvatsis A. D. (**1970**). 'A comparison of the Born and Rytov methods' in *Proceedings of the IEE*, 140-141.

Snieder R. and Sambridge M. (**1992**). Ray perturbation theory for travel times and ray-paths in 3-D heterogeneous media, Geophys. J. Int. **109**, 294-322.

Snieder R. and Lomax A. (**1996**). Wavefield smoothing and the effect of rough velocity perturbations on arrival times and amplitudes, Geophys. J. Int. **125**, 796-812.

Spetzler J. and Snieder R. (**2001**). The formation of caustics in two and three dimensional media, Geophys. J. Int. **144**, 175-182.

Taylor L. S. (**1967**). On Rytov's methods, Radio Science. **2**, 437-441.

Trampert J. and Woodhouse J. H. (**1995**). Global phase velocity maps of Love and Rayleigh waves between 40 and 150 seconds, Geophys. J. Int. **122**, 675-690.

Trampert J. and Woodhouse J. H. (**1996**). High resolution global phase velocity distributions, Geophys. Res. Lett. **23**, 21-24.

Yomogida K. (**1992**). Fresnel zone inversion for lateral heterogeneities in the Earth, PAGEOPH, **138** (3), 391-406.

Woodward M. J. (**1992**). Wave-equation tomography, Geophysics **57**, 15-26.

3.7   Appendix A: The width of Fresnel zones on a sphere

According to Fig. 3.8, the epicentral distance between the source and receiver is denoted by Δ, and the epicentral distance between the source and scatterer point and the scatterer point and receiver are marked as η and η', respectively. The half-width of Fresnel zones at the offset γ is denoted q. Using the law of cosines on a sphere to relate η with q and γ, we get that

$$
\begin{aligned}
\cos(\eta) &= \cos(q)\cos(\gamma) + \sin(q)\sin(\gamma)\cos\left(\frac{\pi}{2}\right) \\
&= \cos(q)\cos(\gamma).
\end{aligned}
\tag{3.36}
$$

Isolating η from Eq. (3.36) and assuming that the ray deflection q is small gives

$$
\begin{aligned}
\eta &= \arccos\left(\cos(q)\cos(\gamma)\right) \\
&\approx \arccos\left(\cos(\gamma) - \frac{1}{2}q^2\cos(\gamma)\right) \\
&\approx \gamma + \frac{q^2}{2\tan(\gamma)}.
\end{aligned}
\tag{3.37}
$$

Similarly, we have for η' that

$$
\eta' = (\Delta - \gamma) + \frac{q^2}{2\tan(\Delta - \gamma)}.
\tag{3.38}
$$

The detour $\eta + \eta' - \Delta$ is calculated as

$$
\begin{aligned}
\eta + \eta' - \Delta &= \frac{q^2}{2}\left(\frac{1}{\tan(\gamma)} + \frac{1}{\tan(\Delta - \gamma)}\right) \\
&= \frac{q^2}{2}\frac{\sin(\Delta)}{\sin(\gamma)\sin(\Delta - \gamma)}.
\end{aligned}
\tag{3.39}
$$

The condition for Fresnel zones on the sphere that the detour is less than the wavelength divided by a number n is given by

$$
\eta + \eta' - \Delta \leq \frac{\lambda}{n},
\tag{3.40}
$$

where λ is the wavelength measured in radians. The detour in Eq. (3.39) is inserted in the Fresnel zone condition in Eq. (3.40), where the sign of equality is applied for the Fresnel
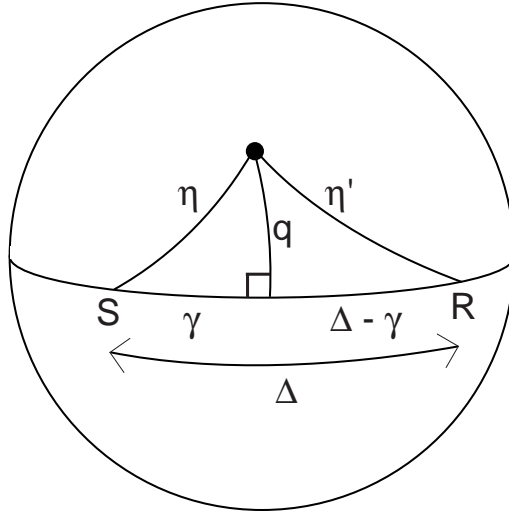
Figure 3.8: *Explanation of the variables used to construct the Fresnel zone due to a point source on the sphere.*

zone boundary. Thereby the half width q of Fresnel zones is given by

$$q = \sqrt{\frac{2\lambda \sin(\gamma)\sin(\Delta - \gamma)}{n\sin(\Delta)}}, \tag{3.41}$$

which has the largest value for $\gamma = \Delta/2$. For that case,

$$q = \sqrt{\frac{\lambda}{n}\tan\left(\frac{\Delta}{2}\right)}. \tag{3.42}$$

The maximum width L_F^{ps} of Fresnel zones due to point sources is the half-width q in Eq. (3.42) multiplied by 2; thus

$$L_F^{ps} = \sqrt{\frac{4\lambda}{n}\tan\left(\frac{\Delta}{2}\right)}, \tag{3.43}$$

where L_F^{ps} and λ are measured in radians.

Chapter 4

A test of ray theory and scattering theory based on a laboratory experiment using ultrasonic waves and numerical simulations by finite-difference method

Abstract.

   The structure of the Earth is represented by a wide spectrum of small-scale structures, as well as large-scale structures. However, tomographic imaging techniques based on ray theory are often applied inappropriately in models with the characteristic length of heterogeneity smaller than the wavelength and the width of the Fresnel zone. In other words, the conditions for ray theory are not satisfied in such models. It is therefore necessary to apply diffraction theory of waves in tomographic reconstruction techniques in order to retrieve images of the Earth with the correct theory. Physically speaking, scattering theory takes the finite-frequency effect of waves into account.

   We performed a test of ray theory and scattering theory in an ultrasonic wave experiment and in a numerical finite-difference experiment using random media with correlation lengths smaller than the width of the Fresnel zone. We used a stochastic approach to compute the mean squared value of timeshift variations calculated from ray theory and diffraction theory. The theoretical results were compared with the experimental values obtained in the laboratory experiment using rock samples with different length-scales

of heterogeneity and from numerical experiments on wave propagation in quasi-random media. We observed that ray theory overestimates the mean squared value of timeshift variations, while the observed statistical values from the two kinds of laboratory experiments are well predicted by scattering theory. This means that tomographic imaging techniques based on ray theory suffer from a loss of resolution when the reconstructing models have a characteristic length of heterogeneity smaller than the width of the Fresnel zone.

4.1   Introduction

In this study, we examine ray theory and scattering theory in a laboratory experiment using ultrasonic waves propagating in granite samples with small-scale heterogeneity. Ray theory is a high-frequency theory which is valid if the characteristic length of inhomogeneity is larger than the wavelength and the width of the Fresnel zone. Accordingly, it is only justified to use ray theory in modeling of sufficiently smooth media. On the other hand, people working with seismology (van der Lee and Nolet, 1997; Trampert and Woodhouse, 1995; Bijwaard and Spakman, 1998; Curtis *et al.*, 1998) or with exploration seismics (Parra and Bangs, 1992; Goudswaard *et al.*, 1998; Hatchell, 2000) focus more and more on small-scale structured media for which the conditions for ray theory are generally not satisfied. For such media with heterogeneity comparable or smaller in size than the width of the Fresnel zone, scattering theory of propagating waves is important (Spetzler and Snieder, 2001a).

There has been much attention on scattering theory during the last decade in the literature. Yomogida and Aki (1987), Yomogida (1992), Woodward (1992), Snieder and Lomax (1996) and Spetzler and Snieder (2001a) use the Rytov approximation on the 2-D acoustic wave equation to introduce finite-frequency effects in transmitted waves. Marquering *et al.* (1998), Tong *et al.* (1998), Marquering *et al.* (1999), Dahlen *et al.* (2000) and Hung *et al.* (2000) utilise the cross-correlation function to introduce the frequency-depending timeshift in three dimensional body wave tomography. In many of these articles, it is shown that scattering theory in 2-D and 3-D media predicts that the maximum sensitivity to slowness perturbations is off-path the geometrical ray. Moreover a paradoxical result is found for the scattering of waves in three dimensions; the sensitivity to slowness fluctuations is zero on the ray path. It is a counter-intuitive result compared to ray theory which predicts non-zero sensitivity to the slowness field on the ray path.

Several authors have worked with laboratory experiments using ultrasonic waves. Lo *et al.* (1988) tested the Rytov approximation and the Born approximation in VSP, cross-borehole and surface reflection tomography by using ultrasonic waves propagating in a water tank with gelatin cylinders as scatterers. They found that diffraction tomography is better than ray tomography to reconstruct the model when the size of scatterers is comparable to the wavelength. Schultz and Toksöz (1995) studied scattering from randomly grooved interfaces. Scattering phenomena have been studied in order to understand the attenuation of seismic waves and the generation of coda waves (Dubendorff and Menke, 1986; Vinogradov *et al.*, 1989; Matsunami, 1991; Vinogradov *et al.*, 1992; Schultz and

Toksöz, 1993; Schultz and Toksöz, 1994).

In this study, we combine the developments in scattering theory with high-quality ul-trasonic waveforms measured in a laboratory experiment using samples of Westerly and Oshima granite. The two granites have the property that the slowness perturbation field can be described using an exponential auto-correlation function. We benefit from this property by using a statistical approach to test ray theory and scattering theory in the real laboratory experiment. That is to say that we compute the ray theoretical and scattering theoretical mean squared value of timeshift fluctuations for exponential random media which are comparable with those obtained from the observed ultrasonic waveforms. In that way, we show that scattering theory is more accurate than ray theory in predicting the observed mean squared value of timeshifts for Westerly and Oshima granite. In addition, we simulate the real laboratory experiment with a 2-D, numerical finite-difference exper-iment which supports the results found in the ultrasonic wave experiment rather well.

In section 4.2, we show how ray theory and scattering theory can be adapted to de-terministic and stochastic models. The laboratory experiment is explained in section 4.3, while we describe in section 4.4 how the independent determination of the exponential auto-correlation function for Westerly and Oshima granite was carried out. The 2-D nu-merical experiment is described in section 4.5. In section 4.6, we present the results from the ultrasonic wave experiment and the numerical experiment, and finally in section 4.7 and 4.8 the discussion and conclusions are given.

4.2   Theory

In this section, the mean squared (MS) value of timeshift fluctuations using ray theory and single-scattering theory is derived. We work with two kinds of stochastic media; the exponential random medium which has the auto-correlation function for the slowness perturbation field given by

$$< \delta u(\mathbf{r}')\delta u(\mathbf{r}'') >= (\varepsilon u_0)^2 \exp(-\frac{r}{a}), \tag{4.1}$$

and the Gaussian random medium with the auto-correlation function for slowness pertur-bations given by

$$< \delta u(\mathbf{r}')\delta u(\mathbf{r}'') >= (\varepsilon u_0)^2 \exp(-\left(\frac{r}{a}\right)^2). \tag{4.2}$$

In the two auto-correlation functions in Eq. (4.1) and (4.2), the reference slowness is denoted by u_0, the rms value of relative slowness perturbation field is ε, the correlation length (or roughly the length-scale of heterogeneity) is written as a and $r = |\mathbf{r}'-\mathbf{r}''|$ is the distance between the two points $\mathbf{r}'$ and $\mathbf{r}''$. See Sato and Fehler (1998) for a thorough description of random media.

4.2.1   Ray theory

We follow the idea from Roth (1997) to derive the MS-value of timeshift fluctuations based on first order ray perturbation theory (also related to Fermat's principle). The derivation is valid for timeshifts obtained in experiments with 2-D and 3-D wave propagation. According to first order ray perturbation theory (Snieder and Sambridge, 1992), the timeshift for deterministic slowness perturbation media $\delta u(\mathbf{r})$ is given by

$$\delta t(L) = \int_0^L \delta u(s)ds, \tag{4.3}$$

where L is the source-receiver distance. The squared timeshift $\left(\delta t\right)^2(L)$ is obtained by taking the square of the timeshift in Eq. (4.3), hence

$$\left(\delta t\right)^2(L) = \int_0^L \int_0^L \delta u(s')\delta u(s'')ds'ds''. \tag{4.4}$$

The expectation value is taken of the squared timeshift in Eq. (4.4), so we get the MS-value of timeshift fluctuations $< \left(\delta t\right)^2 > (L)$ due to ray theory.

$$
\begin{aligned}
< \left(\delta t\right)^2 > (L) &= \int_0^L \int_0^L < \delta u(s')\delta u(s'') > ds'ds'' \\
&= 2\int_0^L (L-r)N(r)dr,
\end{aligned}
\tag{4.5}
$$

where the auto-correlation function $N(r) = < \delta u(s')\delta u(s'') >$ and $r = |s' - s''|$. The step to reduce the double integration to a single integration in Eq. (4.5) is explained in Roth (1997).

First the case that the source-receiver distance is much smaller than the correlation length, (i.e. $L/a \ll 1$) is considered. The exponential and Gaussian auto-correlation function in Eq. (4.1) and (4.2) are set to $(\varepsilon u_0)^2$ in this regime. Hence, the MS-value of timeshift fluctuations is given by

$$
\begin{aligned}
< \left(\delta t\right)^2 > (L) &\approx 2(\varepsilon u_0)^2 \int_0^L (L-r)dr \\
&= (\varepsilon u_0 L)^2,
\end{aligned}
\tag{4.6}
$$

which is the same result as for a homogeneous slowness perturbation field.

Second, consider the case that the source-receiver offset is much larger than the correlation length, (i.e. $L/a \gg 1$). For the exponential auto-correlation function in Eq. (4.1), the MS-value of timeshift fluctuations can be calculated in the following way;

$$
\begin{aligned}
< \left(\delta t\right)^2 > (L) &\approx 2(\varepsilon u_0)^2 \int_0^\infty (L-r)\exp(-\frac{r}{a})dr \\
&= 2(\varepsilon u_0)^2 aL.
\end{aligned}
\tag{4.7}
$$

The upper limit in the integration along the source-receiver path is approximated to infinity, because the exponential auto-correlation function goes towards zero as $r \gg a$. For Gaussian random media, the MS-value of timeshift fluctuations is derived in a similar way with the result that

$$< \left(\delta t \right)^2 > (L) \quad = \quad (\varepsilon u_0)^2 \sqrt{\pi} a L. \tag{4.8}$$

Ray theory is valid when the correlation length of heterogeneity is larger than the wavelength λ and the width L_F of the Fresnel zone. In non-dimensional numbers, the conditions for the regime of ray theory are written as

$$\frac{\lambda}{a} \ll 1, \qquad \text{and} \qquad \frac{L_F}{a} \ll 1. \tag{4.9}$$

See Menke and Abbot (1990).

4.2.2   Scattering theory

The scattering theoretical timeshift $\delta t(L)$ is written as a volume integration of the deterministic slowness perturbation field $\delta u(\mathbf{r})$ multiplied by the sensitivity kernel $K(\mathbf{r})$ due to non-ray geometrical effects (Spetzler and Snieder, 2001a). Hence,

$$\delta t(L) = \int_{\mathbf{V}} \delta u(\mathbf{r}) K(\mathbf{r}) dV, \tag{4.10}$$

where the integration $\int_{\mathbf{V}} \cdots dV$ is written as $\int_0^L \int_{-\infty}^{\infty} \cdots dx dz$ for wave propagation in two dimensions and as $\int_0^L \int_{-\infty}^{\infty} \int_{-\infty}^{\infty} \cdots dx dy dz$ for waves propagating in three dimensions. The scattering theoretical timeshift in Eq. (4.10) is squared, so

$$\left(\delta t \right)^2 (L) = \int_{\mathbf{V'}} \int_{\mathbf{V''}} \delta u(\mathbf{r'}) \delta u(\mathbf{r''}) K(\mathbf{r'}) K(\mathbf{r''}) dV' dV'', \tag{4.11}$$

The MS-value of timeshift fluctuations $< \left(\delta t \right)^2 > (L)$ using scattering theory is obtained by taking the expectation value of Eq. (4.11), thus

$$< \left(\delta t \right)^2 > (L) = \int_{\mathbf{V'}} \int_{\mathbf{V''}} < \delta u(\mathbf{r'}) \delta u(\mathbf{r''}) > K(\mathbf{r'}) K(\mathbf{r''}) dV' dV''. \tag{4.12}$$

The 2-D sensitivity kernel for a point source is given by

$$K(x,z) = \sqrt{u_0 L} \int_{\nu_0 - \Delta\nu}^{\nu_0 + \Delta\nu} A(\nu) \sqrt{\nu} \frac{\sin\left(\pi \nu u_0 L \frac{z^2}{x(L-x)} + \frac{\pi}{4} \right)}{\sqrt{x(L-x)}} d\nu, \tag{4.13}$$

(see Spetzler and Snieder, 2001a). The sensitivity kernel in Eq. (4.13) is integrated in the frequency-range $\nu_0 - \Delta\nu$ to $\nu_0 + \Delta\nu$, where the normalised power spectrum $\int_{\nu_0 - \Delta\nu}^{\nu_0 + \Delta\nu} A(\nu) d\nu$

= 1. The central frequency is denoted ν_0 and the width of the frequency-band is $2\Delta\nu$. For a constant power spectrum over the frequency-band (i.e. $A(\nu) = 1/(2\Delta\nu)$), the scattering sensitivity kernel in Eq. (4.13) can be evaluated analytically (see appendix A), hence

$$
\begin{aligned}
K(x,z) &= \frac{\sqrt{u_0 L}}{2\Delta\nu\sqrt{x(L-x)}} \\
&\quad \times \left[\frac{1}{b}\sqrt{\frac{\nu}{2}}\Big(\sin(b\nu) - \cos(b\nu)\Big) \right. \\
&\quad \left. + \frac{1}{b^{3/2}}\sqrt{\frac{\pi}{4}}\Big(C(\sqrt{\frac{2b\nu}{\pi}}) - S(\sqrt{\frac{2b\nu}{\pi}})\Big) \right]_{\nu_0-\Delta\nu}^{\nu_0+\Delta\nu},
\end{aligned}
\tag{4.14}
$$

where $b = \pi u_0 L z^2/(x(L-x))$ and the functions C and S are the Fresnel cosine integral and sine integral, respectively. Abramowitz and Stegun (1970) give a description of the Fresnel cosine and sine integrals. The sensitivity kernel for a point source using scattering theory for 3-D wave propagation is given by

$$
K(x,y,z) = u_0 L \int_{\nu_0-\Delta\nu}^{\nu_0+\Delta\nu} A(\nu)\nu \frac{\sin\left(\pi\nu u_0 L \frac{y^2+z^2}{x(L-x)}\right)}{x(L-x)} d\nu,
\tag{4.15}
$$

(see Spetzler and Snieder, 2001a for an explanation of how to derive the 3-D scattering theoretical sensitivity kernel in Eq. (4.15)). Assuming a constant power spectrum, the analytical solution of the sensitivity kernel in Eq. (4.15) is found to be

$$
K(x,y,z) = \frac{u_0 L}{2\Delta\nu x(L-x)} \left[-\nu\frac{\cos(b\nu)}{b} + \frac{\sin(b\nu)}{b^2} \right]_{\nu_0-\Delta\nu}^{\nu_0+\Delta\nu}
\tag{4.16}
$$

where $b = \pi u_0 L(y^2+z^2)/(x(L-x))$, (see appendix A). The sensitivity kernel due to the scattering of waves propagating in 2-D and 3-D media is shown in Fig. 4.1A and 4.1B, respectively. We have used Eq. (4.14) to compute the 2-D scattering sensitivity kernel and Eq. (4.16) to evaluate the scattering sensitivity kernel for wave propagation in three dimensions. The sensitivity kernels are calculated for the half source-receiver offset for which the central lobe has the maximum width. The source-receiver distance $L = 8$ cm, the central frequency $\nu_0 = 500$ kHz, the half frequency-band $\Delta\nu = 200$ kHz and the reference slowness $u_0 = 2.5 \times 10^{-4}$ s/m. For both scattering sensitivity kernels in Fig. 4.1, it is seen that the maximum sensitivity to slowness perturbations is off-path the geometrical ray and that the sensitivity kernels have sidelobes. However, the 2-D scattering kernel is non-zero on the ray path and the 3-D scattering kernel vanishes on the geometrical ray. This is a very counter-intuitive result for wave propagation in three dimensions compared with ray theory which predicts non-zero sensitivity to slowness perturbations on the ray. This result is also found in Marquering *et al*. (1998), Tong *et al*. (1998), Marquering *et al*. (1999), Dahlen *et al*. (2000), Hung *et al*. (2000) and Zhao *et al*. (2000) who work with scattering theory in body wave tomography.

   Consider the case that the source-receiver distance is smaller than the correlation length, (e.g. $L/a \ll 1$). This limit corresponds to a medium with a homogeneous slowness

A) 2-D wave propagation

B) 3-D wave propagation
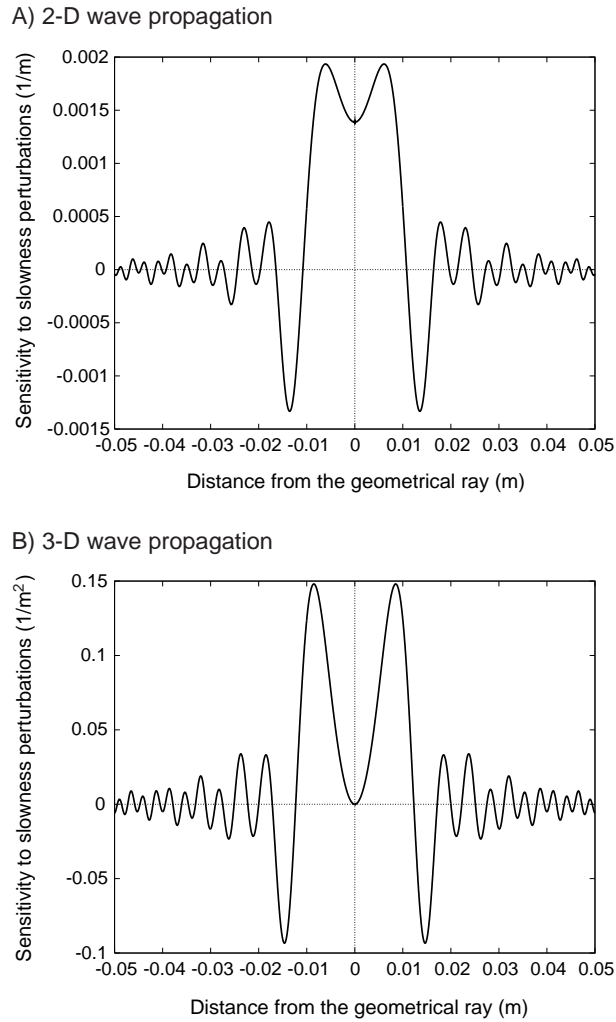
Figure 4.1: *The cross section of the scattering sensitivity kernel. The source-receiver distance $L = 0.08$ m, the reference slowness $u_0 = 2.5 \times 10^{-4}$ s/m, the central frequency $\nu_0 = 500$ kHz and the frequency-band $2\Delta\nu = 400$ kHz. The sensitivity kernels are plotted at the half offset for which the width of the central lobe is maximum. A) The scattering theoretical sensitivity kernel for a point source due to waves propagating in 2-D. B) The sensitivity kernel for a point source due to 3-D scattering theory. Notice that scattering theory in 3-D predicts a zero sensitivity to slowness perturbations on the geometrical ray while according to ray theory there is only non-zero sensitivity to slowness perturbations on the ray path.*

perturbation so the auto-correlation functions in Eq. (4.1) and (4.2) can be set to $(\varepsilon u_0)^2$. The MS-value of timeshift fluctuations using 2-D or 3-D scattering theory in Eq. (4.12) is given by

$$< \left(\delta t\right)^2 > (L) = (\varepsilon u_0 L)^2, \qquad (4.17)$$

which is the same result obtained with ray theory in Eq. (4.6). We derive Eq. (4.17) in appendix B.

Consider instead that the correlation length goes towards zero. It is shown in appendix C that the MS-value of timeshift fluctuations either using 2-D or 3-D scattering theory converges to zero in the limit that the correlation length goes to zero, hence

$$\lim_{a \to 0} < \left(\delta t\right)^2 > (L) \to 0. \qquad (4.18)$$

In this regime, waves propagate in an average medium which is the homogeneous reference medium. The same result can be obtained with Eq. (4.7) for exponential random media and Eq. (4.8) for Gaussian random media using ray theory.

Spetzler and Snieder (2001a) determine in a numerical experiment when the regime of scattering theory is significant. They find that the regime of scattering theory is important when the characteristic length a of heterogeneity is smaller than the width L_F of the Fresnel zone. Hence,

$$\frac{L_F}{a} > 1. \qquad (4.19)$$

Moreover, Spetzler and Snieder (2001a) show that the width of the central lobe of the sensitivity kernels in Fig. 4.1 defines the width of the Fresnel zone. For a more detailed analysis of the properties of the scattering theoretical sensitivity kernel, we refer to Spetzler and Snieder (2001a).

4.3   Setup of the 3-D laboratory experiment

In order to quantify and substantiate the theoretical aspects discussed in the previous sections, we made use of the experimental results from Sivaji *et al*. (2001). The laboratory experiment involves measurements of ultrasonic waves propagating in various rock media. The schematic of the experiment is given in Fig. 4.2. The dimensions of the rock samples are 8 cm×30 cm×30 cm. Elastic waves are sent through the rock sample by triggering the Piezo-electric transducer (PZT) with the source function that is a single cycle sine-wave of 500 kHz frequency. The propagating elastic waves generate vibrations in the sample which are detected by a laser Doppler vibrometer (see laser optical unit in Fig. 4.2). A laser beam is made incident on the reflection sheet attached to the sample surface and the Doppler shifted frequency of the reflected laser beam is measured. The reflection sheet reflects the laser beam almost in the incident direction which enables an
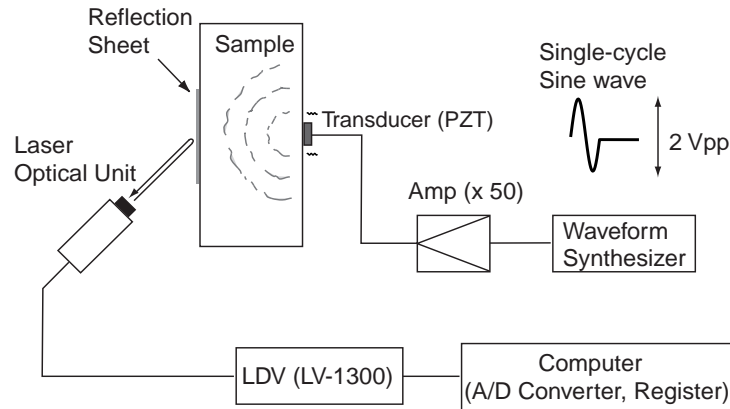
Figure 4.2: *Sketch of the laboratory ultrasonic wave experiment. A 500 kHz single-cycle sine pulse is emitted in the sample at the transducer. Wavefields are recorded with the laser detector and stacked 1000 times to get a clear signal of the waveform.*

accurate measurement in very small aperture. The details of the experiment are elaborated in Nishizawa *et al.* (1997, 1998).

Sivaji *et al.* (2001) performed the waveform measurements on a homogeneous steel sample and heterogeneous granite samples (i.e. Westerly and Oshima). A photo of the micro-structure of Westerly and Oshima granite is shown in Fig. 4.3. The measurements were carried out over a small aperture grid of length 10 mm and spacing of 1 mm. Sivaji *et al.* (2001) related the arrival time and energy fluctuations to the scale-length of heterogeneity. They found a positive correlation between the variance of arrival time/energy fluctuations and the scale-length of heterogeneity. In this paper, we make use of their waveform data to calculate the MS-value of timeshift fluctuations obtained from Westerly and Oshima granite.

For estimating the timeshift of the observed ultrasonic waveforms, we determine the arrival time of the P-wave. First of all, the parabolic equation for spherical waves is applied to correct the P-wave traveltimes for the slightly different source-receiver distance because of the variable receiver position on the reflection sheet. Then we use a Butterworth filter to bandpass-filter the corrected waveforms so that unwanted noise is removed. The bandwidth of the Butterworth filter is determined from the power spectrum of the original waveforms; the central frequency is fixed to 500 kHz and the width of the pass-band is set to 400 kHz. After examining all the bandpass-filtered waveforms, we then estimate the first arrival time of each waveform. We apply the first clear minimum of the waveforms which is close to the first onset time, to obtain the arrival time. The deviations of the measured arrival times from their mean value is then considered as the timeshift variation in the ultrasonic laboratory experiment. The MS-value $< (\delta t)^2 >$ of timeshift fluctuations is calculated by taking the square of the observed timeshifts and

then calculate the mean value. Hence

$$< \left(\delta t \right)^2 >= \frac{1}{M} \sum_{i=1}^{M} \left(\delta t_i \right)^2, \tag{4.20}$$

where the integer M is the number of timeshifts in the sample (see Kreyszip, 1993). The observed MS-value of timeshift fluctuations for Westerly and Oshima granite is 5.1×10^{-16} s^2 and 5.5×10^{-15} s^2, respectively, (see Table 4.1).

In order to access the error in the timeshift picking using the ultrasonic waveforms, we estimated the timeshifts of ultrasonic waves that have propagated through a homogeneous steel sample with the dimensions 8 cm$\times$30 cm$\times$30 cm. The square root of the MS-value of the timeshift variation for steel that is $\sqrt{< (\delta t)^2 >} = 2.76 \times 10^{-8}$ s, is defined as the average error of the timeshift picking in the ultrasonic experiment. Notice that the square root of the MS-value of the timeshift fluctuations for Westerly granite ($\sqrt{< (\delta t)^2 >} = 2.3 \times 10^{-8}$ s) is comparable with the root mean squared value of the timeshift variations for steel. Westerly granite can therefore be considered almost homogeneous.

4.4 Auto-correlation function for Westerly and Oshima granite

The major constituent minerals present in Westerly and Oshima granite are biotite, quartz and plagioclase, identified by the black, grey and white areas in the photos of Westerly and Oshima granite in Fig. 4.3 (Fukushima, 2000). The distribution of these minerals is random in nature with different grain sizes. The grain size in Westerly granite appears to be small compared to that of Oshima granite. The characteristics of random media are described by spatial auto-correlation functions of the slowness and density fluctuations or by their power spectra (Sato and Fehler, 1998). Well-log data are often applied for representing the underground randomness (Wu *et al.*, 1994; Shiomi *et al.*, 1997). Since well-log data are sampled against depth with an equal interval, they are considered as continuous data which can be converted to the slowness or density fluctuations, and their auto-correlation functions are calculated directly from the data. On the other hand, Holliger and Levander (1992, 1994) and Levander *et al.* (1994) applied discrete data based on geological maps in which each rock facies corresponds to the laboratory-measured seismic slowness. We have adopted the second methodology to estimate the scale-length of heterogeneity for Westerly and Oshima granite based on the images of their micro-structure in Fig. 4.3. The micro-structure is assumed isotropic for both granites. The colour-tone distribution of the minerals along a traverse line in the micro-structure images is converted into a tri-mode colour pattern. Then the P-wave slowness values are assigned to each area of the tri-mode colour pattern. We use the Voigt-Reuss averages for the P-wave slowness for quartz ($u_{quartz} = 1.527 \times 10^{-4}$ s/m) and plagioclase ($u_{plagioclase} = 1.639 \times 10^{-4}$ s/m) (Simmons and Wang, 1971). For biotite, we select the slowness randomly from the range between the maximum and minimum P-wave slowness ($u_{min} = 1.282 \times 10^{-4}$ s/m
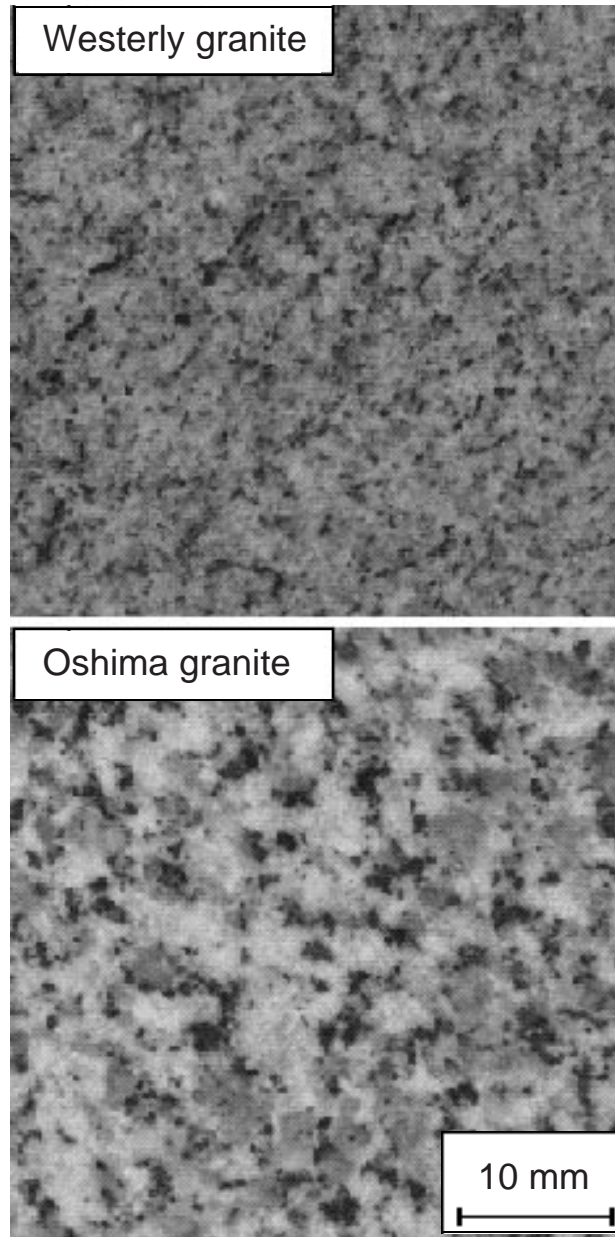
Figure 4.3: *Photograph of Westerly and Oshima granite which shows the micro-structure of the samples. The three major constituent minerals are biotite (black), quartz (grey) and plagioclase (white).*

Sample	v_0 (m/s)	ε (%)	a (mm)	$< \left(\delta t\right)^2 >)$ (s^2)
Westerly granite	4851.9	8.5	0.22	5.1×10^{-16}
Oshima granite	4644.1	9.4	0.46	5.5×10^{-15}

Table 4.1: *The statistical parameters for the exponential auto-correlation function and the MS-value $< (\delta t)^2 >$ of timeshift variations for Westerly and Oshima granite. The reference velocity is denoted v_0, the rms value of relative slowness perturbation is written as ε and the correlation length is denoted a.*

and $u_{max} = 2.375 \times 10^{-4}$ s/m) because of strong anisotropy in biotite (Alekesandrov and Ryzhova, 1961). Therefore slowness fluctuations are controlled mostly by the distribution of biotite minerals and their grain sizes. The slowness perturbation is then calculated by removing the mean slowness value of the slowness distribution. After applying an anti-aliasing filter, the power spectral density function (PSDF) is estimated. This procedure is repeated for 20 profiles and the average PSDF is obtained. The PSDF for Westerly and Oshima are shown in Fig. 4.4A and 4.4B. The auto-correlation function is computed by taking the inverse Fourier transform of the average PSDF. The observed auto-correlation functions that are shown with the solid line in Fig. 4.4C and 4.4D, are fitted by an exponential type auto-correlation function given by Eq.(4.1). The best fitting values for the relative slowness perturbation and correlation length for Westerly and Oshima granite are 8.5 % and 0.22 mm, and 9.4 % and 0.46 mm, respectively, (Table 4.1). The exponential auto-correlation functions with the best fitting values of the relative slowness perturbation and correlation length are plotted with the dashed line in Fig. 4.4C and 4.4D. Notice that the characteristic length of heterogeneity for Oshima granite is about twice as large as that for Westerly granite.

   The width of the Fresnel zone is $L_F = \sqrt{\lambda L} \approx 2.7$ cm for both Westerly granite and Oshima granite using ultrasonic waves with the central frequency equal to 500 kHz ($\lambda = 9.7$ mm for Westerly granite and $\lambda = 9.3$ mm for Oshima granite) and $L = 8$ cm. (The width L_F of the Fresnel zone is derived in Spetzler and Snieder, 2001a.) By comparing the width of the Fresnel zone with the correlation length for Westerly ($a = 0.22$ mm) and Oshima granite ($a = 0.46$ mm), we see that the ultrasonic laboratory experiment is in the regime of scattering theory according to Eq. (4.19).

4.5   2-D numerical experiment to test the stochastic scattering approach

We use a finite-difference (FD) solution of the acoustic wave equation to test the scattering theory for the statistical measurements of the MS-value of timeshifts variations in the real ultrasonic wave experiment. The applied source function is a Ricker wavelet. An incident plane wave is emitted in a 2-D, Cartesian medium and recorded at the source-receiver distance $L = 8$ cm. The waveforms measured at the receiver positions are bandpass-
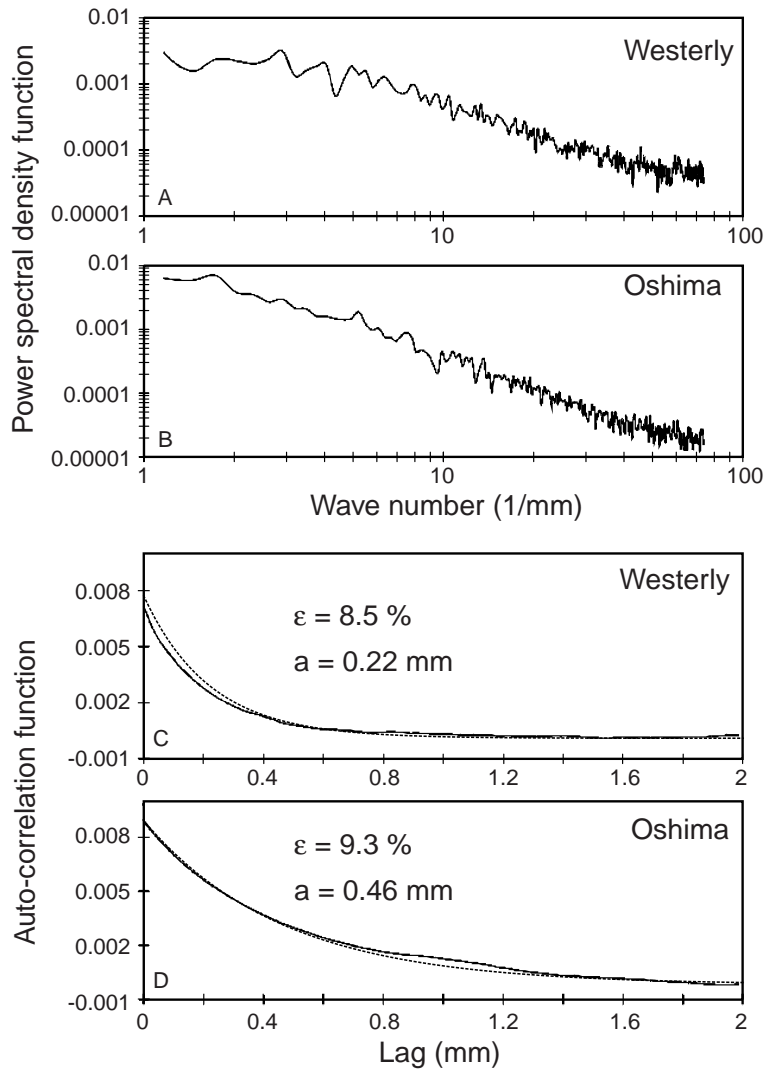
Figure 4.4: *The independent determination of the auto-correlation funtion which describes statistically the slowness perturbation field of Westerly and Oshima granite. A) The PDSF for Westerly granite. B) The PDSF for Oshima granite. C) The auto-correlation function for Westerly granite and its statistical parameters. D) The auto-correlation function for Oshima granite and its stochastic parameters. It is found that the best fitting auto-correlation function to the curve in C) and D) is exponential. The best fitting exponential auto-correlation functions are shown with the dashed line in C) and D).*

filtered between 250 kHz and 1000 kHz. We operate with two slowness fields in the
FD-modeling experiment; the reference slowness field which has the constant reference
slowness $u_0 = 2.5 \times 10^{-4}$ s/m, and the perturbed slowness field with the slowness field
$u(\mathbf{r}) = u_0(\mathbf{r}) + u_1(\mathbf{r})$ where $u_1(\mathbf{r})$ is a realisation of the exponential or Gaussian quasi-
random medium. For both kinds of quasi-random media, we fix the relative slowness
perturbation to 3 % and 10 %, and the correlation length varies between 0.4 mm and 2
mm.

Notice that the mean value of slowness perturbations is not necessarily zero in a finite
sampling of a random medium (see Müller *et al*. 1992). We have corrected the realisations
of the exponential and Gaussian slowness fields by substracting each point of the FD-grid
with the difference between the mean value of the slowness field sample and the reference
slowness u_0. Thereby, each realisation of the exponential and Gaussian random media in
the numerical experiment has the mean value equal to the reference slowness.

The synthetic timeshifts are obtained by comparing the bandpass-filtered reference
waveforms from the constant reference model with the bandpass-filtered perturbed wave-
forms due to the perturbation models. The traveltime of the reference waveform and of
the perturbed waveform is determined using the first clear minimum of the waveforms
as point of measurement. The FD-timeshift is the difference between the reference and
perturbed traveltime. For each distinct correlation length and magnitude of the slowness
perturbation field, five realisations of the exponential and Gaussian random media with
different random seed number are used to generate the FD-timeshifts. For each realisation
of the random media, 150 timeshifts are measured in the FD-experiment. Given the cor-
relation length and magnitude of the slowness perturbation field for either the exponential
media or the Gaussian random media, the MS-value of the sample of the FD-timeshift
fluctuations for every realisation is calculated with Eq. (4.20). It gives five MS-values of
timeshift fluctuations, $<(\delta t)^2>_j$, where $j = 1,..,N$ and $N = 5$, for each combination of
the correlation length and the relative slowness perturbation for the exponential random
media and the Gaussian random media. The average value $<(\delta t)^2>_{ave}$ of the sample of
MS-values of FD-timeshifts for each set of the correlation length and the relative slowness
perturbation field is computed as

$$< \left(\delta t \right)^2 >_{ave} = \frac{1}{N} \sum_{j=1}^{N} < \left(\delta t \right)^2 >_j . \tag{4.21}$$

The standard deviation $\sigma(<(\delta t)^2>)$ of the sample of MS-values of FD-timeshift varia-
tions for each combination of the correlation length and the relative slowness perturbation
field is given by

$$\sigma^2(< \left(\delta t \right)^2 >) = \frac{1}{N-1} \sum_{j=1}^{N} \left(< \left(\delta t \right)^2 >_j - < \left(\delta t \right)^2 >_{ave} \right)^2 , \tag{4.22}$$

(see Kreyszip, 1993). The standard deviation of the sample of the MS-values for FD-
timeshifts is defined as the observed error in the estimation of the MS-value of FD-
timeshifts.

In order to compute the scattering theoretical MS-value of timeshift fluctuations in Eq. (4.12) for exponential and Gaussian random media in the FD-experiment, we must use the 2-D sensitivity kernel for a plane wave due to diffraction theory, hence

$$K(x,z) = \sqrt{u_0} \int_{\nu_0-\Delta\nu}^{\nu_0+\Delta\nu} A(\nu)\sqrt{\nu} \frac{sin\left(\pi\nu u_0 \frac{z^2}{(L-x)} + \frac{\pi}{4}\right)}{\sqrt{L-x}} d\nu, \qquad (4.23)$$

which is explicitly derived in Spetzler and Snieder (2001a). The ray theoretical MS-value of timeshift fluctuations is calculated with Eq. (4.5) wherein the exponential and Gaussian auto-correlation function is inserted.

The width of the Fresnel zone due to a plane wave is about $L_F = \sqrt{3\lambda L} = 3.9$ cm (Spetzler and Snieder, 2001a) for $L = 8$ cm and $\lambda = 1/(u_0\nu_0) = 6.4$ mm. According to Eq. (4.19), we are in the regime of scattering theory using the correlation length $a = 0.4$ mm - 2 mm in the numerical experiment.

4.6 Results

In this section, we present the statistical measurements of the MS-values of timeshift fluctuations from the laboratory experiment and from the FD-numerical experiment. In Fig. 4.5, the theoretical MS-value of timeshift fluctuations for different correlation lengths between 0.15 and 0.55 mm are computed using ray theory (dotted line) in Eq. (4.5) and 3-D scattering theory (dashed line) in Eq. (4.12) for the exponential random medium in the laboratory experiment. Notice that a logarithmic scale is used for the y-axis. The reference slowness and relative slowness perturbation given in Table 4.1 for Oshima granite were applied as statistical model parameters in the exponential auto-correlation function for the two granite samples. The observed MS-value of timeshift perturbations for Westerly ($a = 0.22$ mm) and Oshima ($a = 0.46$ mm) granite is shown with points and errorbars. The size of the errorbars of the MS-value of timeshifts for Westerly and Oshima granite indicates the picking error of the timeshifts in the ultrasonic wave experiment. Westerly granite has a slightly different reference slowness and relative slowness fluctuation than Oshima granite so the observed MS-value of timeshift fluctuations for Westerly granite in Fig. 4.5 has been corrected by multiplying with the factor $(u_0^{Osh}\varepsilon^{Osh})^2/(u_0^{West}\varepsilon^{West})^2$ = 1.33. We see in Fig. 4.5 that ray theory overestimates the observed MS-values of timeshift fluctuations for Westerly and Oshima granite. The MS-value of timeshift variations computed with scattering theory is inside the errorbars of the observed statistical value for Westerly granite and a bit outside the lower errorbar of the observed MS-value for timeshifts for Oshima granite. However, the MS-values of timeshifts that take the scattering of waves into account are in the same order of magnitude as the observed statistical values for Westerly and Oshima granite, while the MS-values of timeshift fluctuations computed with ray theory are a factor 10-15 larger than the stochastic values observed in the ultrasonic wave experiment.

We have simulated the ultrasonic wave experiment with a 2-D numerical experiment which is explained in details in section 4.5. The MS-values of timeshift fluctuations for an
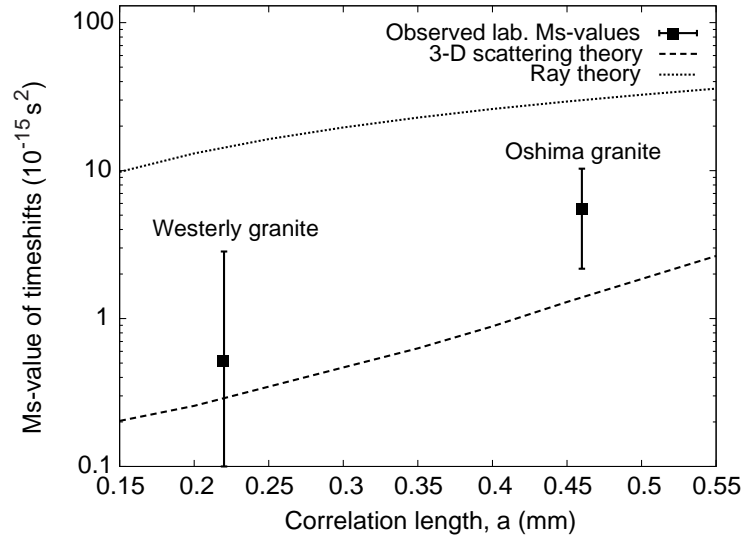
Figure 4.5: *The MS-value of timeshift fluctuations versus the correlation length computed with ray theory (dotted line) and 3-D scattering theory (dashed line) for the exponential random medium in the ultrasonic wave experiment. The offset L = 8 cm, the slowness $u_0 = 2.153 \times 10^{-4}$ s/m and the relative slowness perturbation ε = 9.3 % for Oshima granite. The observed MS-value of timeshift fluctuations from the laboratory experiment is plotted at the correlation length a = 0.22 mm (Westerly) and 0.46 mm (Oshima) with points and errorbars. We see that scattering theory predicts rather well the observed MS-value of timeshift fluctuations obtained from Westerly (within the errorbars) and Oshima granite (just below the errorbars), while ray theory overestimates the observed MS-values of timeshift variations in the laboratory experiment.*

exponential and Gaussian quasi-random medium are shown in Fig. 4.6. The MS-values of timeshift variations computed with ray theory and 2-D scattering theory are shown with the dotted line and dashed line, respectively, while the numerically observed MS-values of timeshift fluctuations for several correlations length are plotted with points and errorbars. In Fig. 4.6A (exponential quasi-random medium) and Fig. 4.6B (Gaussian quasi-random medium), the relative slowness perturbation ε = 3 % and in Fig. 4.6C (exponential quasi-random medium) and Fig. 4.6D (Gaussian quasi-random medium), ε = 10 %. It is seen that 2-D scattering theory predicts the numerically observed MS-values of timeshift perturbations within the errorbars, while the ray theoretical MS-values of timeshift variations are generally too large.

We show in Fig. 4.7 and Fig. 4.8 that 2-D scattering theory (dashed line) is much more accurate than ray theory (dotted line) to predict the FD-timeshifts (solid line) using deter-
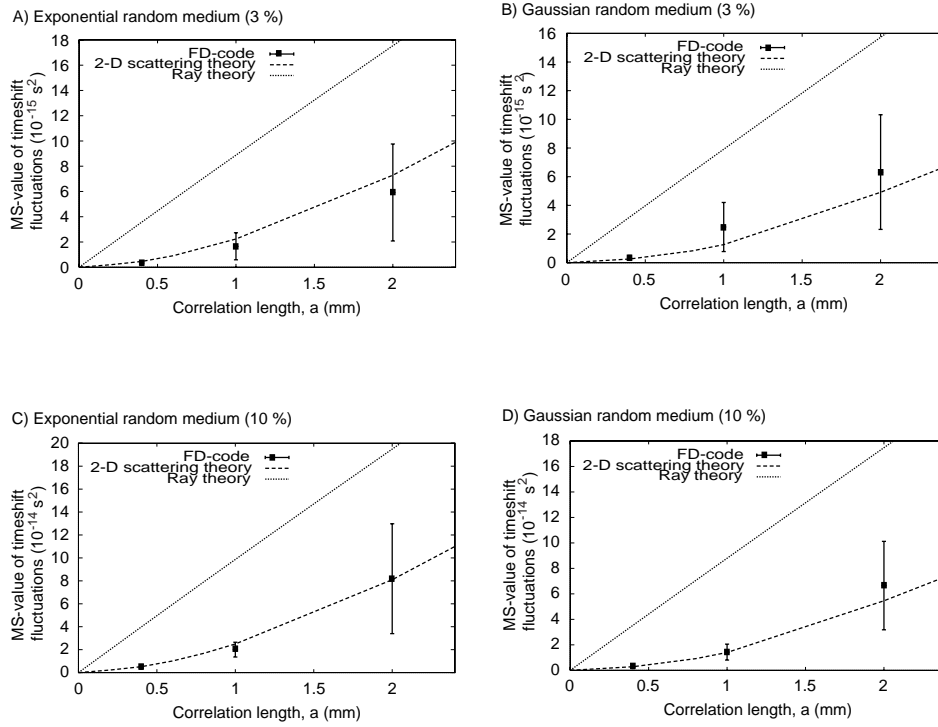
Figure 4.6: *MS-values of timeshift fluctuations for exponential and Gaussian random media with different correlation lengths in the FD-experiment. The reference slowness is 2.5×10^{-4} s/m, the source-receiver offset is 8 cm for an incident plane wave and the frequency-range is from 250 kHz to 1000 kHz. The MS-value of timeshift fluctuations for ray theory is plotted with the dotted line and for scattering theory with the dashed line. The numerical data are computed for the correlation length which is between 0.4 mm and 2 mm. The errorbars show the standard deviation of the numerically observed measurements. A) The exponential random medium with the relative slowness perturbation $\varepsilon = 3$ %. B) The Gaussian random medium with $\varepsilon = 3$ %. C) The exponential random medium with $\varepsilon = 10$ %. D) The Gaussian random medium $\varepsilon = 10$ %. Scattering theory for waves propagating in 2-D is better than ray theory to predict the observed MS-values of timeshift fluctuations computed in the numerical experiment.*

A) Exponential random medium (10 %, a = 0.4 mm)

B) Exponential random medium (10 %, a = 1 mm)

C) Exponential random medium (10 %, a = 2 mm)
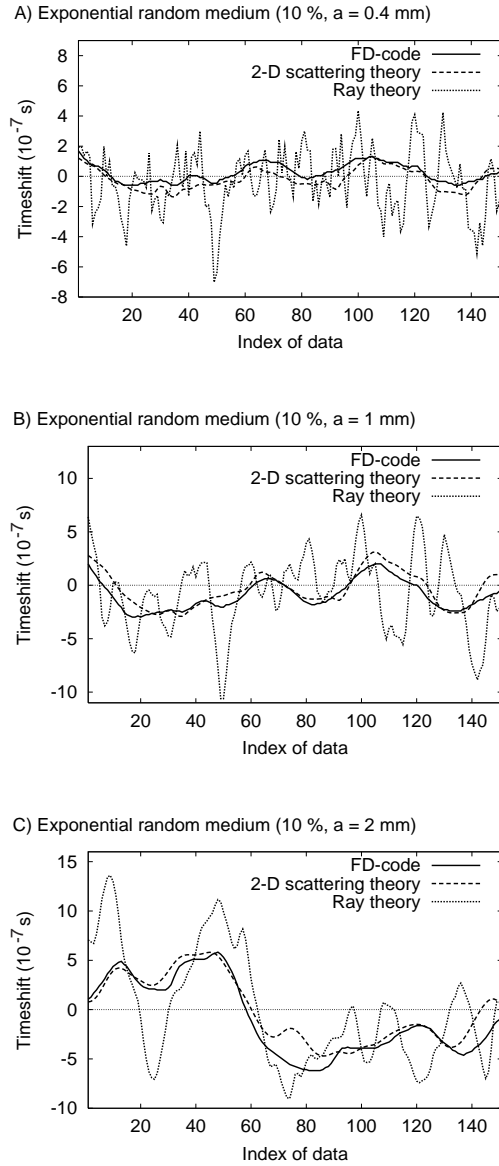
Figure 4.7: *Timeshifts obtained from ray theory, 2-D scattering theory and the FD-solution of the wave equation for different realisations of an exponential quasi-random medium with the reference slowness $u_0 = 2.5 \times 10^{-4}$ s/m and the relative slowness perturbation $\varepsilon = 10$ %. The source-receiver offset $L = 8$ cm for an incident plane wave. The measured waveforms are bandpass-filtered in the frequency-range from 250 kHz to 1000 kHz. A) The correlation length $a = 0.4$ mm, B) $a = 1$ mm and C) $a = 2$ mm.*

A) Gaussian random medium (10 %, a = 0.4 mm)

B) Gaussian random medium (10 %, a = 1 mm)

C) Gaussian random medium (10 %, a = 2 mm)
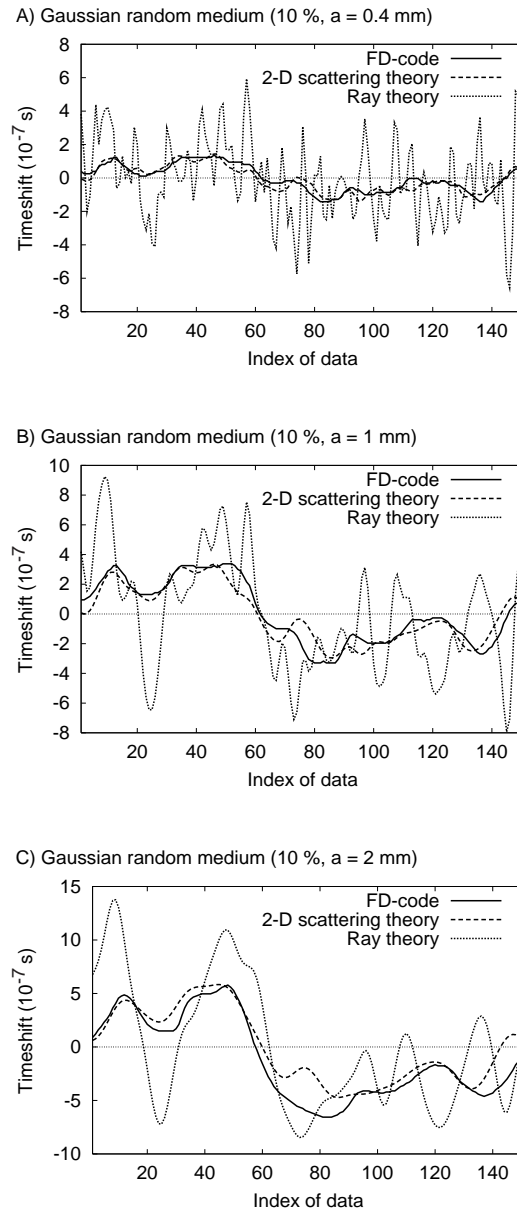
Figure 4.8: *As in Fig. 4.7, but using different realisations of the Gaussian quasi-random medium with the relative slowness perturbation ε = 10 %. A) The correlation length a = 0.4 mm, B) a = 1 mm and C) a = 2 mm.*

ministic realisations of exponential and Gaussian quasi-random media with correlations length smaller in size than the width of the Fresnel zone. The ray theoretical timeshift is calculated with Eq. (4.3) and the timeshift due to scattering theory is computed with Eq. (4.10) using the 2-D sensitivity kernel for a plane wave in Eq. (4.23). For the realisations of exponential quasi-random media and Gaussian quasi-random media with $\varepsilon = 10$ % in Fig. 4.7 and Fig. 4.8, respectively, the correlation length $a = 0.4$, 1 and 2 mm which corresponds to the points for which the numerically observed MS-values of timeshift fluctuations in Fig. 4.6 are computed. In all the figures with the timeshift fluctuations obtained from deterministic realisations of exponential and Gaussian quasi-random media, it is observed that the scattering theoretical timeshift fit the FD-timeshift quite well while ray theory often overestimates the FD-timeshifts.

4.7   Discussion

The results of this study has serious implications for seismic exploration and seismology. We present in Table 4.2 the characteristic values for the wavelength λ , the length L of the ray path between the source and receiver, the width L_F of the Fresnel zone and the length-scale a of slowness anomalies found in present-day tomographic inversions in seismic exploration and seismology. For references, see Parra and Bangs (1992) for vertical seismic profiling tomography (VSP), Goudswaard *et al*. (1998) for crosswell tomography (CT), Hatchell (2000) for reflection seismic (RS), van der Lee and Nolet (1997) for regional surface wave tomography (RSWT), Trampert and Woodhouse (1995) for global surface wave tomography (GSWT) and Bijwaard and Spakman (1998) for global body wave tomography (GBWT). For 3-D wave propagation experiments that is VSP, CT and GBWT, we have used that the maximum width of the Fresnel zone is given by

$$L_F = \sqrt{\lambda L}, \tag{4.24}$$

(Spetzler and Snieder, 2001a) and for RS, the maximum width of the Fresnel zone at the reflector is as well given by Eq. (4.24) but the parameter L is then the two-way length of the wave path from the source to the reflector and back to the receiver. Surface wave tomography (e.g. RSWT and GSWT) is a 2-D wave propagation experiment, so the maximum width of the Fresnel zone on the sphere is given by

$$L_F = \sqrt{\frac{3R\lambda}{2} \tan\left(\frac{L}{2}\right)}, \tag{4.25}$$

where R is the radius of the Earth, and the epicentral distance L is in radians, (see Eq. (35) in Spetzler and Snieder, 2001a). By comparing the width of the Fresnel zone with the characteristic length of inhomogeneity for the different wave experiments in Table 4.2, we see that the regime of scattering theory is important according to Eq. (4.19) in most of the tomographic experiments under consideration.

	λ	L	L_F	a
VSP	5-250 m	300 m	38-274 m	10-15 m
CT	2-10 m	500 m	32-70 m	5-10 m
RS	80 m	200 m (shallow)-8 km (deep)	126-800 m	25-50 m
RSWT	450 km	1-70 deg	200-1735 km	1000 km
GSWT	450 km	20-160 deg	870-4940 km	3000-4000 km
GBWT	6 km	100-20000 km	25-346 km	50-100 km

Table 4.2: *Characteristic values of wave experiments in seismic exploration and seismology. The wavelength is denoted λ, the length of the ray path between the source and receiver is L, the length-scale of observed slowness anomalies is a and the width of the Fresnel zone is written as L_F. The following abbreviations are used; VSP: vertical seismic profiling, CT: crosswell tomography, RS: reflection seismic, RSWT: regional surface wave tomography, GSWT: global surface wave tomography and GBWT: global body wave tomography.*

4.8   Conclusions

We have shown evidence that scattering theory is more accurate than ray theory to predict timeshifts for media with length-scales of inhomogeneity smaller in size than the width of the Fresnel zone. We used a stochastic approach to compute the MS-value of timeshift variations using ray theory and scattering theory because the slowness perturbation field of Westerly and Oshima granite used in the laboratory experiment could be described rather well as an exponential random medium. We compared the MS-value of the observed timeshift distribution for Westerly and Oshima granite in the ultrasonic wave experiment with those calculated theoretically with ray and scattering theory wherein the statistical parameters for the two granite samples were applied. Interestingly, we saw that ray theory would predict too large MS-values of timeshift variations, while scattering theory gave well-fitting values which are close to the observed MS-values of timeshift fluctuations for Westerly and Oshima granite. The result of the laboratory experiment was simulated with a numerical FD-experiment using small-scale structured random media. In the numerical experiment, we showed that scattering theory is better than ray theory to fit both the MS-value of FD-timeshifts from different stochastic models and the FD-time delays measured in deterministic realisations of the random media.

Present-day tomographic models in seismic exploration and seismology are at the edge to explore Earth models with structures smaller than the width of the Fresnel zone. It is therefore necessary to incorporate the finite-frequency effect of waves in seismic reconstruction techniques so that we can get more reliable small-scale models of the Earth. In addition, the applied scattering theory in this paper is a linear theory which makes it just as easy to apply as ray theory. It is therefore feasible in the near-future to incorporate the non-ray geometrical effect into tomographic imaging techniques.

References

Abramowitz M. and Stegun I. A. (**1970**). *Handbook of mathematical functions with formulas, graphs and mathematical tables* (Dover Publications, Inc.).

Alekesandrov K. S. and Ryzhova T. V. (**1961**). The elastic properties of rock-forming minerals, II: Layered silicates, Izv. Acad. Sci. USSR, Geophys. Ser. **12**, 186-189.

Bijwaard H. and Spakman W. (**1998**). Closing the gab between regional and global travel time tomography, Geophys. Res. Lett. **103**, 30055-30078.

Bleistein N. (**1984**). *Mathematical methods for wave phenomena* (Academic Press, Orlanda, FL.).

Curtis A., Trampert J., Snieder R. and Dost B. (**1998**). Eurasian fundamental mode surface wave phase velocities and their relationship with tectonic structures, J. Geophys. Res. **103**, 26919-26947.

Dahlen A., Hung S. H. and Nolet G. (**2000**). Fréchet kernels for finite-frequency travel times-I. theory, Geophys. J. Int. **141**, 157-174.

Dubendorff B. and Menke W. (**1986**). Time-domain apparent-attenuation operators for compressional and shear waves: experiment versus single-scattering theory, J. Geophys. Res. **91**, 14023-14032.

Fukushima Y. (**2000**). *Laboratory study on scattering characteristics of shear waves in rock samples* (Master thesis submitted to Tohoku University, Japan, 1-84).

Goudswaard J. C. M., ten Kroode F. P. E., Snieder R. and Verdel A. R. (**1998**). Detection of lateral velocity contrasts by crosswell traveltime tomography, Geophysics **63**, 523-533.

Hatchell P. K. (**2000**). Fault whispers: transmission distortions on prestack seismic reflection data, Geophysics **65**, 377-389.

Holliger K. and Levander A. (**1992**). A stochastic view of lower crustal fabric based on evidence from the Ivrea zone, Geophys. Res. Lett. **19**, 1153-1156.

Holliger K. and Levander A. (**1994**). Seismic structure of gneissic/granite upper crust: geological and petrophysical evidence from the Strone-Ceneri zone (nothern Italy) and implications for crustal seismic exploration, Geophys. J. R. Int. **119**, 497-510.

Hung S. H., Dahlen A. and Nolet G. (**2000**). Fréchet kernels for finite-frequency travel times-II. examples, Geophys. J. Int. **141**, 175-203.

Kreyszig E. (**1993**). *Advanced engineering mathematics* (John Wiley and Sons, Inc.).

van der Lee S. and Nolet G. (**1997**). Upper mantle *S*-velocity structure of North America, J. Geophys. Res. **102**, 22815-22838.

Levander A., England W., Smith S. K., Hobbs R. W., Goff J. A. and Holliger K. (**1994**). Stochastic characterisation and seismic response of upper and middle crustal rocks based on the Lewisian gneiss complex, Scotland, Geophys. J. Int. **119**, 243-259.

Lo T., Toksöz M. N., Xu S. and Wu R. (**1988**). Ultrasonic laboratory tests of geophysical tomographic reconstruction, Geophysics **53**, 947-956.

Marquering H., Nolet G. and Dahlen F. A. (**1998**). Three-dimensional waveform sensitivity kernels, Geophys. J. Int. **132**, 521-534.

Marquering H., Dahlen F. A. and Nolet G. (**1999**). The body-wave traveltime paradox: bananas, doughnuts and 3-D delay-time kernels, Geophys. J. Int. **137**, 805-815.

Matsunami K. (**1991**). Laboratory tests of excitation and attenuation of coda waves using 2-D models of scattered media, Phys. Earth Planet. Interiors **67**, 36-47.

Menke W. and Abbot D. (**1990**). *Geophysical theory* (Columbia University Press, NY.).

Müller G., Roth M. and Korn M. (**1992**). Seismic-wave traveltimes in random media, Geophys. J. Int. (**110**), 29-41.

Nishizawa O., Satoh T., Lei X. and Kuwahara Y. (**1997**). Laboratory studies of seismic wave propagation in inhomogeneous media using a laser Doppler vibrometer, Bull. Seis. Soc. Am. (**87**), 809-823.

Nishizawa O., Satoh T. and Lei X. (**1998**). Detection of shear waves in ultrasonic range by using a laser Doppler vibrometer, Reviews of Scientific Instruments (**69**), 1-2.

Parra J. O. and Bangs J. H. (**1992**). High-resolution reverse VSP and interwell seismic experiments at the Buckhorn test site in Illinois, *62nd Annual Internat. Mtg., Soc. Expl. Geophys., Expanded Abstracts* 103-107.

Roth M., Müller G. and Snieder R. (**1993**). Velocity shift in random media, Geophys. J. Int. (**115**), 552-563.

Roth M. (**1997**). Statistical interpretation of traveltime fluctuations, Physics of the Earth and Planetary Interiours **104**, 213-225.

Sato H. and Fehler M. (**1998**). *Seismic wave propagation and scattering in the heterogeneous Earth* (Springer Verlag, New York Inc.).

Schultz C. A. and Toksöz M. N. (**1993**). Enhanced backscattering of seismic waves from a highly irregular interface: SH case, Geophys. J. Int. **114**, 91-102.

Schultz C. A. and Toksöz M. N. (**1994**). Enhanced backscattering of seismic waves from a highly irregular interface: P-SV case, Geophys. J. Int. **117**, 783-810.

Schultz C. A. and Toksöz M. N. (**1995**). Reflections from a randomly grooved interface: ultrasonic modelling and finite-difference calculation, Geophys. Prospec. **43**, 581-594.

Shiomi K., Sato H. and Ohtake M. (**1997**). Broad-band power-law spectra of well-log data in Japan, Geophys. J. Int. **130**, 57-64.

Simmons G. and Wang H. (**1971**). *Single crystal elastic constants and calculated aggregate properties*, Handbook 2nd Ed. (MIT Press, Cambridge and London.).

Sivaji C., Nishizawa O. and Fukushima Y. (**2001**). Relationship between fluctuations of arrival time and energy of seismic waves and scale-length of heterogeneity: an inference from experimental study, Bull. Seis. Soc. Am. (**in press**), April.

Snieder R. and Sambridge A. (**1992**). Ray perturbation theory for traveltimes and ray paths in 3-D heterogeneous media, Geophys. J. Int. **109**, 294-322.

Snieder R. and Lomax A. (**1996**). Wavefield smoothing and the effect of rough velocity perturbations on arrival times and amplitudes, Geophys. J. Int. **125**, 796-812.

Spetzler J. and Snieder R. (**2001a**). The effects of small-scale heterogeneity on the arrival time of waves, Geophys. J. Int. (**145**), In press.

Spetzler J., and Snieder R. (**2001b**). The formation of caustics in two and three dimensional media, Geophys. J. Int. **144**, 175-182.

Tong J., Dahlen F. A., Nolet G. and Marquering H. (**1998**). Diffraction effects upon finite-frequency traveltimes: a Simple 2-D Example, Geophys. Res. Lett. **25**, 1983-1986.

Trampert J. and Woodhouse J. H. (**1995**). Global phase velocity maps of Love and Rayleigh waves between 40 and 150 seconds, Geophys. J. Int. **122**, 675-690.

Yomogida K. and Aki K. (**1987**). Amplitude and phase data inversion for phase velocity anomalies in the Pacific ocean basin, Geophys. J. R. astr. Soc. **88**, 161-204.

Yomogida K. (**1992**). Fresnel zone inversion for lateral heterogeneities in the Earth, Pure Appl. Geophys., **138** (3), 391-406.

Vinogradov S. D., Troitsky P. A. and Solovyeva M. S. (**1989**). Influence of fracturing and stresses on the propagation of elastic waves, Izvestiya Earth Physics, **25**, 293-303.

Vinogradov S. D., Troitsky P. A. and Solovyeva M. S. (**1992**). Study of propagation of elastic waves in medium with oriented cracks, Izvestiya Earth Physics, **28**, 367-383.

Woodward M. J. (**1992**). Wave-equation tomography, Geophys., **57**, 15-26.

Wu, R. S., Xu, Z. and Li X. P. (**1994**). Heterogeneity spectrum and scale-anisotropy in the upper crust revealed by the German Continental deep-drilling (KTB) holes, Geophys. Res. Lett. **21**, 911-914.

Zhao L., Jordan T. H. and Chapman C. H. (**2000**). Three-dimensional Fréchet differential kernels for seismic delay times, Geophys. J. Int. **141**, 558-576.

4.9 Appendix A: Analytical integration over a constant frequency-band

To derive the analytical solution of the 2-D scattering sensitivity kernel in Eq. (4.14), we use that the integration of the functional $\sqrt{\nu}\sin(b\nu + \pi/4)$ is given by

$$
\int \sqrt{\nu}\sin(b\nu + \frac{\pi}{4})d\nu = \frac{\sqrt{\nu}}{\sqrt{2}b}\left(\sin(b\nu) - \cos(b\nu)\right)
$$
$$
+ \frac{\sqrt{\frac{\pi}{4}}}{b^{3/2}}\left(C(\sqrt{\frac{2b\nu}{\pi}}) - S(\sqrt{\frac{2b\nu}{x}}\pi)\right), \qquad (4.26)
$$

where the functions C and S are the Fresnel cosine integral and sine integral, respectively. See Abramowitz and Stegun (1970) for a description of the Fresnel cosine and sine integrals. For the 3-D sensitivity kernel due to non-ray geometrical effects in Eq. (4.16), an integration of the functional $\nu\sin(b\nu)$ gives that

$$
\int \nu\sin(b\nu)d\nu = -\frac{\nu\cos(b\nu)}{b} + \frac{\sin(b\nu)}{b^2}. \qquad (4.27)
$$

4.10 Appendix B: The MS-value of timeshift fluctuations using scattering theory in a homogeneous slowness perturbation medium

We derive Eq. (4.17) explicitly for 2-D scattering theory. The source-receiver distance is assumed to be much smaller than the correlation length which allows us to set the exponential function in Eq. (4.1) for exponential random media and in Eq. (4.2) for Gaussian random media to unity. The MS-value of timeshifts fluctuations is then derived

by rewriting Eq. (4.12) as a multiplication of two timeshifts, thus

$$
\begin{aligned}
< \left(\delta t\right)^2 > (L) &= (\varepsilon u_0)^2 \int_0^L \int_0^L \int_{-\infty}^{\infty} \int_{-\infty}^{\infty} K(x',z')K(x'',z'')dx'dz'dx''dz'' \\
&= (\varepsilon u_0)^2 \int_0^L \int_{-\infty}^{\infty} K(x',z')dx'dz' \int_0^L \int_{-\infty}^{\infty} K(x'',z'')dx''dz'' \\
&= (\varepsilon u_0 L)^2,
\end{aligned}
\tag{4.28}
$$

because each scattering theoretical sensitivity kernel integrated over the 2-D volume between the source and receiver is equal to the source-receiver offset L as shown in Eq. (4.29) below. Hence

$$
\begin{aligned}
\int_0^L \int_{-\infty}^{\infty} K(x,z)dzdx &= \sqrt{u_0 L} \int_{v_0-\Delta v}^{v_0+\Delta v} A(v)\sqrt{v} \int_0^L \frac{1}{\sqrt{x(L-x)}} \\
&\quad \times \int_{-\infty}^{\infty} sin\left(v\pi u_0 L \frac{z^2}{x(L-x)} + \frac{\pi}{4}\right)dzdxdv \\
&= \frac{\sqrt{u_0 L}}{2i} \int_{v_0-\Delta v}^{v_0+\Delta v} A(v)\sqrt{v} \int_0^L \frac{1}{\sqrt{x(L-x)}} \\
&\quad \times \int_{-\infty}^{\infty} \left(e^{i(v\pi u_0 L \frac{z^2}{x(L-x)} + \frac{\pi}{4})} - e^{-i(v\pi u_0 L \frac{z^2}{x(L-x)} + \frac{\pi}{4})}\right)dzdxdv \\
&\approx \frac{\sqrt{u_0 L}}{2i} \int_{v_0-\Delta v}^{v_0+\Delta v} A(v)\sqrt{v} \int_0^L \frac{1}{\sqrt{x(L-x)}}\left(2i\sqrt{\frac{x(L-x)}{vu_0 L}}\right)dxdv \\
&= \int_{v_0-\Delta v}^{v_0+\Delta v} A(v)dv \int_0^L dx = L.
\end{aligned}
\tag{4.29}
$$

Stationary phase theory (Bleistein, 1984) is applied to evaluate the integration of the variable z between $-\infty$ and ∞. A similar derivation holds for 3-D scattering theory for a point source and for the 2-D diffraction sensitivity kernel for a plane wave.

4.11   Appendix C: The converging of the MS-value of time shift fluctuations towards zero when the correlation length goes to zero

In this appendix, Eq. (4.18) is derived explicitly for 2-D scattering theory. A similar derivation is valid for the scattering of waves propagating in 3-D. The following integration technique can also be found in Roth *et al*. (1993) and in Spetzler and Snieder (2001b). Let

$$
f(r) = < \delta u(x',z')\delta u(x'',z'') >,
\tag{4.30}
$$

and

$$
\eta(x',x'',z',z'') = K(x',z')K(x'',z'').
\tag{4.31}
$$

The MS-value of timeshift fluctuations for scattering theory of 2-D propagating waves in
Eq. (4.12) is then written as

$$< \left(\delta t \right)^2 > (L) = \int_{-\infty}^{\infty} \int_{-\infty}^{\infty} \int_0^L \int_0^L f(r) \eta(x', x'', z', z'') dx' dz' dx'' dz''. \qquad (4.32)$$

The distance $r = \sqrt{l^2 + (z' - z'')^2}$ and $l = |x' - x''|$. We split the integration of the variable
x'' in Eq. (4.32) into two parts; one integration from zero to x' and another integration from
x' to L. The MS-value of timeshift fluctuations is then written as

$$
\begin{aligned}
< \left(\delta t \right)^2 > (L) &= \int_{-\infty}^{\infty} dz' \int_{-\infty}^{\infty} dz'' \int_0^L dx' \\
&\times \left[\int_0^{x'} f(r) \eta(x', x'', z', z'') dx'' \right. \\
&\left. + \int_{x'}^L f(r) \eta(x', x'', z', z'') dx'' \right].
\end{aligned}
\qquad (4.33)
$$

Define $l = x' - x''$ and $l = x'' - x'$ for the first and second integration of x'' inside the
squared brackets, respectively. Making a change of variable, we obtain that

$$
\begin{aligned}
< \left(\delta t \right)^2 > (L) &= \int_{-\infty}^{\infty} dz' \int_{-\infty}^{\infty} dz'' \int_0^L dx' \\
&\times \left[\int_0^{x'} f(r) \eta(x', x' - l, z', z'') dl \right. \\
&\left. + \int_0^{L-x'} f(r) \eta(x', x' + l, z', z'') dl \right].
\end{aligned}
\qquad (4.34)
$$

As shown explicitly in appendix A of Spetzler and Snieder (2001b), we can change the
order of integration of the variable x' and l in Eq. (4.34). Moreover, the auto-correlation
function $f(r)$ depends on l and can be removed outside the squared brackets. The final
result of the MS-value of timeshift fluctuations for waves propagating in 2-D media is
written as

$$
\begin{aligned}
< \left(\delta t \right)^2 > (L) &= \int_{-\infty}^{\infty} dz' \int_{-\infty}^{\infty} dz'' \int_0^L dl f\left(\sqrt{l^2 + (z' - z'')^2} \right) \\
&\times \left[\int_l^L \eta(x', x' - l, z', z'') dx' \right. \\
&\left. + \int_0^{L-l} \eta(x', x' + l, z', z'') dx' \right],
\end{aligned}
\qquad (4.35)
$$

where we explicitly write $r = \sqrt{l^2 + (z' - z'')^2}$ in the auto-correlation function. Finally,
we can investigate what happens to the scattering theoretical MS-value of timeshift fluc-
tuations in the limit that the correlation length goes to zero. In that particular case, the
auto-correlation function

$$
f\left(\sqrt{l^2 + (z' - z'')^2} \right) = \begin{cases} (\varepsilon u_0)^2 & \text{if } z' = z'' \text{ and } l = 0 \\ 0 & \text{if } l \neq 0 \end{cases}
\qquad (4.36)
$$

We see that the auto-correlation function in Eq. (4.36) is only non-zero for the variable $l = 0$. This means that the MS-value of timeshift fluctuations using 2-D scattering theory converges towards zero in the limit that the correlation length goes to zero because the integration of the variable l in Eq. (4.35) yields zero.

Chapter 5

The effect of scattering in surface wave tomography

Abstract.

We present a new technique in surface wave tomography which takes the finite-frequency of surface waves into account using first-order scattering theory in a SNREI Earth. Physically, propagating surface waves with a finite-frequency are diffracted by heterogeneity distributed on a sphere and then interfere at the receiver position. Paradoxically, surface waves have the largest sensitivity to velocity anomalies off-path the geometrical ray. The non-ray geometrical effect is increasingly important for increasing period and distance. Therefore, it is expected that the violation of ray theory in surface wave tomography is most significant for the longest periods.

We applied scattering theory to phaseshift measurements of Love waves between periods of 40 s and 150 s to obtain global phase velocity maps expanded in spherical harmonics to angular degree and order 40. These models obtained with scattering theory were compared with those constructed with ray theory. We observed that ray theory and scattering theory predict the same structure in the phase velocity maps to degree and order 25-30 for Love waves at 40 s and to degree and order 12-15 for Love waves at 150 s. A smoothness condition was included in the phaseshift inversion for phase velocity maps, so we could not access the structure with smaller length-scale of velocity anomalies in the obtained Earth models.

We carried out a synthetic experiment for phase and group velocity measurements to investigate the limits of classical ray theory in surface wave tomography. In the synthetic experiment, we computed, using the source-receiver paths in the surface wave dataset, the discrepancy between ray theoretical and scattering theoretical phase velocity measurements and group velocity measurements, respectively, for an input-model with slowness heterogeneity for increasing angular degree. We found that classical ray theory in global surface wave tomography is only applicable for structures with angular degrees smaller

than 30 (equivalent to 1300 km) and 20 (equivalent to 2000 km) for Love waves at 40 s and 150 s, respectively. The synthetic experiment suggests that the ray theoretical great circle approximation is appropriate to use in present-day global surface wave tomography. On the other hand, in order to obtain reliable global models with a higher resolution we must take the non-ray geometrical effect of surface waves into account.

5.1   Introduction

In surface wave tomography, global as well as regional models are obtained with increasing resolution. This increase in spatial resolution allows a comparison between tomographic models and detailed tectonic features. Most techniques for surface wave tomography are based on simplified versions of ray theory; see Backus (1964), Dziewonski (1984), Woodhouse and Dziewonski (1984), Trampert and Woodhouse (1995), van der Lee and Nolet (1997) and van Heijst and Woodhouse (1999) who all apply the great circle approximation to compute Earth models from surface wave data. However, ray theory introduces an inconsistency from a methodological point of view. It is only valid if the length-scale of velocity perturbations is larger than the wavelength and the width of the Fresnel zone. This condition is often violated for high-resolution S-velocity models compiled with ray theory because the characteristic length of heterogeneity in present surface wave models is comparable with the width of Fresnel zones (Passier and Snieder, 1995).

Several examples of scattering theory to explain wave propagation in heterogeneous media are given in the literature. Yomogida and Aki (1987), Yomogida (1992), Woodward (1992), Snieder and Lomax (1996) and Spetzler and Snieder (2001) use the Rytov approximation to derive the frequency-depending timeshift. In Spetzler and Snieder (2001), it is demonstrated explicitly that the timeshift can be computed as an integration of the slowness perturbation field multiplied by a sensitivity kernel (also known as the Fréchet kernel). Furthermore, Spetzler and Snieder (2001) confirm through a numerical experiment that the regime of scattering theory is important when the length-scale of inhomogeneity is smaller than the width of the Fresnel zone. Woodhouse and Girnuis (1982) and Snieder (1993) use normal mode theory to compute the Fréchet kernel for degree l and order m in surface wave tomography using spherical harmonics to expand the slowness perturbation field. Marquering *et al.* (1998), Tong *et al.* (1998), Marquering *et al.* (1999), Dahlen *et al.* (2000), Hung *et al.* (2000) and Zhao *et al.* (2000) apply a cross-correlation function to introduce the frequency-dependent timeshift in body wave tomography. It is shown in several of these articles that the sensitivity kernel for 3-D wave propagation vanishes on the geometrical ray and that the maximum sensitivity to slowness perturbations is off-path the ray. However surface wave tomography is a 2-D problem and the scattering theoretical sensitivity to slowness perturbations is non-zero on the ray path.

In this study, we develop a frequency-dependent scattering theory for minor and major arc surface waves by using the first-order Rytov approximation. The theory is applicable for unconverted surface waves in a SNREI Earth model. The scattering theory can be applied to both phase and group velocity measurements. Given the same strength of inhomogeneity, diffraction of surface waves becomes increasingly important when the

dominant period in the phaseshift dataset or the source-receiver distance increases. It is shown how relative phaseshifts and timeshifts measured from surface waves are linearly related to the coefficients of the spherical harmonics for relative phase and group velocity, respectively. Relative phaseshift measurements for Love waves at 40 s and 150 s from Trampert and Woodhouse (2001) are then inverted to obtain phase velocity maps using scattering theory.

We show a synthetic experiment wherein given the source-receiver paths in the surface wave data set the relative error introduced by ray theory is computed for slowness heterogeneities with increasing angular degree. The synthetic experiment shows that the diffraction of surface waves is dominant if the structure of the Earth exceeds the angular degree 20 (corresponds to the length-scale of inhomogeneity of about 2000 km) for surface waves at 150 s and angular degree 30 (the characteristic length of heterogeneity is 1300 km) for surface waves at 40 s. This is close to the current limit of resolution using ray theory that we obtain in the phase velocity maps in this article.

In section 5.2, the width of the Fresnel zone for surface waves is derived, and it is shown how to relate surface wave measurements (i.e. relative phaseshift and timeshift) with relative phase and group velocity perturbations on a sphere using ray theory and scattering theory. In addition, the properties of the obtained Fréchet kernels are discussed. In section 5.3, the setup of the surface wave experiment using Love waves between periods of 40 s and 150 s is explained. In section 5.4, the results of the inversion of relative phaseshifts for Love and Rayleigh waves at 40 s and 150 s are given. In section 5.5, a discussion of the small-scale structures of the Earth is given, and thereby the synthetic experiment is shown. The conclusions are drawn in section 5.6.

5.2 Theory

5.2.1 The width of Fresnel zones on the sphere

Fresnel zones are defined in terms of the difference in propagation length of rays with adjacent paths. The points inside the Fresnel zone are those points giving single-scattered waves which have a detour smaller than a certain fraction of the wavelength λ compared with the ballistic ray (e.g. Kravtsov, 1988). This fraction of the wavelength is denoted λ/n, where the number $n = 8/3$ for waves propagating in two dimensions (Spetzler and Snieder 2001). Physically, waves scattered by points inside the first Fresnel zone interfere constructively at the receiver position. In the rest of this paper, the Fresnel zone refers strictly speaking to the first Fresnel zone. It is shown in appendix A how to derive the maximum width of Fresnel zones on the sphere. The epicentral distance between a given source and receiver geometry is denoted Δ_{off}. The maximum width L_F of Fresnel zones in radians is then given by

$$L_F = \sqrt{\frac{3\lambda}{2} \tan\left(\frac{\Delta_{\text{off}}}{2}\right)}, \tag{5.1}$$

where $\Delta_{\text{off}} \in [0, \pi]$ and the wavelength is in radians. The width of Fresnel zones increases with increasing wavelength and epicentral distance. In the limit that the source-receiver distance goes towards π, the Fresnel zone converges to the whole sphere. The formula in Eq. (5.1) is derived using second order perturbation theory. Accordingly, the tangent function goes to infinity for the source-receiver offset Δ_{off} going to π (i.e. the approximation breaks down).

5.2.2 Phase and group velocity maps using ray theory

Trampert and Woodhouse (1995) apply the ray theoretical great circle approximation (e.g. Backus, 1964; Jordan, 1978; Dahlen, 1979) to write the relative phaseshift $\delta\varphi/\varphi_0$ for minor arcs (i.e. $0 < \Delta_{\text{off}} < \pi$) and major arcs (i.e. $\pi < \Delta_{\text{off}} < 2\pi$) as the relative velocity perturbation $\delta v/v_0$ averaged over the ray path between the source and receiver, hence

$$\frac{\delta\varphi}{\varphi_0}(\Delta_{\text{off}}) = -\frac{1}{\Delta_{\text{off}}} \int_{\mathbf{r}_S}^{\mathbf{r}_R} \frac{\delta v}{v_0}(\theta, \varphi) dr, \tag{5.2}$$

where dr is in radians. The location of the source and receiver on the unit sphere is denoted $\mathbf{r}_S$ and $\mathbf{r}_R$, respectively, and the epicentral distance between the source and receiver is Δ_{off}. In addition, Trampert and Woodhouse (1995) write the relative velocity perturbation as a summation of spherical harmonics, thus

$$\frac{\delta v}{v_0}(\theta, \varphi) = \sum_{l=0}^{l_{max}} \sum_{m=-l}^{l} C_l^m Y_l^m(\theta, \varphi). \tag{5.3}$$

The upper limit in the spherical expansion of the relative velocity perturbation is denoted l_{max}, and the coefficient of spherical harmonics to angular degree l and order m for relative phase velocity is written as C_l^m. The relative phaseshift is then expressed in spherical harmonics by inserting Eq. (5.3) in Eq. (5.2) which gives that

$$\frac{\delta\varphi}{\varphi_0}(\Delta_{\text{off}}) = \sum_{l=0}^{l_{max}} \sum_{m=-l}^{m=l} C_l^m K_{l,m}^{ray,ph}(\Delta_{\text{off}}), \tag{5.4}$$

with the ray theoretical sensitivity kernel for angular degree l and order m equal to

$$K_{l,m}^{ray,ph}(\Delta_{\text{off}}) = -\frac{1}{\Delta_{\text{off}}} \int_{\mathbf{r}_S}^{\mathbf{r}_R} Y_l^m(\theta, \varphi) dr. \tag{5.5}$$

Similarly, group velocity maps are retrieved from time delays obtained by bandpass-filtered surface waveforms in a frequency-band $2\Delta v$ around the central frequency v_0. In terms for ray theory, the timeshift $\delta t(\Delta_{\text{off}}) = \delta\varphi(\Delta_{\text{off}})/(2\pi v)$ at offset Δ_{off} is given by

$$\delta t(\Delta_{\text{off}}) = \sum_{l=0}^{l_{max}} \sum_{m=-l}^{m=l} U_l^m K_{l,m}^{ray,gr}(\Delta_{\text{off}}), \tag{5.6}$$

where the coefficient of spherical harmonics to degree l and order m for relative group velocity is denoted U_l^m, and the sensitivity kernel for relative group velocity is

$$K_{l,m}^{ray,gr}(\Delta_{\text{off}}) = -\frac{R}{v_0} \int_{\mathbf{r}_S}^{\mathbf{r}_R} Y_l^m(\theta, \varphi) dr. \tag{5.7}$$

The reference velocity at the central frequency is denoted v_0, and R is the radius of the Earth.

Ray theory is valid when the characteristic length a of heterogeneity is much larger than the wavelength λ and the width of Fresnel zones L_F. Hence in non-dimensional numbers the condition for ray theory is written as;

$$\frac{\lambda}{a} \ll 1, \qquad \text{and} \qquad \frac{L_F}{a} \ll 1, \tag{5.8}$$

see Menke and Abbot (1990).

5.2.3 Phase and group velocity maps using to scattering theory

The theory of diffracted surface waves is developed for minor and major arc measurements using the first-order Rytov approximation. First the relative phaseshift for minor arcs is derived for a reference system using co-latitude coordinates with the source position at $(\pi/2, 0)$ and the receiver position at $(\pi/2, \Delta_{\text{off}})$. We derive the scattering sensitivity kernels that relate the relative phaseshift and the time residual linearly with the relative phase and group velocity, respectively, that are expanded in spherical harmonics. Then, we show how surface wave measurements for major arcs using scattering theory are derived from the developed theory for minor arcs. Finally, we show that phase and group velocity measurements for any source-receiver configuration can be computed in a fast way by rotating tabulated sensitivity kernels in the reference system.

Snieder and Nolet (1987) and Snieder and Romanowicz (1988) linearise the Lamé coefficients λ and μ and the density ρ to write the Born vector wavefield $\mathbf{u}_1(\mathbf{r}_r)$ as

$$\begin{aligned}
\mathbf{u}_1(\mathbf{r}_r) &= \mathbf{P}(R, \theta_r, \varphi_r)[\mathbf{P}(R, \theta_s, \varphi_s) \cdot \mathbf{F}] \\
&\times \int_0^{\Delta_{\text{off}}} \int_0^{\pi} \frac{\exp i(kR\Delta_2 + \frac{\pi}{4})}{\sqrt{\frac{\pi}{2}kR\sin(\Delta_2)}} V(R, \theta, \varphi) \\
&\times \frac{\exp i(kR\Delta_1 + \frac{\pi}{4})}{\sqrt{\frac{\pi}{2}kR\sin(\Delta_1)}} R^2 \sin(\theta) d\theta d\varphi,
\end{aligned} \tag{5.9}$$

which is derived for wave propagation on the sphere. The adiabatic assumption (i.e. there is no mode conversion between different modes of Love and Rayleigh waves) is applied in Eq. (5.9) so there is no summation over modes and mode conversions are absent. The polarisation vector at the source (R, θ_s, φ_s) and at the receiver (R, θ_r, φ_r) is $\mathbf{P}$, the wavenumber is k for surface waves, the epicentral distances between the source and scatterer and between the scatterer and receiver are denoted Δ_1 and Δ_2, respectively, the Fourier transform of the point source function is $\mathbf{F}$ and the scattering coefficient

is V. The expression in Eq. (5.9) then reads as follows; The polarised point source $\mathbf{P}(R,\theta_s,\varphi_s)\cdot\mathbf{F}$ excites the surface wave. The surface wave propagates to the scattering point (R,θ,φ); the phaseshift and the geometrical factor are determined by the propagating term $\exp i(kR\Delta_1 + \frac{\pi}{4})/\sqrt{\frac{\pi}{2}kR\sin(\Delta_1)}$. The wavefield is scattered with an amplitude determined by the interaction term V. The scattered wavefield propagates to the receiver; the phaseshift and the geometrical factor are determined by the propagating term $\exp i(kR\Delta_2 + \frac{\pi}{4})/\sqrt{\frac{\pi}{2}kR\sin(\Delta_2)}$. Finally the recorded signal is given by the polarisation $\mathbf{P}(R,\theta_r,\varphi_r)$. Snieder (1986) shows that for unconverted surface waves the interaction term V can be written as

$$V(R,\theta,\varphi) = -\frac{k^2}{2}\frac{\delta v}{v_0}(R,\theta,\varphi), \qquad (5.10)$$

where the reference phase velocity and the phase velocity perturbation is v_0 and δv, respectively.

Given the measurement of the i-component of the displacement, the phaseshift $\delta\varphi^{(i)}$ $(\Delta_{\mathrm{off}},\nu)$ of the surface waves is obtained from

$$\delta\varphi^{(i)}(\Delta_{\mathrm{off}},\nu) = Im\{\frac{u_1^i(\mathbf{r}_r)}{u_0^i(\mathbf{r}_r)}\}, \qquad (5.11)$$

where the unperturbed vector wavefield $\mathbf{u}_0(\mathbf{r}_r)$ is given by

$$\mathbf{u}_0(\mathbf{r}_r) = \mathbf{P}(R,\theta_r,\varphi_r)\frac{\exp i(kR\Delta_{\mathrm{off}} + \frac{\pi}{4})}{\sqrt{\frac{\pi}{2}kR\sin(\Delta_{\mathrm{off}})}}[\mathbf{P}(R,\theta_s,\varphi_s)\cdot\mathbf{F}], \qquad (5.12)$$

for the epicentral distance Δ_{off} between the source and receiver (Snieder, 1986). The expression in Eq. (5.11) generalises the Rytov approximation (e.g. Yomogida and Aki, 1987; Snieder and Lomax, 1996; Spetzler and Snieder, 2001) to elastic waves.

The detour $\Delta_1 + \Delta_2 - \Delta_{\mathrm{off}}$ and the geometrical factors $\sin(\Delta_1)$ and $\sin(\Delta_2)$ in Eq. (5.9) are perturbed to second and zeroth order in the path deflection $(\theta - \frac{\pi}{2})$, respectively. For a source-receiver geometry along the equator line, the detour is given by

$$\Delta_1 + \Delta_2 - \Delta_{\mathrm{off}} \approx \frac{(\theta - \frac{\pi}{2})^2}{2}\frac{\sin(\Delta_{\mathrm{off}})}{\sin(\varphi)\sin(\Delta_{\mathrm{off}} - \varphi)}, \qquad (5.13)$$

and the geometrical factors are

$$\sin(\Delta_1) \approx \sin(\varphi), \qquad \text{and} \qquad \sin(\Delta_2) \approx \sin(\Delta_{\mathrm{off}} - \varphi), \qquad (5.14)$$

(see appendix A). The relative phaseshift $\delta\varphi^{(i)}/\varphi_0(\Delta_{\mathrm{off}},\nu)$ for the ith receiver is derived by inserting Eq. (5.9), (5.10) and (5.12) in Eq. (5.11), then dividing with the phase $\varphi_0 = kR\Delta_{\mathrm{off}}$ and finally using the Taylor approximation for the detour and for the geometrical factors in Eq. (5.13) and (5.14), respectively, thus

$$\frac{\delta\varphi^{(i)}}{\varphi_0}(\Delta_{\mathrm{off}},\nu) = \int_0^{\Delta_{\mathrm{off}}}\int_0^{\pi}K(R,\theta,\varphi)\frac{\delta v}{v_0}(R,\theta,\varphi)d\theta d\varphi, \qquad (5.15)$$

where the wavenumber $k = 2\pi v / v_0$, and the sensitivity kernel $K(R, \theta, \varphi)$ for the relative velocity perturbation field is given by

$$K(R, \theta, \varphi) = -\frac{\sin(\theta)}{\Delta_{\text{off}}} \sqrt{\frac{vR\sin(\Delta_{\text{off}})}{v_0}} \frac{\sin\left(\frac{\pi v R}{v_0}(\theta - \frac{\pi}{2})^2 \frac{\sin(\Delta_{\text{off}})}{\sin(\varphi)\sin(\Delta_{\text{off}} - \varphi)} + \frac{\pi}{4}\right)}{\sqrt{\sin(\varphi)\sin(\Delta_{\text{off}} - \varphi)}} \quad (5.16)$$

The relative velocity perturbation $\frac{\delta v}{v_0}(R, \theta, \varphi)$ is written as an expansion of spherical harmonics as shown in Eq. (5.3). The relative phaseshift in Eq. (5.15) is then given by

$$\begin{aligned}
\frac{\delta\varphi^{(i)}}{\varphi_0}(\Delta_{\text{off}}, v) &= \sum_{l=0}^{lmax} \sum_{m=-l}^{l} C_l^m \int_0^{\Delta_{\text{off}}} \int_0^{\pi} Y_l^m(\theta, \varphi) K(R, \theta, \varphi) d\theta d\varphi \\
&= \sum_{l=0}^{lmax} \sum_{m=-l}^{l} C_l^m K_{l,m}^{scat,ph}(\Delta_{\text{off}}, v).
\end{aligned} \quad (5.17)$$

The right-hand side of the relative phaseshift due to scattering in Eq. (5.17) has the same form as the ray theoretical phaseshift in Eq. (5.4), but with the scattering sensitivity kernel at frequency v for minor arcs given by

$$K_{l,m}^{scat,ph}(\Delta_{\text{off}}, v) = \int_0^{\Delta_{\text{off}}} \int_0^{\pi} Y_l^m(\theta, \varphi) K(R, \theta, \varphi) d\theta d\varphi. \quad (5.18)$$

In order to obtain group velocity maps using scattering theory, the frequency-averaged, timeshift $\delta t^{(i)}(\Delta_{\text{off}})$ in the frequency-range $v_0 - \Delta v$ and $v_0 + \Delta v$ is derived, hence

$$\begin{aligned}
\delta t^{(i)}(\Delta_{\text{off}}) &= \frac{1}{2\Delta v} \int_{v_0 - \Delta v}^{v_0 + \Delta v} \delta t^{(i)}(\Delta_{\text{off}}, v) dv \\
&= \sum_{l=0}^{lmax} \sum_{m=-l}^{l} U_l^m K_{l,m}^{scat,gr}(\Delta_{\text{off}}),
\end{aligned} \quad (5.19)$$

where we use that $\delta t^{(i)}(\Delta_{\text{off}}, v) = \delta\varphi^{(i)}(\Delta_{\text{off}}, v)/(2\pi v)$, and the coefficients of the spherical harmonics for relative group velocity are denoted by U_l^m. The minor arc, scattering theoretical sensitivity kernel for relative group velocity in Eq. (5.19) is given by

$$K_{l,m}^{scat,gr}(\Delta_{\text{off}}) = \frac{\Delta_{\text{off}}R}{2\Delta v} \int_{v_0 - \Delta v}^{v_0 + \Delta v} \frac{K_{l,m}^{scat}(\Delta_{\text{off}}, v)}{v_0(v)} dv. \quad (5.20)$$

In general, the reference velocity $v_0(v)$ depends upon the frequency in Eq. (5.20).

The relative phaseshift for major arcs is obtained using the scattering theory for minor arcs. This is because major arc scattering sensitivity kernels can be constructed from three scattering sensitivity kernels for minor arcs; one sensitivity kernel for the minor arc between the source $\mathbf{r}_S$ and the receiver anti-pod $\mathbf{r}_{RA}$, between the receiver anti-pod and the source anti-pod $\mathbf{r}_{SA}$ and between the source anti-pod and the receiver $\mathbf{r}_R$, respectively.

For major arcs, the scattering sensitivity kernel for relative phase velocity derived in the reference system is

$$
\begin{aligned}
K_{l,m}^{scat,ph}(\Delta_{\text{off}},\nu) \;=\; \frac{1}{\Delta_{\text{off}}} \Big(\;\; & (\Delta_{\text{off}}-\pi)K_{l,m}^{scat,ph,S\to RA}(\Delta_{\text{off}}-\pi,\nu) \\
& +(2\pi-\Delta_{\text{off}})K_{l,m}^{scat,ph,RA\to SA}(2\pi-\Delta_{\text{off}},\nu) \\
& +(\Delta_{\text{off}}-\pi)K_{l,m}^{scat,ph,SA\to R}(\Delta_{\text{off}}-\pi,\nu) \Big),
\end{aligned}
\tag{5.21}
$$

where $K_{l,m}^{scat,ph,S\to RA}(\Delta_{\text{off}}-\pi,\nu)$, $K_{l,m}^{scat,ph,RA\to SA}(2\pi-\Delta_{\text{off}},\nu)$ and $K_{l,m}^{scat,ph,SA\to R}(\Delta_{\text{off}}-\pi,\nu)$ are the relative phase velocity sensitivity kernels due to scattering for the minor arc between the source and receiver anti-pod, between the receiver anti-pod and the source anti-pod and between the source anti-pod and receiver, respectively. Similarly, the major arc sensitivity kernel for relative group velocity using scattering theory is given by

$$
\begin{aligned}
K_{l,m}^{scat,gr}(\Delta_{\text{off}}) \;=\; & K_{l,m}^{scat,gr,S\to RA}(\Delta_{\text{off}}-\pi) + K_{l,m}^{scat,gr,RA\to SA}(2\pi-\Delta_{\text{off}}) \\
& +K_{l,m}^{scat,gr,SA\to R}(\Delta_{\text{off}}-\pi).
\end{aligned}
\tag{5.22}
$$

The expansions in Eq. (5.21) and (5.22) are derived in appendix B.

Dziewonski (1984) and Dahlen and Tromp (1998) explain how to rotate the reference system so that the source-receiver configuration, originally aligned along the equator, can be anywhere on the sphere. In appendix C, the relative phaseshift related to relative phase velocity for any minor arc, as well as, major arc with the source position $\mathbf{r}_S$ and the receiver position $\mathbf{r}_R$ is derived. The sensitivity kernel in the observed coordinate system is given by

$$
K_{l,m}^{scat,ph}(\Delta_{\text{off}},\nu) = \exp(im\Phi) \sum_{n=-l}^{l} \exp(in\Psi) Q_l^{m,n}(\Theta) K_{l,n}^{scat,ph}(\Delta_{\text{off}},\nu),
\tag{5.23}
$$

where Φ, Ψ and Θ are the three Euler angles, $Q_l^{m,n}(\Theta)$ are the elements of the rotation matrix and the sensitivity kernel $K_{l,n}^{scat,ph}(\Delta_{\text{off}},\nu)$ is computed in the reference system where the source and receiver lie on the equator. This result also holds for group velocity measurements.

The regime of surface wave scattering theory is significant when the scale-length of heterogeneity is smaller than the width of the Fresnel zone (e.g. the conditions for ray theory are not satisfied). Let the characteristic length of inhomogeneity $a = 2\pi/l$ (in radians) for the angular degree l. By using the condition for scattering theory, we can derive the limits of classical ray theory expressed in the angular degree of the spherical harmonics. Hence, when

$$
\frac{L_F}{a} > 1 \Rightarrow l > \sqrt{\frac{8\pi^2}{3\lambda \tan\left(\frac{\Delta_{\text{off}}}{2}\right)}},
\tag{5.24}
$$

the regime of scattering theory is important.

5.2.4   The properties of the scattering sensitivity kernels

If the reference velocity is constant, the frequency integration in the sensitivity kernel due to scattering theory in Eq. (5.20) can be done analytically. The integration of the function $\sqrt{x}\sin(ax + \pi/4)$ is

$$\int \sqrt{x}\sin(ax + \frac{\pi}{4})dx = \frac{\sqrt{x}}{\sqrt{2}a}\left(\sin(ax) - \cos(ax)\right)$$
$$+ \frac{\sqrt{\frac{\pi}{4}}}{a^{3/2}}\left(C(\sqrt{\frac{2ax}{\pi}}) - S(\sqrt{\frac{2ax}{\pi}})\right), \qquad (5.25)$$

where the functions C and S are the Fresnel cosine integral and sine integral, respectively. See Abramowitz and Stegun (1970) for a description of the Fresnel cosine and sine integrals. This analytical result can be used to compute the scattering sensitivity kernels in Eq. (5.20) in an efficient and accurate manner. On the other hand if the reference velocity is dispersive, the frequency integration must be carried out numerically.

It is instructive to look at the sensitivity to the relative phase and group velocity fluctuations for a minor arc surface wave and a major arc surface wave as shown in Fig. 5.1A and 5.1B. The source position is located at latitude (0°, 0°), and the receiver position is at (0°, 70°), thus the epicentral distance for the minor arc is 70°, while for the major arc the source-receiver distance is 290°. The reference velocity $v_0 = 4779$ m/s which is the PREM phase velocity for Love waves at 150 s. The radius of the sphere is set to 6371 km. The sensitivity to the relative phase velocity in Fig. 5.1A is computed with Eq. (5.16). For group velocity measurements, the frequency-band is chosen proportional to the central frequency so that an optimal fit of waveforms is obtained simultaneously in the time and frequency domain. For example, surface waves at 40 s are bandpass-filtered between 20 s and 60 s while at 150 s the periodband is 150 s. Therefore, the sensitivity kernel using scattering theory for relative group velocity in Fig. 5.1B is frequency integrated between 75 s and 225 s for Love waves at the central period equal to 150 s. The sensitivity kernel for relative group velocity measurements in Fig. 5.1B is obtained by using Eq. (5.16) multiplied by $\Delta_{\text{off}}R/v_0(\nu)$ and then averaging over the frequency-band $\nu_0 - \Delta\nu$ and $\nu_0 + \Delta\nu$ where the frequency-dependent PREM reference velocity is taken into account. The black zones in the nearfield at the source, source anti-pod, receiver anti-pod and receiver show the singularities in the geometrical factors of the scattering sensitivity kernels for minor arcs and major arcs. The sensitivity to the relative phase and group velocity resembles those of the form of Fresnel zones for point sources. The sensitivity kernel for relative phase velocity clearly shows the first Fresnel zone, as well as, higher order Fresnel zones. Notice that the sidelobes corresponding to higher order Fresnel zones do not vanish if we take the frequency averaging, inherent to the measurement, into account. In order to obtain the phase velocity measurements from Trampert and Woodhouse (2001), the width of the bandpass-filter is 5 mHz. The form of the scattering sensitivity kernels for phase velocity measurements is also shown by Woodhouse and Girnuis (1982) and Snieder (1993) who apply normal mode theory to compute the sensitivity to slowness perturbations due to scattering theory in surface wave tomography.
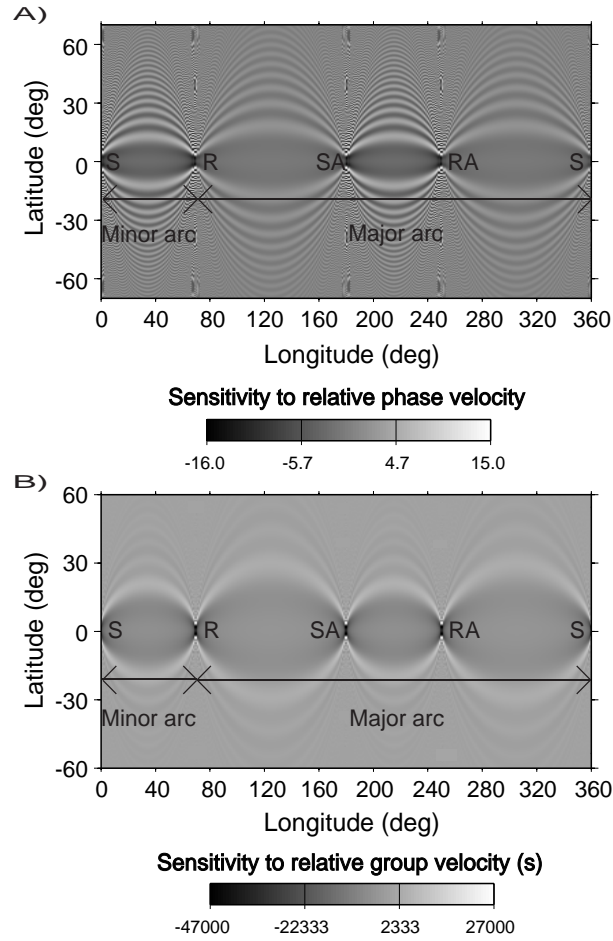
Figure 5.1: *The scattering sensitivity kernel for relative phase and group velocity perturbations computed point by point on the sphere. The epicentral distance is 70° for the minor arc and 290° for the major arc. The source position is denoted by S, the receiver anti-pode position is RA, the source anti-pode position is SA and the receiver position is R. The sensitivity kernel due to scattering theory for the major arc surface wave is constructed by three scattering sensitivity kernels for minor arc surface waves. A) The sensitivity kernel for relative phase velocity perturbations is calculated for Love waves with the single period at 150 s. The sensitivity kernel has sidelobes so that the first Fresnel zone and higher order Fresnel zones are visible. B) The sensitivity kernel for relative group velocity fluctuations is computed between 75 s and 225 s taking the frequency-dependence of the PREM phase velocity for Love waves into account. The sidelobes of the sensitivity kernel at different frequencies interfer destructively. The relative phaseshift is therefore only sensitive to relative group velocity inside the Fresnel zone.*

Notice that the sensitivity kernels in Woodhouse and Girnuis (1982) and Snieder (1993) have oscillations along the great circle as a result of the interference of different surface wave orbits. The scattering sensitivity kernel for relative group velocity in Fig. 5.1B only shows the first Fresnel zone. This is because of the frequency integration that causes destructive interference of sidelobes at higher order Fresnel zones. According to ray theory, the sensitivity kernel is only non-zero on the great circle passing through the source and receiver at 0° latitude.

In Fig. 5.2, the cross sections of the scattering sensitivity kernels in Fig. 5.1A and 5.1B are plotted for different periods and epicentral offsets. The sensitivity kernels for relative phase and group velocity are calculated at the half epicentral offset where the width of the Fresnel zone is maximum. In Fig. 5.2A, the sensitivity kernels for relative phase velocity are estimated for the period at 40 s (solid line), 100 s (dotted line) and 150 s (dashed line) using the PREM model for the reference velocity, and the epicentral distance is set to 160°. In Fig. 5.2B, the sensitivity kernels for relative group velocity are computed with numerical frequency integration taking account of the PREM model for the central periods at 40 s (solid line), 100 s (dotted line) and 150 s (dashed line) with the periodbands set equal to the central period. The source-receiver distance is fixed to 160° for the curves in Fig. 5.2B. Notice that computing the scattering sensitivity kernel using the complete PREM model in the range of frequency integration yields nearly the same result as using the PREM phase velocity at central period as constant reference velocity in the frequency-range. We do not show any scattering sensitivity kernels for group velocity measurements calculated with a constant reference velocity over the frequency range of integration because they are almost indistinguishable from the scattering sensitivity kernels for group velocity measurements taking the PREM phase velocity into account. The sensitivity kernels in Fig. 5.2C and 5.2D are computed with the period fixed to 150 s, and the epicentral distance is 60° (solid line), 110° (dotted line) and 160° (dashed line). For Fig. 5.2D, the periodband of the frequency integration is equal to the central period. In brief, Fig. 5.2 shows that the width of the central lobe of the scattering sensitivity kernel increases for increasing period and source-receiver distance. In terms of ray theory, the sensitivity to relative phase and group velocity perturbations is only non-zero at 0° latitude for the given source-receiver configuration in Fig. 5.2.

Ray theory and scattering theory predict the same relative phaseshift when the lengthscale of heterogeneity is larger than the width of the Fresnel zone (i.e the condition for the regime of ray theory) since it follows from expression (5.16) that

$$\int_0^{\Delta_{\text{off}}} \int_0^{\pi} K(R, \theta, \varphi) \frac{\delta v}{v_0}(R, \theta, \varphi) d\theta d\varphi = -\frac{1}{\Delta_{\text{off}}} \int_0^{\Delta_{\text{off}}} \frac{\delta v}{v_0}(\theta, \varphi) dr, \qquad (5.26)$$

when the characteristic length of the relative phase velocity is larger than the width of the Fresnel zone.

The maximum width W of the central lobe of the scattering sensitivity kernel is com-
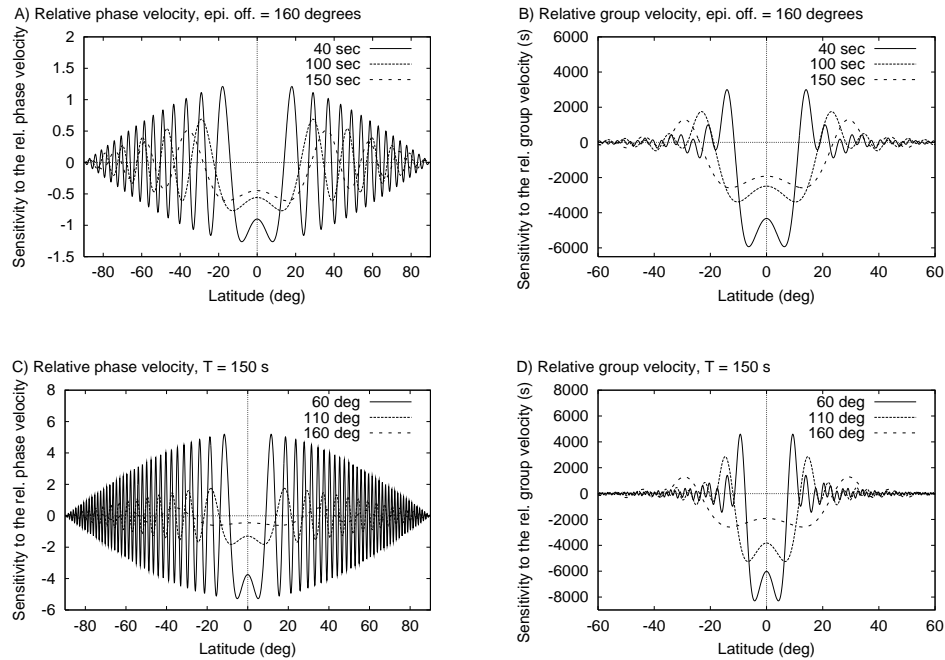
Figure 5.2: *Cross sections of the scattering sensitivity kernels for relative phase and group velocity perturbations computed at the half epicental distance. A) The epicentral distance is 160° for the three curves. The cross section of the sensitivity kernel for relative phase velocity fluctuations is computed at 40 s (solid line), 100 s (dotted line) and 150 s (dashed line). B) The epicentral distance is 160° for the curves. The cross section of the sensitivity kernel for relative group velocity perturbations is computed in the periodband with the central period $T_0 = 40$ s and the half periodband $\Delta T = 20$ s (solid line), $T_0 = 100$ s and $\Delta T = 50$ s (dotted line) and $T_0 = 150$ s and $\Delta T = 75$ s (dashed line). C) Sensitivity kernels at 150 s for relative phase velocity fluctuations. The epicentral distance for the cross section of the scattering sensitivity kernel is 60° (solid line), 110° (dotted line) and 160° (dashed line). D) The cross section of three sensitivity kernels for relative group velocity fluctuations with the epicentral distance at 60° (solid line), 110° (dotted line) and 160° (dashed line). The sensitivity kernels for relative group velocity fluctuations are integrated between 75 s and 225 s including the frequency-dependence of the PREM phase velocity.*

puted by setting the sine function in Eq. (5.16) equal to zero, hence

$$
\begin{aligned}
0 &= \sin\left(\frac{\pi v R}{v_0}(\theta - \frac{\pi}{2})^2 \frac{\sin(\Delta_{\text{off}})}{\sin(\varphi)\sin(\Delta_{\text{off}} - \varphi)} + \frac{\pi}{4}\right) \Rightarrow \\
\left(\theta - \frac{\pi}{2}\right)^2 &= \frac{3\lambda}{4} \frac{\sin(\varphi)\sin(\Delta_{\text{off}} - \varphi)}{\sin(\Delta_{\text{off}})},
\end{aligned}
\tag{5.27}
$$

where $\lambda = v_0/(vR)$ is the central wavelength in radians. The maximum width $W = 2|\theta - \pi/2|$ of the central lobe is obtained by setting $\varphi = \Delta_{\text{off}}/2$ in Eq. (5.27) which gives that

$$
W = \sqrt{\frac{3\lambda}{2} \tan\left(\frac{\Delta_{\text{off}}}{2}\right)}.
\tag{5.28}
$$

By comparing the maximum width of the central lobe in Eq. (5.28) with the width L_F of Fresnel zones on the sphere in Eq. (5.38), the number n that defines the width of the Fresnel zone is given by

$$
n = \frac{8}{3}.
\tag{5.29}
$$

This result is also derived in Spetzler and Snieder (2001) in a 2-D, Cartesian coordinate system. Additionally, we identify the central lobe of the scattering sensitivity kernel as the Fresnel zone on the sphere.

According to Eq. (5.24), scattering theory is significant when the width of the Fresnel zone is larger than the length-scale of heterogeneity. We see in Fig. 5.2 that the Fresnel zone of surface waves enlarges for increasing period and epicentral offset. Therefore given the same strength of heterogeneity, scattering theory is most important for the longest period surface waves and if there are many long epicentral offsets in a given surface wave data set.

5.3   Setup of the surface wave experiment

The dataset of observed relative phaseshifts is from Trampert and Woodhouse (2001), who calculate global phase velocity maps of Love and Rayleigh waves for periods between 40 s and 150 s using the great circle approximation. The source and receiver positions corresponding to the measured phaseshifts are corrected for the ellipticity of the Earth. We use the observed relative phaseshifts to compute new phase velocity maps at 40 s and at 150 s, but using the scattering theory for fundamental-mode Love waves.

The maximum degree of the spherical expansion of the phase velocity maps is 40, thus the number of unknown model parameters to be inverted is 1681. In addition, we use the same inversion procedure as Trampert and Woodhouse (1995); an a priori Laplacian smoothness condition is implemented so that truncation problems are avoided. In this manner, using the same data set and inversion method as Trampert and Woodhouse (2001), it is possible to make a direct comparison between global phase velocity maps between periods at 40 s and 150 s inferred from ray theory and scattering theory, respectively. In Table 5.1, the a priori reference PREM velocity for Love waves at 40 s and 150 s and the number of observed relative phaseshifts are given.

	Love waves
PREM velocity at 40 s (m/s)	4440
PREM velocity at 150 s (m/s)	4779
Number of obs. rel. phaseshifts	41016

Table 5.1: *The PREM reference velocity at 40 s and 150 s and the number of observed relative phaseshift measurements for Love waves.*

5.4   Results

In this section, we present the phase velocity maps that are obtained with ray theory and scattering theory using Love wave phase measurements between periods of 40 s and 150 s. We do not show any results retrieved from Rayleigh waves which lead to the same conclusions that we draw from the Love wave phase velocity maps. We hardly find any discrepancy between the phase velocity maps for Love waves at either 40 s and 150 s obtained from ray theory and scattering theory. The difference between the phase velocity maps compiled with scattering theory and the ones computed using ray theory are shown in Fig. 5.3A and 5.3B for the global Love wave experiment at 40 s and 150 s, respectively.

The powerspectra of the phase velocity maps in Fig. 5.4 confirm the qualitative observation that ray theory and scattering theory produce the same models. For Love waves at 40 s, the Laplacian smoothness factor $\gamma = 1 \times 10^{-4}$, while for the surface wave study at 150 s, $\gamma = 1 \times 10^{-2}$. Phase measurements for Love waves at 150 s are quite noisy which cause unrealistic small-scale structure in the phase velocity maps using too small a value for the smoothness factor. As a result of the values of the Laplacian smoothness parameter, small-scale structures for angular degrees higher than 20-25 and 10-15 (e.g. heterogeneity with a characteristic length of 1600-2000 km and 2700-4000 km, respectively) are strongly suppressed in the phase velocity maps for Love waves at 40 s and 150 s, respectively. On the other hand, the Fresnel zone for Love waves at 40 s and at 150 s with the characteristic epicentral distance equal to 100° has a maximum width of about 1400 km (angular degree ≈ 28) and 2800 km (angular degree ≈ 14), respectively. Hence according to the condition for the regime of ray theory in Eq. (5.8), it is approximately correct to apply ray theory for the obtained phase velocity maps (not shown in the paper).

The smoothness parameters for the scattering theoretical inversion of Love waves at 40 s and 150 s are determined in the following way; the derivation matrix $\mathbf{G}$ (see Menke, 1989) built from the kernels $k_{l,m}$ is not necessarily the same for ray theory and scattering theory. Thus, the two theories will in general not resolve models identically for a given smoothness parameter. We require for Love waves at a given period that the trace of the resolution matrix for ray theory closely resembles to that for scattering theory. Then we can compare models built for the same number of parameters.

A) Difference (scat-ray): Love 40 sec

Rel. phase velocity perturbations (%)

B) Difference (scat-ray): Love 150 sec

Rel. phase velocity perturbations (%)

Figure 5.3: *The difference between the phase velocity maps obtained using scattering theory and ray theory for Love wave at 40 s and 150 s. The difference in relative phase velocity are given in percent on a scale between $\pm$ 2 %. Plate boundaries and hotspots are drawn with white lines and circles, respectively. The coastlines are marked with black l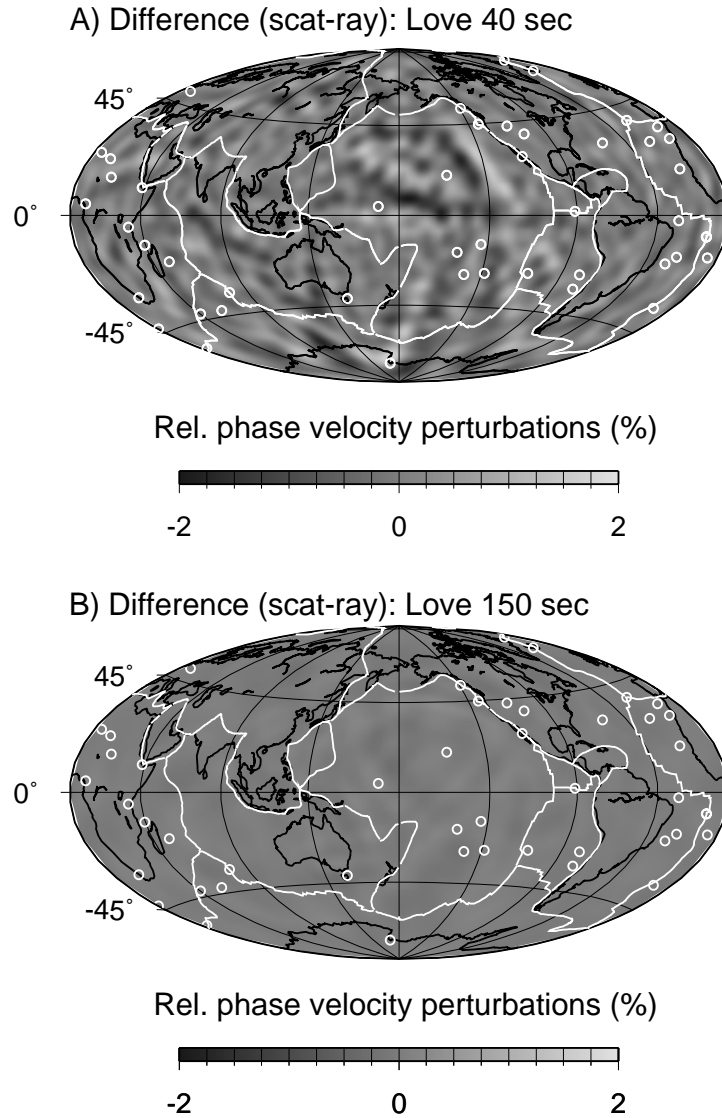ines on the difference between the phase velocity maps compiled using scattering theory and ray theory. A) Love wave at 40 s. The smoothness factor $\gamma = 1 \times 10^{-4}$. B) Love waves at 150 s. The smoothness factor $\gamma = 1 \times 10^{-2}$.*
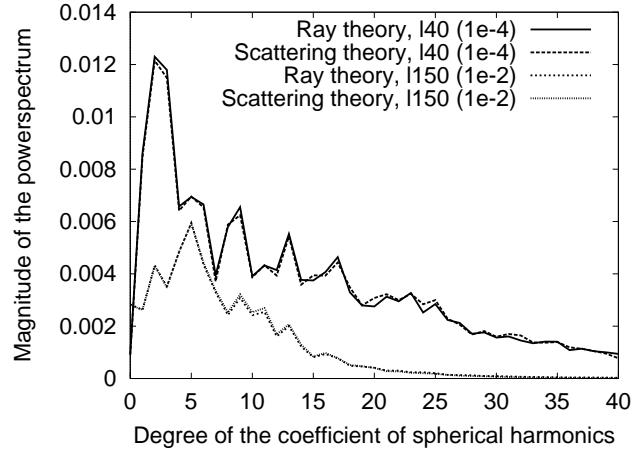
Figure 5.4: *The power spectra of the estimated phase velocity maps for Love waves at 40 s and 150 s using ray theory and scattering theory. The degree of the coefficients of spherical harmonics is shown on the abscissa, while the magnitude of the powerspectra is plotted on the ordinate. It is observed that the phase velocity models for Love waves at 40 s and 150 s have the same large-scale structure when using scattering theory and ray theory. However, it is not possible to obtain reliable smaller scale structures in the obtained phase velocity maps because the observed relative phaseshifts requires a rather large Laplacian smoothness factor for Love waves at 150 s. The smoothness factors applied in the inversion of phase velocity measurements for Love waves at 40 s and 150 s are the numbers in the brackets.*

5.5 Discussion

In the inversion of phaseshift data for Love waves between periods at 40 s and 150 s, ray theory and scattering theory compile the same large-scale structure as shown in Fig. 5.3. Because of the large value of the smoothness parameter, it is not possible to comment on the presence of smaller scaled structures of the Earth. In order to examine the discrepancy between ray theory and scattering theory in surface wave tomography, synthetic tests should be carried out using an input-model with heterogeneity which is much smaller in size than the width of the Fresnel zone.

Spetzler and Snieder (2001) and Spetzler *et al*. (2001) show that scattering theory is very accurate in the prediction of timeshifts obtained from a finite-difference solution of the acoustic wave equation and from a laboratory ultrasonic wave experiment, respectively, wherein the length-scale of heterogeneity is smaller than the width of the Fresnel zone. We believe that the same holds for surface wave tomography.

In Fig. 5.5, we show with a synthetic surface wave experiment that the discrepancy between ray theory and diffraction theory in global surface wave tomography is important for heterogeneity with the angular degree larger than $l = 30$ and $l = 20$ for Love

waves at 40 s and 150 s, respectively. Using the results from Spetzler and Snieder (2001) and Spetzler *et al*. (2001), we assume that surface wave scattering theory for phase and group velocity measurements is correct to use in models with any scale-length of velocity anomalies. We calculate in Fig. 5.5 the relative error in percent introduced by ray theory using the source and receiver positions in the dataset for Love waves, hence

$$\text{relative error} = \frac{100 \text{ \%}}{N} \sum_{i=1}^{N} \left| \frac{d_i^{ray} - d_i^{scat}}{d_i^{scat}} \right|, \tag{5.30}$$

where N is the number of source-receiver geometries and d_i^{ray} and d_i^{scat} are the surface wave data due to ray theory and scattering theory, respectively. To avoid numerical instability, source-receiver pairs with $|d_i^{scat}| \leq 1 \times 10^{-3}$ for phase velocity measurements and $|d_i^{scat}| \leq 1$ s for group velocity measurements have not been included in Eq. (5.30). The velocity perturbation is set to 10 % and the angular order m is fixed to zero, while the angular degree goes from 1 to 40 corresponding to the size of velocity heterogeneity between 40000 km and 1000 km in the synthetic experiment. The ray theoretical approach based on the great circle approximation and the first order scattering theory are both linear theories, so the amplitude of the velocity perturbation does not influence the relative error in Eq. (5.30). Thus, for realistic Earth models with either a white or a red spectrum, the synthetic experiment presented in this paper indicates to which extent the ray theoretical great circle approximation differs from a more exact scattering theory. In Fig. 5.5A, the relative error due to ray theory in surface wave tomography for phase velocity measurements is calculated using the sensitivity kernel for ray theory in Eq. (5.5) and the sensitivity kernel due to diffraction theory in Eq. (5.18). In Fig. 5.5B, we show the relative error introduced by ray theory in tomographic surface wave experiments with group velocity measurements for which we have applied Eq. (5.7) for the ray theoretical sensitivity kernel and Eq. (5.20) for the scattering theoretical sensitivity kernel. The relative error due to the great circle approximation should not exceed the observational relative error in the data. The phase velocity measurements from Trampert and Woodhouse (2001) have a relative error of about 20 % for Love waves at 40 s and a relative error of 40 % for Love waves at 150 s. Using the results in Fig. 5.5, we see that ray theoretical surface wave tomography is limited to angular degrees smaller than $l = 30$ and $l = 20$ for Love waves at 40 s and 150 s, respectively. However, if we proceed to slightly higher angular degrees we must certainly take the non-ray geometrical effect of surface waves into account. Otherwise, we may obtain inaccurate surface wave Earth models because of the inappropriate use of ray theory.

In Fig. 5.6A to 5.6F, we present plots of the scattering theoretical phaseshift versus the ray theoretical phaseshift for Love waves at 150 s. Fig. 5.6 is similar to the plots that are found in Baig *et al*. (2000). The source-receiver positions in the surface wave dataset from Trampert and Woodhouse (2001) are applied. Spherical harmonics input models with the length-scale of inhomogeneity related to the angular degree l are used in Fig. 5.6A ($l = 1$), 5.6B ($l = 5$), 5.6C ($l = 15$), 5.6D ($l = 20$), 5.6E ($l = 30$) and 5.6F ($l = 40$). We have chosen to plot the normalised phaseshifts calculated with scattering theory and ray theory. The solid lines indicate the error in the Love waves dataset at 150 s. We see

A) Phase velocity measurements

B) Group velocity measurements
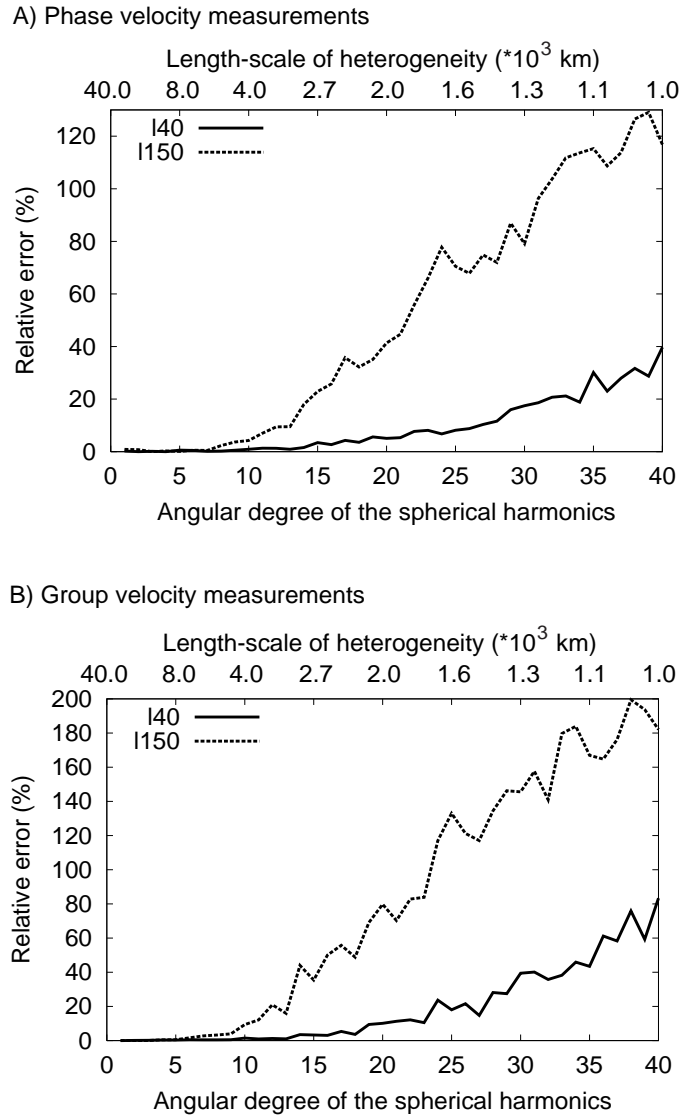
Figure 5.5: *The synthetic experiment showing that the relative error introduced by ray theory increases for decreasing characteristic length of velocity anomalies in a global surface wave experiment with Love waves between 40 s and 150 s. The length-scale of heterogeneity is expressed in angular degree ranging between 1 and 40. The relative error between surface wave data due to ray theory and scattering is calculated using the source-receiver positions in the Love wave dataset. A) The synthetic experiment for phase velocity measurements. B) The synthetic experiment for group velocity measurements.*
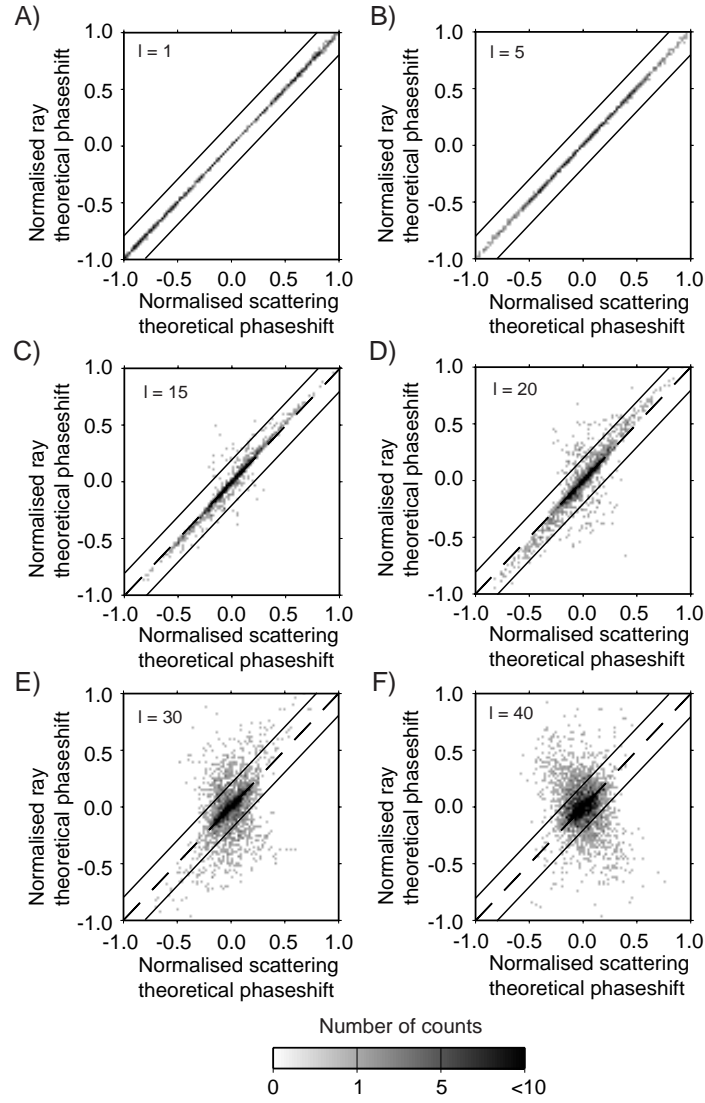
Figure 5.6: *Plots of the scattering theoretical phaseshift versus the ray theoretical phaseshift for spherical harmonic models with the characteristic length of heterogeneity expressed written as angular degree l. The case of Love waves at 150 s is considered, and the source-receiver positions for the computation of the phaseshifts due to ray theory and scattering theory come from Trampert and Woodhouse (2001). The two solid lines indicate the error in the surface wave dataset for Love waves at 150 s. A) l = 1, B) l = 5, B) l = 15, B) l = 20, B) l = 30, B) l = 40.*

in Fig. 5.6A and 5.6B that there is a one-to-one correspondence between the scattering theoretical phaseshifts and the ray theoretical phaseshifts. In Fig. 5.6C ($l = 15$) and 5.7D ($l = 20$) where the angular degree of inhomogeneity is at the limit of the regime of the great circle approximation for Love waves at 150 s, it is noticed that several points of d^{scat} versus d^{ray} are outside the observed relative error in the dataset. It is as well seen in Fig. 5.6C and 5.6D that the points in the plot are slightly rotated anti-clockwise compared to the dashed line with slope one through origo. There is therefore a tendency for a bias towards smaller values of the scattering theoretical relative phaseshifts compared to the ray theoretical ones (see Spetzler and Snieder, 2001; Spetzler *et al.*, 2001 for other examples of this trend). However in Fig. 5.6E and 5.6F, the picture is a bit different than in the previous plots of Fig. 5.6. The points of d^{scat} versus d^{ray} are spread more homogeneously around in the plots, but there is still a tendency of an anti-clockwise rotation of the best-fitting line (not shown) through the points (d^{scat}, d^{ray}). In Fig. 5.6F, the best-fitting line of the points (d^{scat}, d^{ray}) is rather that positive scattering theoretical phaseshift correspond to negative ray theoretical phaseshift and vice versa. It means that using Love waves at 150 s to estimate small-scale structures ($l = 40$ in Fig. 5.6F) the application of the ray theoretical great circle approximation produces global maps with the wrong sign of the estimated velocity field.

In terms of wavefront healing, Nolet and Dahlen (2000) discuss scattering theory in surface wave tomography. They explain using the Gaussian beam solution to the parabolic approximation of the scalar Helmholtz equation that an inversion of phase velocity measurements is better behaved than the one using group velocity measurements. Their argument is that surface wave group velocity delays have large sidelopes compared to surface wave phase delays when the diameter of heterogeneity is of the same order of magnitude as the wavelength. The large sidelopes of the surface wave group velocity delay may therefore introduce considerable noise into the data according to Nolet and Dahlen (2000). Based on the sensitivity kernels for phase and group velocity in this paper, we rather find that the inversions of phase and group velocity measurements are both equally behaved. It is not difficult to compute the forward problem either applying the sensitivity kernel for relative phase or group velocity. The developed scattering approach for surface waves is just as easy to use as the ray theoretical great circle approximation. On a 250 MHz ultra-sparc machine, it takes 1 day, 5 days and 15 days cpu-time to compute the tabulated scattering sensitivity kernels for the analytical frequency-integration for relative group velocity, for single-frequency relative phase velocity and for the numerically frequency-integrated PREM model for relative group velocity, respectively, and to carry out the inversion of 42000 surface wave phaseshifts for a phase or group velocity map to angular degree and order 40.

5.6 Conclusions

We have investigated the non-ray geometrical effect in global surface wave tomography. The first-order Rytov approximation was used to derive a linear relationship between surface wave phase and group velocity measurements and relative phase and group velocity

perturbations, respectively. The diffraction theoretical approach takes the finite-frequency effect of surface waves into account which is not possible with conventional ray theory in surface wave tomography. For finite-frequency surface waves, the sensitivity to relative phase and group velocity is maximum in magnitude off-path the ray trace. In addition, the scattering sensitivity kernel for relative phase velocity has sidelobes outside the Fresnel zone, while the sensitivity kernel for relative group velocity is only dominant over the Fresnel zone. In contrast to this, ray theory predicts that the sensitivity to relative velocity perturbations is only non-zero on the great circle path connecting the source and receiver. Given the same strength of heterogeneity, scattering of surface waves becomes increasingly important for increasing period and epicentral distance.

We applied phaseshift measurements for Love waves between periods at 40 s and 150 s from Trampert and Woodhouse (2001) to compile global phase velocity maps to angular degree and order 40 using scattering theory. These models for diffraction theory were matched with those computed with ray theory. We applied an a priori Laplacian smoothness condition in the inversion procedure resulting that only structures to angular degree 20-25 for Love waves at 40 s and to angular degree 10-15 for Love waves at 150 s are present in the phase velocity maps which is close to the limit of resolution in current global surface wave tomography. We saw that ray theory and scattering theory produce the same tomographic models in that regime for which the conditions for ray theory are satisfied.

We showed with a synthetic experiment where the relative error between surface wave data using ray theory and scattering theory was computed for velocity inhomogeneity with increasing angular degree that the scattering of surface waves is dominant at angular degrees larger than $l = 20$ and $l = 30$ for surface wave at 150 s and 40 s, respectively. The regime of surface wave scattering theory corresponds to the limits of present-day resolution in surface wave tomography. Consequently, in order to obtain detailed higher degree surface wave models using long-period surface waves or dataset with many long source-receiver distances we must take the finite-period effect of surface waves into account.

In the USArray project, the United States will be covered with a dense array of 2000 seismographs having an uniform station spacing during the next ten years (see Levander *et al*., 1999). The purpose of the USArray is to increase the resolution of tomographic images of the North American shield. However, it is not enough to increase the data coverage of the area of interest, but it is as well important to improve the tomographic imaging methodology that is to be applied in inversions of data from the USArray project.

References

Abramowitz M. and Stegun I. A. (**1970**). *Handbook of mathematical functions (with formulas, graphs and mathematical tables)* (Dover Publications, Inc.).

Backus G. E. (**1964**). Geographical interpretation of measurements of average phase velocities of surface waves over great circular and great semi circular paths, Bull. seism. Soc. Am. **54**, 571-610.

Baig A., Dahlen F. A. and Hung S. H. (**2000**). The efficacy of Born kernels for computation of traveltimes in random media, Abstract at AGU 2000 Fall Meeting. **S62A-01**.

Dahlen F. A. (**1979**). The spectra of unresolved split normal mode multiplets, Geophys. J. R. astr. Soc. **58**, 1-33.

Dahlen F. A. and Tromp J. (**1998**). *Theoretical global seismology* (Princeton University Press, Princeton, New Jersey.).

Dahlen A., Hung S. H. and Nolet G. (**2000**). Fréchet kernels for finite-frequency travel times-I. theory, Geophys. J. Int. **141**, 157-174.

Dziewonski A. M. (**1984**). Mapping the lower mantle: determination of lateral heterogeneity in *P*-velocity up to degree and order 6, J. Geophys. Res. **89**, 5929-5952.

van Heijst H. J. and Woodhouse J. (**1999**). Global high-resolution phase velocity distributions of overtone and fundamental-mode surface waves determined by mode branch stripping, Geophys. J. Int. **137**, 601-620.

Hung S. H., Dahlen A. and Nolet G. (**2000**). Fréchet kernels for finite-frequency travel times-II. examples, Geophys. J. Int. **141**, 175-203.

Jordan T. H. (**1978**). A procedure for estimating lateral variations from low frequency eigenspectra data, Geophys. J. R. astr. Soc. **52**, 441-455.

Kravtsov Y. A. (**1988**). 'Rays and caustics as physical objects' in *Prog. in Optics*, XXVI, Edited by Wolf E. (Elsevier, Amsterdam), 227-348.

van der Lee S. and Nolet G. (**1997**). Upper mantle *S*-velocity structure of North America, J. Geophys. Res. **102**, 22815-22838.

Levander A., Humphreys E. G., Ekstrom G., Meltzer A. S. & Shearer P. M. (**1999**). Proposed project would give unprecedented look under North America, EOS **80, No. 22**, 245 and 250-251.

Marquering H., Nolet G. and Dahlen F. A. (**1998**). Three-dimensional waveform sensitivity kernels, Geophys. J. Int. **132**, 521-534.

Marquering H., Dahlen F. A. and Nolet G. (**1999**). The body-wave traveltime paradox: bananas, doughnuts and 3-D delay-time kernels, Geophys. J. Int. **137**, 805-815.

Menke W. (**1989**). *Geophysical data analysis: discrete inverse theory* (Academic Press, Inc.).

Menke W. and Abbot D. (**1990**). *Geophysical theory* (Columbia University Press, NY.).

Nolet G. and Dahlen F. A. (**2000**). Wavefront healing and the evolution of seismic delay times, J. Geophys. Res. (**105**), 19043-19054.

Passier M. L and Snieder R. (**1995**). Using differential waveform data to retrieve local S-velocity structure or path-averaged S-velocity gradients, J. Geophys. Res. **100**, 24061-24078.

Ritzwoller M. H. and Levshin A. L. (**1998**). Eurasian surface wave tomography: group velocities, J. Geophys. Res. **103**, 4839-4878.

Snieder R. (**1986**). The influence of topography on the propagation and scattering of surface waves, Phys. Earth. Plan. Int., **44**, 226-241.

Snieder R. and Nolet G. (**1987**). Linearized scattering of surface waves on a spherical Earth, J. Geophys. **61**, 55-63.

Snieder R. and Romanowicz B. (**1988**). A new formalism for the lateral heterogeneity on normal modes and surface waves -I: isotropic perturbations, perturbations of interfaces and gravitational perturbations, Geophys. J. R. Astron. Soc. **92**, 207-222.

Snieder R. (**1993**). Global inversions using normal mode and long-period surface waves, in *Seismic tomography: theory and practice*, 23-63, (Chapman and Hall, London, UK.).

Snieder R. and Lomax A. (**1996**). Wavefield smoothing and the effect of rough velocity perturbations on arrival times and amplitudes, Geophys. J. Int. **125**, 796-812.

Spetzler J. and Snieder R. (**2001**). The effects of small-scale heterogeneity on the arrival time of waves, Geophys. J. Int. (**145**), In press.

Spetzler J., Sivaji C., Nishizawa O. and Fukushima Y. (**2001**). A test of ray theory and scattering theory based on a laboratory experiment using ultrasonic waves and numerical simulations by finite-difference method, Geophys. J. Int. (**Submitted**).

Tong J., Dahlen F. A., Nolet G. and Marquering H. (**1998**). Diffraction effects upon finite-frequency traveltimes: a simple 2-D example, Geophys. Res. Lett. **25**, 1983-1986.

Trampert J. and Woodhouse J. H. (**1995**). Global phase velocity maps of Love and Rayleigh waves between 40 and 150 seconds, Geophys. J. Int. **122**, 675-690.

Trampert J. and Woodhouse J. H. (**2001**). Assessment of global phase velocity models, Geophys. J. Int. (**144**), 165-174.

Yomogida K. and Aki K. (**1987**). Amplitude and phase data inversion for phase velocity anomalies in the Pacific ocean basin, Geophys. J. R. astr. Soc. **88**, 161-204.

Yomogida K. (**1992**). Fresnel zone inversion for lateral heterogeneities in the Earth, Pure Appl. Geophys., **138** (3), 391-406.

Woodhouse J. H and Dziewonski A. M. (**1984**). Mapping the upper mantle: three-dimensional modeling of Earth structure by inversion of seismic wavefroms, J. Geophys. Res. **89**, 5953-5986.

Woodhouse J. H. and Girnuis T. P. (**1982**). Surface waves and free oscillations in a regional Earth model, Geophys. J. R. astr. Soc, **68**, 653-673.

Woodward M. J. (**1992**). Wave-equation tomography, Geophys., **57**, 15-26.

Zhao L., Jordan T. H. and Chapman C. H. (**2000**). Three-dimensional Fréchet differential kernels for seismic delay times, Geophys. J. Int. **141**, 558-576.

5.7   Appendix A: Perturbation theory of the propagation length of scattered ray paths, the width of the Fresnel zone and the geometrical factor

According to Fig. 5.7 the epicentral distance between the source and receiver is denoted by Δ_{off}, and the epicentral distance between the source and scatterer point and the scatterer point and receiver are marked as Δ_1 and Δ_2, respectively. The perpendicular distance from the source-receiver geometry to the scatterer at the offset φ is $|\theta - \pi/2|$. Using the law of cosines on a sphere to relate Δ_1 with $|\theta - \pi/2|$ and φ, we obtain

$$
\begin{aligned}
\cos(\Delta_1) &= \cos(|\theta - \frac{\pi}{2}|)\cos(\varphi) + \sin(|\theta - \frac{\pi}{2}|)\sin(\varphi)\cos(\frac{\pi}{2}) \\
&= \cos(|\theta - \frac{\pi}{2}|)\cos(\varphi).
\end{aligned} \tag{5.31}
$$

Isolating Δ_1 from Eq. (5.31) and assuming that the ray deflection $|\theta - \pi/2|$ is small gives

$$
\begin{aligned}
\Delta_1 &= \arccos\left(\cos(|\theta - \frac{\pi}{2}|)\cos(\varphi)\right) \\
&\approx \arccos\left(\cos(\varphi) - \frac{1}{2}(\theta - \frac{\pi}{2})^2\cos(\varphi)\right) \\
&\approx \varphi + \frac{(\theta - \frac{\pi}{2})^2}{2\tan(\varphi)}.
\end{aligned} \tag{5.32}
$$

Similarly, we have for Δ_2 that

$$
\Delta_2 = (\Delta_{\text{off}} - \varphi) + \frac{(\theta - \frac{\pi}{2})^2}{2\tan(\Delta_{\text{off}} - \varphi)}. \tag{5.33}
$$
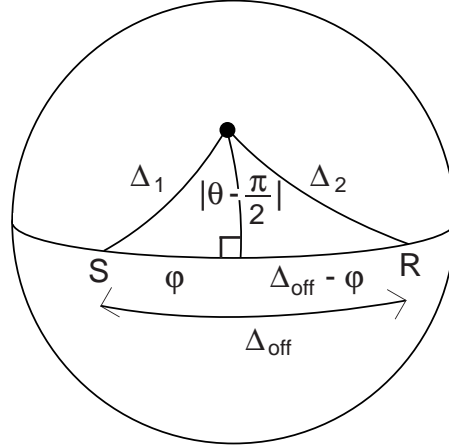
Figure 5.7: *Explanation of the variables applied in the derivation of the propagation
length of a scattered ray path, the width of the Fresnel zone on the sphere and the geo-
metrical factor using second order perturbation theory.*

The detour (i.e. $\Delta_1 + \Delta_2 - \Delta_{\text{off}}$) is then given by

$$
\begin{aligned}
\Delta_1 + \Delta_2 - \Delta_{\text{off}} &= \frac{(\theta - \frac{\pi}{2})^2}{2}\left(\frac{1}{\tan(\varphi)} + \frac{1}{\tan(\Delta_{\text{off}} - \varphi)}\right) \\
&= \frac{(\theta - \frac{\pi}{2})^2}{2}\frac{\sin(\Delta_{\text{off}})}{\sin(\varphi)\sin(\Delta_{\text{off}} - \varphi)}.
\end{aligned}
\tag{5.34}
$$

The condition for Fresnel zones on a sphere that the detour is less than the wavelength
divided by a number n is given by

$$
\Delta_1 + \Delta_2 - \Delta_{\text{off}} \leq \frac{\lambda}{n},
\tag{5.35}
$$

where λ is the wavelength measured in radians. The sign of equality in Eq. (5.35) is
used to calculate the Fresnel zone boundary. By inserting the detour in Eq. (5.34) in the
Fresnel zone condition in Eq. (5.35), the half width $(\theta - \frac{\pi}{2})$ of Fresnel zones is derived,
hence

$$
(\theta - \frac{\pi}{2}) = \sqrt{\frac{2\lambda\sin(\varphi)\sin(\Delta_{\text{off}} - \varphi)}{n\sin(\Delta_{\text{off}})}},
\tag{5.36}
$$

which has the largest value for $\varphi = \Delta_{\text{off}}/2$. For that case, the half width of the Fresnel
zone is given by

$$
(\theta - \frac{\pi}{2}) = \sqrt{\frac{\lambda}{n}\tan(\frac{\Delta_{\text{off}}}{2})}.
\tag{5.37}
$$

The maximum width L_F of Fresnel zones on the sphere is twice the half width $(\theta - \frac{\pi}{2})$ in Eq. (5.37), thus

$$L_F = \sqrt{\frac{4\lambda}{n} \tan(\frac{\Delta_{\text{off}}}{2})},\tag{5.38}$$

where L_F and λ are measured in radians.

The geometrical factors $\sin(\Delta_1)$ and $\sin(\Delta_2)$ are derived to zeroth order approximation using Eq. (5.32) and Eq. (5.33), thus

$$\sin(\Delta_1) = \sin(\varphi) \qquad \text{and} \qquad \sin(\Delta_2) = \sin(\Delta_{\text{off}} - \varphi),\tag{5.39}$$

where it is assumed that $(\theta - \pi/2)^2/(2\tan(\varphi)) \ll 1$ and $(\theta - \pi/2)^2/(2\tan(\Delta_{\text{off}} - \varphi)) \ll 1$.

5.8   Appendix B: The scattering sensitivity kernel for major arcs

The scattering sensitivity kernel to compute phase velocity maps for major arcs (e.g. $\pi < \Delta_{\text{off}} < 2\pi$) can be constructed by three scattering sensitivity kernels for minor arcs. Let the scattering sensitivity kernels for the minor arcs between the source (S) and the receiver anti-pod (RA), between the receiver anti-pod and the source anti-pod (SA) and between the source anti-pod and receiver (R) be given by

$$K_{l,m}^{scat,ph,S \to RA}(\Delta_{\text{off}} - \pi, \nu) = \int_0^{\Delta_{\text{off}} - \pi} \int_0^{\pi} Y_l^m(\theta, \varphi) K^{S \to RA}(R, \theta, \varphi) d\theta d\varphi,\tag{5.40}$$

$$K_{l,m}^{scat,ph,RA \to SA}(2\pi - \Delta_{\text{off}}, \nu) = \int_{\Delta_{\text{off}} - \pi}^{\pi} \int_0^{\pi} Y_l^m(\theta, \varphi) K^{RA \to SA}(R, \theta, \varphi) d\theta d\varphi,\tag{5.41}$$

and

$$K_{l,m}^{scat,ph,SA \to R}(\Delta_{\text{off}} - \pi, \nu) = \int_{\pi}^{\Delta_{\text{off}}} \int_0^{\pi} Y_l^m(\theta, \varphi) K^{SA \to R}(R, \theta, \varphi) d\theta d\varphi,\tag{5.42}$$

where the sensitivity kernels $K^{S \to RA}(R, \theta, \varphi)$, $K^{RA \to SA}(R, \theta, \varphi)$ and $K^{SA \to R}(R, \theta, \varphi)$ are equivalent to the sensitivity kernel in Eq. (5.16) but having the epicentral distance substituted with $\Delta_{\text{off}} - \pi$, $2\pi - \Delta_{\text{off}}$ and $\Delta_{\text{off}} - \pi$, respectively. In order to derive the sensitivity kernel $K_{l,m}^{scat,ph}(\Delta_{\text{off}}, \nu)$ due to scattering theory for major arcs, the integration along the source-receiver line is split up into the three minor arc integrations. Hence,

$$
\begin{aligned}
K_{l,m}^{scat,ph}(\Delta_{\text{off}}, \nu) \quad &= \frac{1}{\Delta_{\text{off}}} \bigg(\quad (\Delta_{\text{off}} - \pi) K_{l,m}^{scat,ph,S \to RA}(\Delta_{\text{off}} - \pi, \nu) \\
&\quad + (2\pi - \Delta_{\text{off}}) K_{l,m}^{scat,ph,RA \to SA}(2\pi - \Delta_{\text{off}}, \nu) \\
&\quad + (\Delta_{\text{off}} - \pi) K_{l,m}^{scat,ph,SA \to R}(\Delta_{\text{off}} - \pi, \nu) \bigg),
\end{aligned}\tag{5.43}
$$

which is the formula in Eq. (5.21). Similarly by dividing the major arc into three minor arcs, the formula in Eq. (5.22) for the scattering sensitivity kernel for group velocity measurements can be derived.

5.9   Appendix C: Rotation of scattering sensitivity kernels

Dziewonski (1984) and Dahlen and Tromp (1998) show that the transformation of the spherical harmonics of angular degree l and order m from a reference coordinate system to a new coordinate system is given by

$$Y_l^m(\theta, \varphi) = \exp(im\Phi) \sum_{n=-l}^{l} \exp(in\Psi) Q_l^{m,n}(\Theta) Y_l^n(\theta', \varphi'), \qquad (5.44)$$

with the three Euler angles denoted by Φ, Ψ and Θ, and the elements of the rotation matrix are $Q_l^{m,n}(\Theta)$. The sensitivity kernel for minor arcs in Eq. (5.18) depends linearly on the spherical harmonics. This means that the sensitivity kernel for relative phase velocity using scattering theory can be transformed from the reference coordinate system to the observed coordinate system by using the relation for the transformation of spherical harmonics in Eq. (5.44). Let $K^*(R, \theta, \varphi)$ denote the sensitivity kernel in the observed coordinate system which is equivalent to the sensitivity kernel $K(R, \theta, \varphi)$ in Eq. (5.16) in the reference coordinate system. The formula in Eq. (5.44) is inserted in the scattering sensitivity kernel in Eq. (5.18). The sensitivity kernel $K_{l,m}^{scat,ph}(\Delta_{\text{off}})$ for the epicentral offset Δ_{off} in the new coordinate system is then

$$
\begin{aligned}
K_{l,m}^{scat,ph}(\Delta_{\text{off}}, \nu) &= \iint_{\mathbf{r}_S}^{\mathbf{r}_R} Y_l^m(\theta, \varphi) K^*(R, \theta, \varphi) d\theta d\varphi \\
&= \exp(im\Phi) \sum_{n=-l}^{l} \exp(in\Psi) Q_l^{m,n}(\Theta) \\
&\quad \times \int_0^{\Delta_{\text{off}}} \int_0^{\pi} Y_l^n(\theta', \varphi') K(R, \theta', \varphi') d\theta' \varphi' \\
&= \exp(im\Phi) \sum_{n=-l}^{l} \exp(in\Psi) Q_l^{m,n}(\Theta) K_{l,n}^{scat,ph}(\Delta_{\text{off}}, \nu), \quad (5.45)
\end{aligned}
$$

with the scattering sensitivity kernel for relative phase velocity given by

$$K_{l,n}^{scat,ph}(\Delta_{\text{off}}, \nu) = \int_0^{\Delta_{\text{off}}} \int_0^{\pi} Y_l^n(\theta', \varphi') K(R, \theta', \varphi') d\theta' d\varphi', \qquad (5.46)$$

at offset Δ_{off} computed in the reference coordinate system.

The scattering sensitivity kernels in Eq. (5.21) and (5.22) for major arcs are composed by three scattering sensitivity kernels for minor arcs. It is therefore possible to apply the

transformation of spherical harmonics in Eq. (5.44) on each scattering sensitivity kernel for minor arcs in order to obtain the same result as in Eq. (5.45) but with the scattering kernel for major arcs computed in the reference coordinate system. In addition, the result in Eq. (5.45) is valid for major arc sensitivity kernels using scattering theory to compute group velocity maps.

Chapter 6

The practical implementation of spectral leakage theory in global surface wave tomography

Abstract.

We investigate the effect of uneven ray path coverage in global surface wave tomography. An inhomogeneous distribution of seismicity may bias tomographic models because certain areas are better sampled than others. It is possible to suppress the bias due to the inhomogeneous ray path coverage by using a linear inversion technique known as spectral leakage theory that differs only from the general least squares solution in the way that data are weighted. In spectral leakage theory, the data weighting matrix is the summation of the data covariance matrix and a matrix that accounts for the simulation of even ray path coverage. Spectral leakage theory is applied together with surface wave scattering theory in an inversion of phase velocity measurements for Love waves between 40 s and 150 s. Surface wave scattering theory has a larger validity in media with small-scale heterogeneity for which the conditions for the ray theoretical great circle approximation are not satisfied. Phase velocity maps for Love waves at 40 s and 150 s from the undamped spectral leakage inversion are compared with those from the least squares inversion without any regularisation condition in use. It is concluded from the comparison of surface wave models from these two linear inversions that the simulation of homogeneous ray path coverage in the global surface wave tomographic experiment improves the phase velocity maps that correlate better with tectonic features.

6.1   Introduction

High-resolution tomographic surface wave models of the Earth may contain significant errors because of the limitations of the methodology in surface wave tomography; First,

most surface wave tomographic experiments are based on the ray theoretical great circle theorem (Jordan, 1978; Trampert and Woodhouse, 1995; van der Lee and Nolet, 1997; Curtis *et al.*, 1998) which is only valid in smooth media. However, present-day surface wave models show characteristic length-scales of heterogeneity that are at the limits to justify the use of the great circle approximation in global and regional, high-resolution surface wave models (Passier and Snieder, 1995; Spetzler *et al.*, 2001). It is therefore important to take the scattering of surface waves into account in order to obtain surface wave Earth models with a higher resolution than is currently possible. Second, due to the practical limitations of inversion techniques in surface wave tomography, it is common to truncate the series of basis functions that is used to model the structure of the Earth to a certain (arbitrary) level. The truncation of the expansion of basis functions may lead to spectral leakage which means that the contribution of small-scale structures of heterogeneity that is not accounted for in the inversion may leak into the inverted tomographic model of inhomogeneity (Trampert and Snieder, 1996). The spectral leakage problem is related to the uneven ray path coverage in surface wave tomography on the globe (Gudmundsson *et al.*, 1990; Snieder *et al.*, 1991; Iyer and Hirahara, 1993). This in its turn is due to the nature of global tomographic wave experiments where earthquakes are used as the source of waves to probe the interior of the Earth.

The main focus in this article is on the spectral leakage problem in a global surface wave tomographic experiment using phase velocity measurements for Love waves between 40 s and 150 s. The surface wave data are from Trampert and Woodhouse (2001). Instead of making use of the great circle approximation, we benefit from the methodological improvements in surface wave scattering theory of Spetzler *et al.* (2001). The employed scattering theory of surface waves is a linear theory where the relative phaseshift is expressed as a volume integration of the relative velocity perturbation field multiplied by the Fréchet kernel. The reader is referred to Spetzler *et al.* (2001) for more information about surface wave scattering theory.

In order to compensate for the uneven distribution of earthquake and receiver positions in global surface wave tomography, we make use of the work of Trampert and Snieder (1996) who develop a least-squares technique to suppress the artifacts due to spectral leakage. The difference between the least squares solution taking account of the spectral leakage problem and the general least squares inversion (Tarantola, 1987; Menke, 1989) is the way that data are weighted. In Trampert and Snieder (1996), the data weighting matrix is the sum of the data covariance matrix and another matrix that is used to suppress the effects of spectral leakage.

The elements of the matrix that accounts for the effects of spectral leakage in the spectral leakage inversion is only defined for scattering theory and not for ray theory. This is because these matrix elements correspond to the volume integration over the sphere of the Fréchet kernels due to the source-receiver configurations under consideration. For ray theory, the Fréchet kernel is the delta-function, and the integration of two delta-functions is not defined matematically.

The spectral leakage problem is considered by others in geophysics. For instance, Dziewonski and Anderson (1981) eliminate the bias introduced by unequally distributed seismicity in lateral structures by taking the average of body wave traveltime curves for

Earth sections with equal area in order to obtain the one dimensional PREM model. Snieder *et al.* (1991) set up a synthetic experiment using an artificial set of evenly distributed source-receiver pairs and a realistic set of inhomogeneous ray path coverage. In this way, they show that the spectral leakage problem originates from unevenly distributed source-receiver pairs. The spectral leakage problem is not only applicable to a truncation of the series of basis functions as it is the case in surface wave tomography (Trampert and Woodhouse, 1995; Trampert and Woodhouse, 2001; Spetzler *et al.* 2001). Arkani-Hamed *et al.* (1994) who work with the Earth's magnetic field, expand the perturbation field of a magnetic anomaly map into spherical harmonics with angular degrees from 15 to 60. In that case, the effect of spectral leakage may be relevant for the lower and upper truncation of the series of the spherical harmonics.

In section 6.2, the theory correcting for the spectral leakage problem as found in Trampert and Snieder (1996) is briefly reviewed. It is explained in section 6.3, how the least squares solution from spectral leakage theory is combined with surface wave scattering theory in global surface wave tomography. The surface wave tomographic models obtained in the spectral leakage inversion of phase velocity measurements for Love waves at 40 s and 150 s are discussed in section 6.4, while a discussion and conclusions are given in section 6.5.

6.2   Theory

In this section, we explain the basic principles behind spectral leakage theory which is described in detail by Trampert and Snieder (1996) and Snieder and Trampert (1999). In general, the model parameter $m(x)$ at point x containing the complete set of basis functions $B_j(x)$ with the coefficients m_j can be decomposed into the part $m_L(x)$ which is the basis function expansion until the (arbitrary) truncation level L, and the part $m_\infty(x)$ that is the infinite series of the remaining basis functions, thus

$$m(x) = \sum_{j=1}^{\infty} m_j B_j(x) = m_L(x) + m_\infty(x), \qquad (6.1)$$

with

$$m_L(x) = \sum_{j=1}^{L} m_j B_j(x), \quad \text{and} \quad m_\infty(x) = \sum_{j=L+1}^{\infty} m_j B_j(x). \qquad (6.2)$$

Following the notation of Menke (1989), the datum d_i in continuous inverse theory is given by

$$d_i = \int G_i(x) m(x) dx + e_i, \qquad (6.3)$$

where $G_i(x)$ is the continuous data kernel and e_i is the error of datum d_i. By inserting the series of basis functions in Eq. (6.1) for the model parameter $m(x)$ in the datum in Eq.

(6.3), the data can be related to the infinitely dimensional discrete model vector with the coefficients m_j. Hence,

$$d_i = \sum_{j=1}^{\infty} A_{ij} m_j + e_i, \tag{6.4}$$

where the modeling matrix elements

$$A_{ij} = \int G_i(x) B_j(x) dx, \tag{6.5}$$

are the projection of the data kernel $G_i(x)$ on the basis functions $B_j(x)$ (Snieder and Trampert, 1999). In more general terms, the discrete forward problem in eq. (6.4) is written as

$$\mathbf{d} = \mathbf{Am} + \mathbf{e}, \tag{6.6}$$

which is the well-known linear forward problem in vector form (Tarantola, 1987; Menke, 1989). Given the truncation level L, the least squares solution to the linear problem in Eq. (6.6) is given by

$$\tilde{\mathbf{m}}_L = \mathbf{A}_L^{-g} \mathbf{d}, \tag{6.7}$$

with the inverse of the modeling matrix $\mathbf{A}_L$ in the least squares sense given by

$$\mathbf{A}_L^{-g} = \left(\mathbf{A}_L^t \mathbf{C}_d^{-1} \mathbf{A}_L + \mathbf{C}_{m,L}^{-1} \right)^{-1} \mathbf{A}_L^t \mathbf{C}_d^{-1}. \tag{6.8}$$

The modeling matrix $\mathbf{A}_L$ is constructed for the model parameters until the (arbitrary) truncation level L, and the covariance matrix for the truncated prior model vector $\mathbf{m}_L$ and the observed data $\mathbf{d}$ is denoted by $\mathbf{C}_{m,L}$ and $\mathbf{C}_d$, respectively. (Tarantola, 1987; Menke, 1989)

The observed data in the general linear problem in Eq. (6.6) are affected by both vectors $\mathbf{m}_L$ and $\mathbf{m}_\infty$ of the coefficients m_j, hence

$$\mathbf{d} = \mathbf{A}_L \mathbf{m}_L + \mathbf{A}_\infty \mathbf{m}_\infty + \mathbf{e}, \tag{6.9}$$

where $\mathbf{A}_\infty$ is the modeling matrix for the infinitely-dimensional vector $\mathbf{m}_\infty$. The expression for the observed data in Eq. (6.9) is inserted in the least squares solution in Eq. (6.7), thereby enabling us to show the effect of spectral leakage. According to Snieder and Trampert (1999), the truncated vector $\tilde{\mathbf{m}}_L$ of the estimated model vector to the truncation level L is given by

$$\tilde{\mathbf{m}}_L = \mathbf{m}_L + \left(\mathbf{A}_L^{-g} \mathbf{A}_L - \mathbf{I} \right) \mathbf{m}_L + \mathbf{A}_L^{-g} \mathbf{A}_\infty \mathbf{m}_\infty + \mathbf{A}_L^{-g} \mathbf{e}. \tag{6.10}$$

The last three terms in Eq. (6.10) are responsible for the discrepancy in the estimated model from the true model $\mathbf{m}_L$. The second term and the last term account for the limitations in finite-resolution within the subspace for the vector $\mathbf{m}_L$ of the model coefficients,

and the effects of the observational data errors $\mathbf{e}$. The remaining term $\mathbf{A}_L^{-g}\mathbf{A}_\infty\mathbf{m}_\infty$ is the projection of the data contribution from the vector $\mathbf{m}_\infty$ of model coefficients onto the truncated vector $\tilde{\mathbf{m}}_L$ of model coefficients. This term describes spectral leakage.

The cure for spectral leakage is given in Trampert and Snieder (1996) and Snieder and Trampert (1999). In the least squares sense, they show how the solution for the truncated model vector including the spectral leakage correction is derived. In this paper, only the simplest case that the covariance matrix for the data $\mathbf{C}_d = \sigma_d^2\mathbf{I}$, and for the model vectors $\mathbf{C}_{m,L} = \sigma_{m,L}^2\mathbf{I}$ and $\mathbf{C}_{m,\infty} = \sigma_{m,\infty}^2\mathbf{I}$, is considered. Trampert and Snieder (1996) define $\alpha^2 = \sigma_d^2/\sigma_{m,L}^2$ and $\beta^2 = \sigma_d^2/\sigma_{m,\infty}^2$. The least squares solution $\tilde{\mathbf{m}}_L^W$ with the spectral leakage correction is given by

$$\tilde{\mathbf{m}}_L^W = \left(\mathbf{A}_L^t\mathbf{W}\mathbf{A}_L + \left(\frac{\alpha^2}{\beta^2}\right)\mathbf{I}\right)^{-1}\mathbf{A}_L^t\mathbf{W}\mathbf{d}, \tag{6.11}$$

with the anti-leakage matrix

$$\mathbf{W} = \left(\mathbf{A}_\infty\mathbf{A}_\infty^t + \beta^2\mathbf{I}\right)^{-1}. \tag{6.12}$$

The anti-leakage matrix in Eq. (6.12) is the inverse of the sum of the matrix $\mathbf{A}_\infty\mathbf{A}_\infty^t$ that is used to suppress the spectral leakage effect and the diagonal matrix $\beta^2\mathbf{I}$ that includes the variance of the data and the infinitely dimensional model vector $\mathbf{m}_\infty$.

6.3 Spectral leakage theory in global surface wave tomography

In this section, it is explained how the inverse problem with the spectral leakage correction is set up in global surface wave tomography using phase velocity measurements. The relative phaseshift d_{scat} due to the scattering of surface waves is calculated as a summation of the spherical harmonics coefficients C_l^m multiplied by the Fréchet kernel $K_{l,m}^{scat}$ for angular degree l and order m using diffraction theory. Scattering theory for unconverted surface waves is derived in Spetzler *et al.* (2001). The relative phaseshift is given by

$$d_{scat} = \sum_{l=0}^{l_{max}} \sum_{m=-l}^{l} C_l^m K_{l,m}^{scat}, \tag{6.13}$$

with the maximum angular degree of the spherical harmonic expansion denoted by l_{max}, which is a finite number in practical applications. The Fréchet kernel $K_{l,m}^{scat}$ for angular degree l and order m is the integration of the sensitivity function $K^{scat}(R,\theta,\varphi)$ due to the scattering of surface waves and the spherical harmonic $Y_l^m(\theta,\varphi)$ over the sphere Ω. Hence,

$$K_{l,m}^{scat} = \int_\Omega K^{scat}(R,\theta,\varphi)Y_l^m(\theta,\varphi)d\theta d\varphi. \tag{6.14}$$

The reader is referred to Fig. 1 in Spetzler *et al.* (2001) for examples of the sensitivity function $K^{scat}(R, \theta, \varphi)$. By comparing the expression for the modeling matrix in Eq. (6.5) with the Fréchet kernel in eq. (6.14), we identify that the data kernel $G_i(x)$ corresponds to $K^{scat}(R, \theta, \varphi)$ and the basis functions $B_j(x)$ are the spherical harmonics $Y_l^m(\theta, \varphi)$. It is shown on p. 154 in Snieder and Trampert (1999) that the matrix product $\mathbf{A}_\infty \mathbf{A}_\infty^t$ in Eq. (6.12) using the notation for surface wave scattering theory can be written as

$$\{\mathbf{A}_\infty \mathbf{A}_\infty^t\}_{ij} = \int_\Omega K_i^{scat}(R, \theta, \varphi) K_j^{scat}(R, \theta, \varphi) d\theta d\varphi - \{\mathbf{A}_L \mathbf{A}_L^t\}_{ij}, \qquad (6.15)$$

where the subindex in the sensitivity functions indicate the source-receiver pairs i and j. In terms of surface wave scattering theory, it makes sense to evaluate the integration of the two weighting functions in Eq. (6.15), because they are defined everywhere over the sphere. In contrast, the integration part (known as the Gram matrix, Trampert and Snieder, 1996) in Eq. (6.15) is not defined for ray theory; the data kernel $K_i^{ray}(R, \theta, \varphi)$ due to ray theory on the sphere is a delta-function depending on the spherical coordinates. The integration of the product of two delta-functions on the sphere yields zero, so the Gram matrix is not defined in terms of ray theory. In addition, the application of the ray-theoretical great circle approximation in global surface wave tomography is limited to structures with angular degrees of the spherical harmonics smaller than $l = 30$ for Love waves at 40 s and $l = 20$ for Love waves at 150 s (Spetzler *et al.*, 2001).

The anti-leakage matrix $\mathbf{W}$ in Eq. (6.12) has the number of rows and columns equal to the number of data applied in the inverse problem. If many data are used in the tomographic experiment, the matrix $\mathbf{W}$ is large which may cause problems when storing it in the computer memory (or even on the hard-disc). In the global surface wave tomographic experiment using phase velocity measurements, the elements of the matrix $\mathbf{A}_\infty \mathbf{A}_\infty^t$ in the anti-leakage matrix $\mathbf{W}$ are calculated from the matrix product

$$\{\mathbf{A}_\infty \mathbf{A}_\infty^t\}_{ij} = \sum_{s=L+1}^{\infty} \{\mathbf{A}_\infty\}_{is} \{\mathbf{A}_\infty^t\}_{sj}, \qquad (6.16)$$

instead of using the expression for $\mathbf{A}_\infty \mathbf{A}_\infty^t$ in Eq. (6.15) for which the evaluation of the integral is numerically demanding. In practice, the summation over s in eq. (6.16) is limited to a certain maximum angular degree l_{max} of the spherical harmonics expansion much higher than the truncation level L.

The off-diagonal elements of the anti-leakage matrix in Eq. (6.12) are significant if different source-receiver pairs are parallel and close to each other or if different source-receiver minor arcs or major arcs cross at an oblique angle so that their Fresnel zones overlap. In general, the anti-leakage matrix $\mathbf{W}$ is symmetric, and it is found that $\mathbf{W}$ is sparse as well for the Love wave dataset between 40 s and 150 s from Trampert and Woodhouse (2001). The sparseness of $\mathbf{W}$ comes from the fact that many of the source-receiver pairs do not have overlapping Fresnel zones. However for Love waves at both 40 s and 150 s, several of the off-diagonal elements of the anti-leakage matrix are comparable with the diagonal elements of $\mathbf{W}$ because the respective source-receiver pairs are close to each other. The matrix $\mathbf{W}$ must therefore be inverted by brute force (such as Gaus-
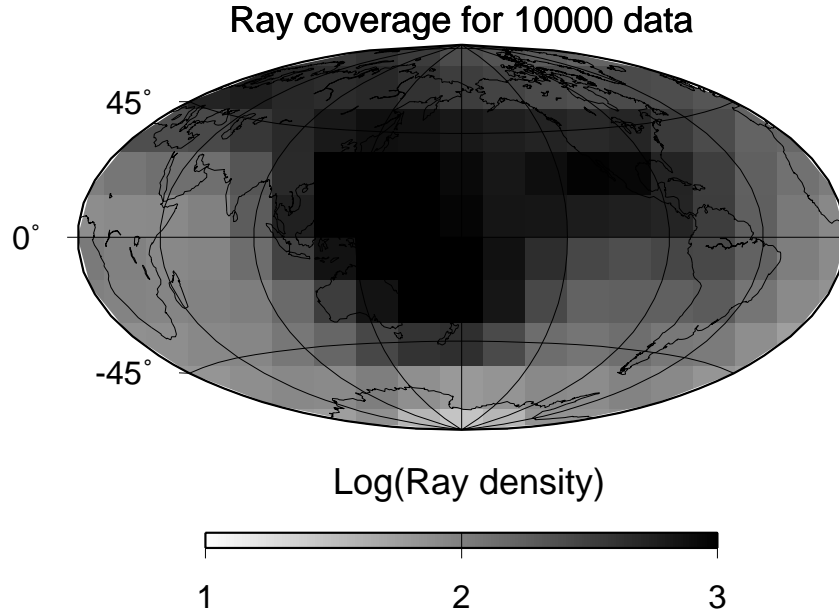
Figure 6.1: *The ray coverage density for the dataset of the 10000 relative phaseshifts for Love waves between 40 s and 150 s. The grey colour scale shows the logarithmic value of the ray path coverage density.*

Jordan elimination, see Press *et al*., 1986) as the form of the sparse anti-leakage matrix is irregular.

In the inversion of phase velocity measurements for Love waves between 40 s and 150 s using spectral leakage theory, we apply 10000 surface wave data from Trampert and Woodhouse (2001). Note that all the global surface wave Earth models presented here are estimated from the same 10000 phase velocity measurements for Love waves between 40 s and 150 s. The ray density for the Love wave dataset of 10000 relative phaseshift measurements is shown in Fig. 6.1. Notice that the ray density is shown on a logarithmic-scale. It is clearly seen that the phase velocity models presented later in this paper are sampled with an uneven path distribution. We find the highest ray path coverage on the Pacific plate, in Eurasia and in North America while the poorest sampling rate is found on the Southern hemisphere with an emphasis on the Southpole.

The value of α in Eq. (6.11) is set to zero, which corresponds to an inversion without any damping. The value of β in Eq. (6.12) is chosen by trial and error using the conditions that the phase velocity maps from the spectral leakage inversion are stable. We found that the lowest value of β which is $\beta = 0.5$, satisfies this condition.

According to Eq. (6.10) the estimated model $\tilde{\mathbf{m}}_L$ differs from the true model $\mathbf{m}_L$ because of the three distinct contributions that are $(\mathbf{R} - \mathbf{I})\mathbf{m}_L$ (resolution limitation), $\mathbf{A}_L^{-g}\mathbf{A}_\infty \mathbf{m}_\infty$ (spectral leakage effect) and $\mathbf{A}_L^{-g}\mathbf{e}$ (data error propagation). The resolution

matrix is given by $\mathbf{R} = \mathbf{A}_L^{-g}\mathbf{A}_L$ (Tarantola, 1987; Menke, 1989). Firstly, because there is no need for a regularisation condition in the spectral leakage inversion ($\alpha = 0$), the resolution matrix $\mathbf{R} = \mathbf{I}$ (see appendix A). Secondly, we use spectral leakage theory in the global phase velocity experiment, so the leakage term $\mathbf{A}_L^{-g}\mathbf{A}_\infty\mathbf{m}_\infty = \mathbf{0}$. The estimated surface wave models using spectral leakage theory are therefore only affected by the un-certainty from the data error propagation. Hence,

$$\tilde{\mathbf{m}}_L = \mathbf{m}_L + \mathbf{A}_L^{-g}\mathbf{e}. \tag{6.17}$$

The truncation level is $L = 20$ and $L = 10$ for Love waves at 40 s and 150 s, respec-tively, which assures stable surface wave models when applying spectral leakage theory. It is shown in Fig. 5 of Trampert and Snieder (1996) that mostly the lower degree basis functions, $Y_{l,m}$, just above the truncation level bias the highest degree spherical harmonics below the truncation level. The maximum angular degree and order of the Fréchet kernels that is used to compute the elements of the anti-leakage matrix in Eq. (6.12) is set to l_{max} = 40, because it is unlikely that higher degree spherical harmonics larger than $l_{max} = 40$ leak into the spherical harmonics with angular degrees smaller than the truncation level at angular degree $L = 20$ and $L = 10$ for Love waves at 40 s and 150 s, respectively.

6.4   Phase velocity maps from the spectral leakage inver-sion of relative phaseshifts

The relative phase velocity maps for Love waves at 40 s and 150 s corrected for the spectral leakage effect are shown in Fig. 6.2A and 6.3A, respectively. The surface wave models from the spectral leakage inversion are compared with those for Love waves at 40 s (Fig. 6.2B) and 150 s (Fig. 6.3B) which are retrieved in a common least squares estimation (see Eq. (6.8)) without any regularisation in use ($\mathbf{C}_d^{-1} = \mathbf{I}$, and $\mathbf{C}_{m,L}^{-1} = \mathbf{0}$). The reader is referred to appendix A for a discussion about the fairness of the comparison of the phase velocity models from the undamped spectral leakage inversion and the com-mon least squares inversion without applying a regularisation condition. The grey-scale colour for the relative phase velocity perturbations in Fig. 6.2 and 6.3 is between $\pm$ 5 % compared to the PREM-model for Love waves at the respective periods in order to show detailed structures of all the phase velocity models presented here. However, the relative phase velocity perturbations in the inversion of the relative phaseshifts for Love waves at 40 s are between -15 % and 17 %, and for Love waves at 150 s the minimum pertur-bation is - 7 % and the maximum phase velocity perturbation is 9 %. The surface wave models for Love waves at 40 s may seem identical which is an artifact due to the applied grey-scale colours ranging between $\pm$ 5 % for the relative velocity perturbations that are between -15 % and 17 %.

The difference between the phase velocity maps obtained in the two separate inver-sions are plotted in Fig. 6.4A for Love waves at 40 s and in Fig. 6.4B for Love waves at 150 s. The abbreviation 'usli' stands for the undamped spectral leakage inversion, and 'cls' refers to the common least squares inversion without applying any regularisation

condition. Unfortunately, the difference in relative phase velocity between the surface wave models from the undamped spectral leakage inversion and the common undamped least squares inversion is not entirely due to the effect of spectral leakage. There might be some contribution of data error propagation in the differences of relative phase velocity in Fig. 6.4A and 6.4B, because the inverse of the modeling matrix $\mathbf{A}_L^{-g}$ is not the same in the spectral leakage inversion and in the common least squares inversion. A scale analysis of the difference between the inverse of the modeling matrix $\mathbf{A}_L^{-g}$ in the spectral leakage estimation and in the least squares inversion that is compared to the inverse of the modeling matrix in the spectral leakage inversion has been carried out. This scale analysis reveals that the difference between the inverse of the modeling matrix in the spectral leakage inversion and in the least squares inversion is not negligible. On the other hand, the global surface wave experiment is well-constrained because we use many data and because we do not need to apply any damping in the inversion of phase velocity measurements using spectral leakage theory or the least squares estimation (see appendix A for a discussion of the comparison of the relative phase velocity models from the two separate linear inversions). We therefore believe that the contribution of data error is not significant in the global surface wave experiment. It is seen in Fig. 6.4 that the effect of the anti-leakage matrix is significant as there are large differences in the small-scale structures of the surface wave models obtained in the two kind of inversions. The characteristic wavelength of the differences in the small-scale relative phase velocity structure is comparable to the truncation level of the series of the spherical harmonics. Thus for the inversion of Love waves at 40 s the length-scale of differences of relative phase velocity is about $l \approx 20$ (or corresponding to 2000 km), and for the experiment with Love waves at 150 s the difference in structure has a characteristic length of $l \approx 10$ (or corresponding to 4000 km). This observation shows that the effect of spectral leakage is most important at the truncation level, which is as well shown by in Fig. 5 of Trampert and Snieder (1996).

Qualitatively, the phase velocity maps for Love waves at 40 s and 150 s from the undamped spectral leakage inversion correlate better with tectonic features than those from the common least squares inversion without applying a regularisation condition. For instant look at Fig. 6.5 where two sections of the Love wave model at 40 s from the two separate inversions are presented. The section for Fig. 6.5A and 6.5B contains the area with Africa, Tibet and the Carlsberg ridge, while the section for Fig. 6.5C and 6.5D is the region with South America, the East Pacific rise and the Chile rise. These two sections are the most clear examples for the Love wave models at 40 s. It is clearly seen from Fig. 6.3 that the phase velocity maps for Love wave at 150 s using the undamped spectral leakage solution have a better correlation with tectonic boundaries than the surface wave models obtained in the common least squares estimation without any regularisation condition in use. For examples in Fig. 6.3, we stress out the Carlsberg ridge, the South-West Indian ridge, the Hunter ridge and the Chile rise.

In Fig. 6.6, the unexplained variance that is a measure of how well the Love wave phase velocity maps explain the observed data, is plotted for values of $(\alpha/\beta)^2$ ranging from zero to 30. In general, the unexplained variance increases for increasing values of $(\alpha/\beta)^2$. Nevertheless, it is shown most clearly in the spectral leakage inversion for Love waves at 150 s that the value of α giving the minimum unexplained variance is not for

A) Spectral leakage inversion: Love 40 sec

Rel. phase velocity perturbations (%)

-5   0   5

B) Least squares inversion: Love 40 sec

Rel. phase velocity perturbations (%)

-5   0   5
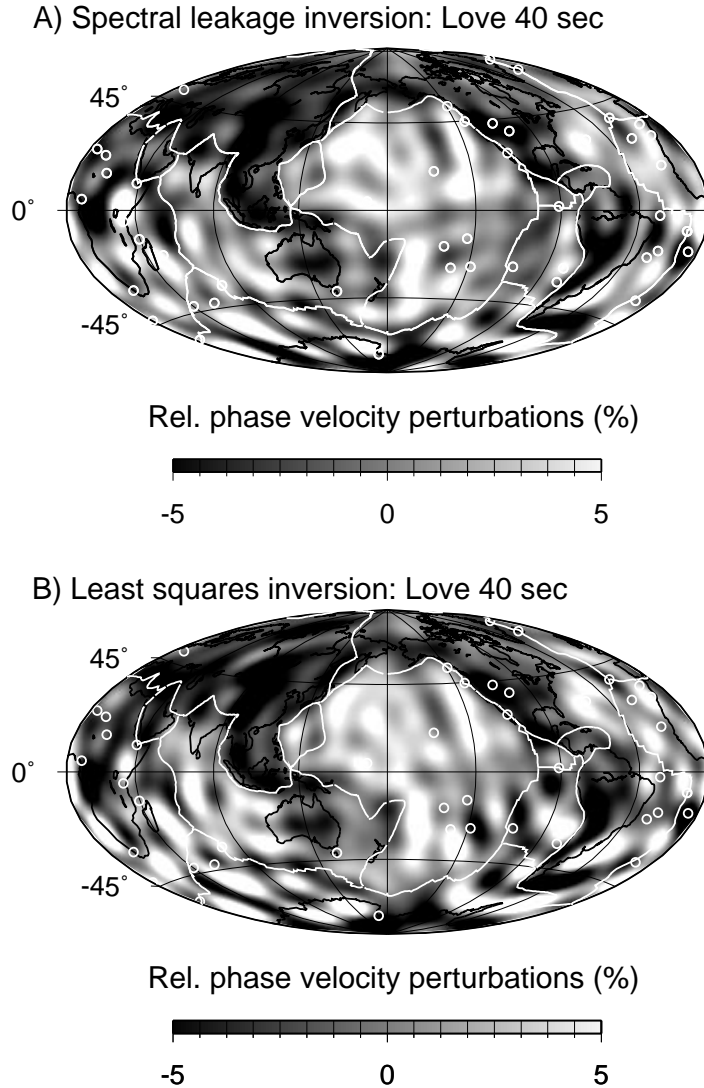
Figure 6.2: *Global phase velocity Earth models for Love waves at 40 s. The white circles are hotspots, the white lines show the boundaries between tectonic plates and coastlines are drawn with the thick black lines. The variations in the relative phase velocity pertur-bations are given in percent on a scale ± 5 % with respect to the constant PREM model for Love waves at 40 s. The series of the spherical harmonics is truncated at the angular degree L = 20. A) The phase velocity map that is obtained in the inversion accounting for the spectral leakage problem. The parameters* α = 0 *and* β = 0.5. *B) The phase velocity map that comes from the common least squares inversion without using any damping.*

A) Spectral leakage inversion: Love 150 sec

Rel. phase velocity perturbations (%)

-5   0   5

B) Least squares inversion: Love 150 sec

Rel. phase velocity perturbations (%)

-5   0   5
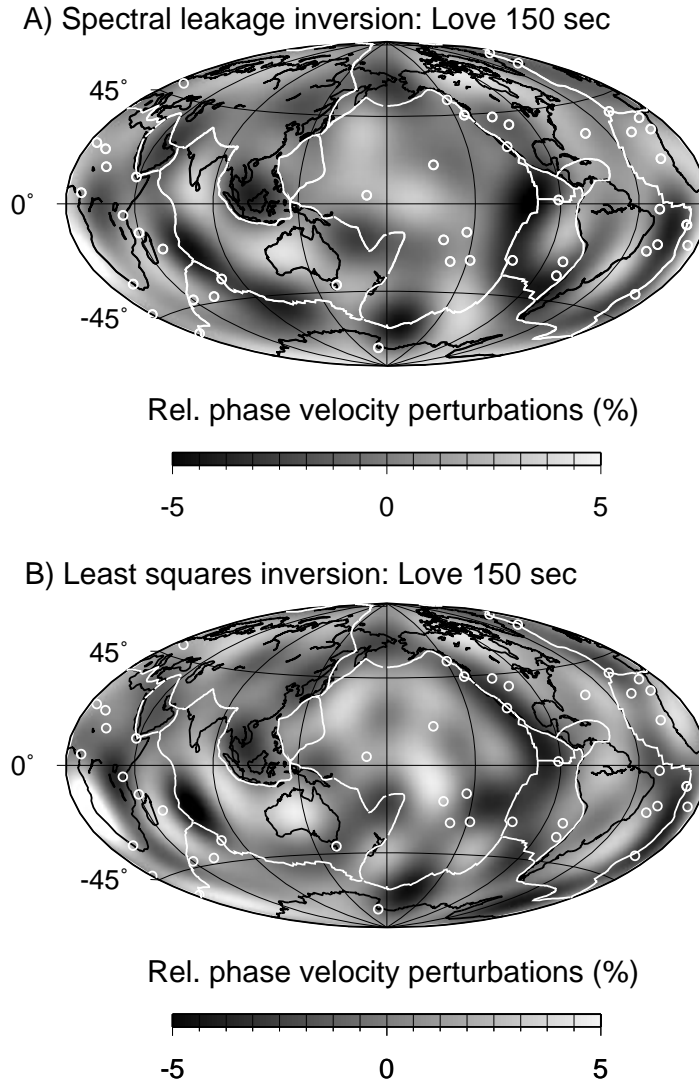
Figure 6.3: *As in Fig. 6.2, but for this figure Love waves at 150 s are used in the two separate linear inversions without applying any damping. The series of the spherical harmonics is truncated at the angular degree L = 10. The variations in the relative phase velocity perturbations are given in percent on a scale ± 5 % with respect to the constant PREM model for Love waves at 150 s. A) The phase velocity map obtained in the inversion that suppresses the spectral leakage effect. The value of α is zero and β is set to 0.5. B) The phase velocity map that is retrieved from the common least squares inversion without using any regularisation condition.*

A) usli - cls: Love 40 sec

Rel. phase velocity perturbations (%)

-5   0   5

B) usli - cls: Love 150 sec

Rel. phase velocity perturbations (%)

-5   0   5
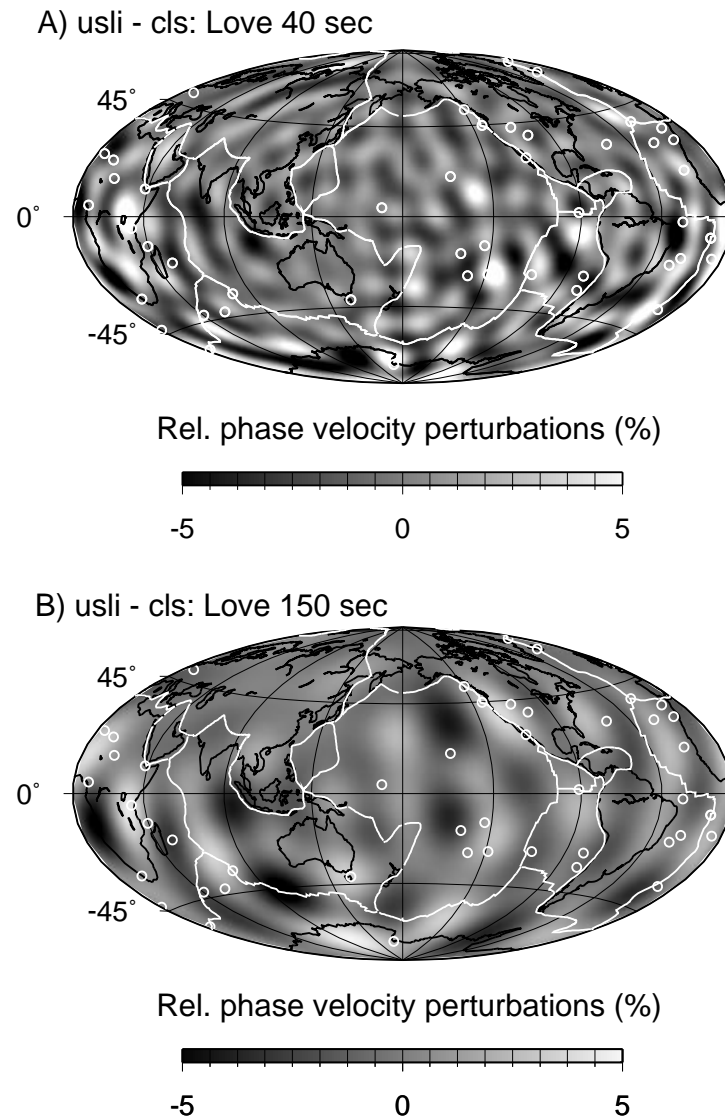
Figure 6.4: *The difference between the phase velocity maps obtained in the undamped spectral leakage inversion (usli) without any damping and the common least squares (cls) inversion with no regularisation condition in use. The convention for hotspots, plate boundaries and coast lines is the same as in Fig. 6.2. A) The inversion of relative phase-shifts for Love waves at 40 s. B) The inversion of the phase velocity measurements for Love waves at 150 s.*
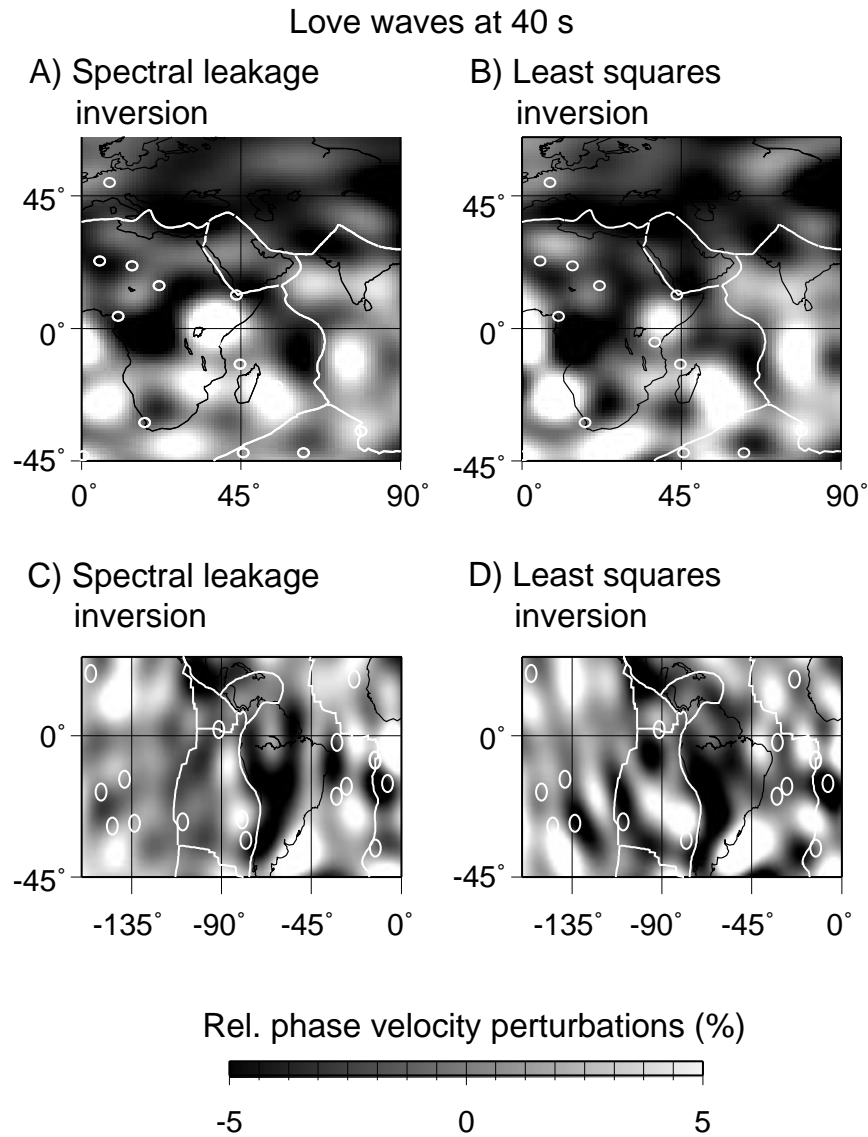
Figure 6.5: *Selected sections of the phase velocity maps for Love wave at 40 s and 150 s that are shown in Fig. 6.2. The colour convention for hotspots, plate boundaries and coast lines is unchanged from Fig. 6.2. For A) and B), the section includes Africa, Tibet and the Carlsberg ridge. For C) and D), the section is the region with the east Pacific rise, the Chile rise and South America.*
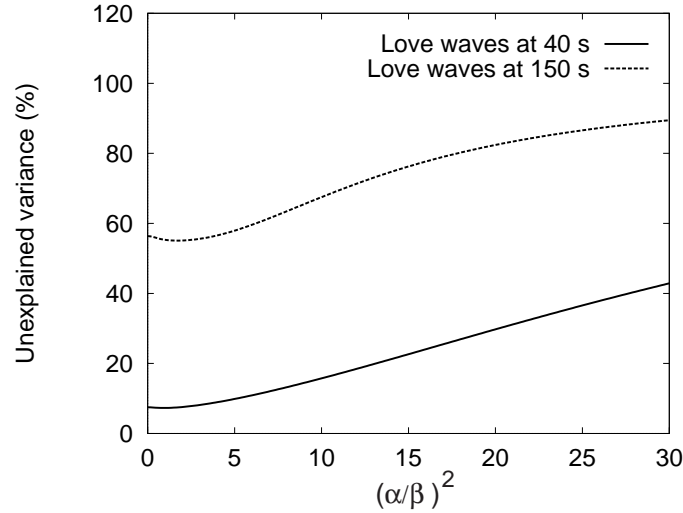
Figure 6.6: *The unexplained variance in percent for different values of* $(\alpha/\beta)^2$ *in the spectral leakage inversion of phase velocity measurements for Love waves at 40 s and 150 s, respectively. If* $(\alpha/\beta)^2$ *is equal to zero, this corresponds to an inversion with no regularisation. The estimated phase velocity maps for Love waves at 40 s and 150 s converge towards the homogeneous PREM reference model as the value of* $(\alpha/\beta)^2$ *increases.*

$\alpha = 0$ but for $\alpha \approx 2$. When $(\alpha/\beta)^2$ is large in the spectral leakage inversion, the estimated phase velocity models for Love waves at 40 s and 150 s are close to the homogeneous PREM reference model because a large value of $(\alpha/\beta)^2$ corresponds to an inversion with a restrictive regularisation condition.

6.5   Discussion and conclusions

The presented Love wave phase velocity models from the spectral leakage inversion are obtained without using any damping ($\alpha = 0$). This means that only the effects of data error propagation contribute to the surface wave models for Love waves at 40 s and 150 s which are estimated in the inversion of phase velocity measurements using spectral leakage theory.

   The phase velocity maps for Love waves at 40 s and 150 s obtained in the spectral leakage inversion without any damping are compared with those that are estimated in a common least squares inversion without using any regularisation condition. Among these two linear inversion approaches, the surface wave models from the spectral leakage inversion correlate better with many tectonic features such as ridges (e.g. the Carlsberg ridge, the South-West Indian ridge, the Hunter ridge and the southern part of the Mid-Atlantic ridge) and rises (i.e. the East Pacific rise and the Chile rise).

Spectral leakage theory is numerically rather demanding, because the anti-leakage matrix must be inverted by brute force. Every time the number of data doubles it takes 8 times more processor time to invert the anti-leakage matrix (Press *et al*., 1986). This problem imposes a limitation on the number of surface wave data that is feasible to invert for in a reasonable amount of time. For instance, the spectral leakage inversion of 10000 Love wave relative phaseshifts takes 2 day on a 250 MHz ultra-sparc machine, so an inversion of 20000 surface wave data takes 16 days. It would therefore be rewarding to find a way to invert the anti-leakage matrix much faster by exploiting the symmetric and sparse property of the anti-leakage matrix.

References

Arkani-Hamed J., Langel R. A. and Purucker M. (**1994**). Scalar magnetic anomaly maps of the Earth from POGO and Magsat data, J. Geophys. Res. **99**, 24075-24090.

Curtis A., Trampert J., Snieder R. and Dost B. (**1998**). Eurasian fundamental mode surface wave phase velocities and their relationship with tectonic structures, J. Geophys. Res. **103**, 26919-26947.

Dziewonski M. A. and Anderson D. L. (**1981**) Preliminary reference Earth model, Phys. Earth Planet. Inter. **25**, 297-356.

Gudmondsson O., Davies J. H. and Clayton R. W. (**1990**). Stochastic analysis of global traveltime data: mantle heterogeneity and random errors in the ISC data, J. Geophys. Res. **102**, 25-43.

Iyer H. M. and Hirahara K. (**1993**). *Seismic tomography; theory and pratice* (Chapman and Hall.).

Jordan T. H. (**1978**). A procedure for estimating lateral variations from low frequency eigenspectra data, Geophys. J. R. astr. Soc. **52**, 441-455.

van der Lee S. and Nolet G. (**1997**). Upper mantle *S*-velocity structure of North America, J. Geophys. Res. **102**, 22815-22838.

Menke W. (**1989**). *Geophysical data analysis: discrete inverse theory* (Academic Press, Inc.).

Passier M. L and Snieder R. (**1995**). Using differential waveform data to retrieve local S-velocity structure or path-averaged S-velocity gradients, J. Geophys. Res. **100**, 24061-24078.

Press W. H., Flannary B. P., Teukolsky S. A. and Vetterling W. I. (**1986**). *Numerical recipes: the art of scientific computation* (Cambridge University Press, UK).

Scales J. and Snieder R. (**2000**). The anatomy of inverse problems, Geophysics **65**, 1708-1710.

Snieder R., Beckers J. and Neele F. (**1991**). The effect of small-scale structure on normal mode frequencies and global inversions, J. Geophys. Res. **96**, 501-515.

Snieder R. and Trampert J. (**1999**). *Inverse problems in geophysics* in wavefield inversion, Ed. A. Wirgin (Springer Verlag, New York.).

Spetzler J., Trampert J. and Snieder R. (**2001**). The effect of scattering in surface wave tomography, Geophys. J. Int. (**Submitted**).

Tarantola A. (**1987**). *Inverse problem theory: methods for data fitting and model parameter estimation* (Elsevier, New York).

Trampert J. and Woodhouse J. H. (**1995**). Global phase velocity maps of Love and Rayleigh waves between 40 and 150 seconds, Geophys. J. Int. **122**, 675-690.

Trampert J. and Snieder R. (**1996**). Model estimations biased by truncated expansions: possible artifacts in seismic tomography, Science **271**, 1257-1260.

Trampert J. and Woodhouse J. H. (**2001**). Assessment of global phase velocity models, Geophys. J. Int. (**144**), 165-174.

6.6 Appendix A: The comparison of the phase velocity maps from the undamped spectral leakage inversion and the common undamped least squares inversion

According to Eq. (6.8), the inverse of the modeling matrix $\mathbf{A}_L$ in the least squares solution using $\mathbf{C}_d^{-1} = \mathbf{I}$ and $\mathbf{C}_{m,L}^{-1} = \mathbf{0}$ is given by

$$\mathbf{A}_L^{-g} = \left(\mathbf{A}_L^t \mathbf{A}_L\right)^{-1} \mathbf{A}_L^t. \qquad (6.18)$$

By using spectral leakage theory in Eq. (6.11), the inverse of the modeling matrix for $\alpha = 0$ (no damping) is simplified to

$$\mathbf{A}_L^{-g} = \left(\mathbf{A}_L^t \mathbf{W} \mathbf{A}_L\right)^{-1} \mathbf{A}_L^t \mathbf{W}. \qquad (6.19)$$

The only difference between the inverted modeling matrix $\mathbf{A}_L^{-g}$ in eq. (6.18) and Eq. (6.19) is the anti-leakage matrix $\mathbf{W}$, which is applied to suppress the effects of spectral leakage.

Next according to Tarantola (1987) and Menke (1989), the model resolution matrix $\mathbf{R}$ is given by

$$\mathbf{R} = \mathbf{A}_L^{-g}\mathbf{A}_L. \tag{6.20}$$

The inverse of the modeling matrix from the common least squares solution without using any regularisation condition in Eq. (6.18) and from the undamped spectral leakage estimation in Eq. (6.19) are inserted in the expression for the model resolution matrix in Eq. (6.20). Hence for the common least squares inversion without any regularisation condition in use, we get that

$$\mathbf{R} = \left(\mathbf{A}_L^t\mathbf{A}_L\right)^{-1}\mathbf{A}_L^t\mathbf{A}_L=\mathbf{I}, \tag{6.21}$$

and for the undamped spectral leakage inversion, the model resolution matrix is

$$\mathbf{R} = \left(\mathbf{A}_L^t\mathbf{W}\mathbf{A}_L\right)^{-1}\mathbf{A}_L^t\mathbf{W}\mathbf{A}_L=\mathbf{I}, \tag{6.22}$$

which is always the case for a well-conditioned overdetermined inverse problem (p. 67 in Menke, 1989).

In order to verify if the global surface wave experiment for Love waves at 40 s and 150 s is a well-posed inverse problem, the trace of the model resolution matrix is calculated in the spectral leakage inversion without any damping and the common least squares solution without any regularisation condition in use. For both separate inversions, we find that the trace of the resolution matrix for the model parameters is equal to the number of model parameters used in the inversions. The positive result of the calculation of the trace of the model resolution matrix indicates that the model resolution matrices in the two kind of undamped inversions have no zero-eigenvalues. The global surface wave experiment for Love waves between 40 s and 150 s is therefore well-conditioned either using spectral leakage theory with $\alpha = 0$ or using the common least squares estimation without any regularisation condition. The comparison of the phase velocity maps from the two separate inversions is therefore considered to be fair.

Summary and conclusions

In this thesis, the theories for wavefield-modeling and inverse problems in seismic tomography are improved. Seismic tomographic experiments are based mostly on ray theory which is valid for the description of wave propagation in media where velocity anomalies are larger in size than the wavelength and the Fresnel zone (see Fig. 1.1 in the introduction of the thesis, chapter one, for an explanation of the physical parameters). Nonetheless, the newest surface wave models of the Earth have characteristic lengths of inhomogeneity of approximately the same order as the wavelength and the Fresnel zone. This observation poses a problem from a methodological point of view, as it is inappropriate to use an approximative theory (namely ray theory) that is only valid under conditions that are not satisfied in the final result (e.g. the tomographic model). Instead, it is necessary to take the scattering of waves into account in the theory for wave propagation so that inhomogeneities with length-scales comparable with or smaller than the Fresnel zone are modeled correctly. Second, a common problem in the inversion of seismic data is that heterogeneities smaller than a certain (arbitrary) length scale are neglected due to practical reasons. However, the truncation of the allowed length-scale in surface wave tomographic experiments may introduce a systematic error in the surface wave models of the Earth.

It is shown that the timeshift can be expressed as a volume integration of the slowness perturbation field multiplied by the Fréchet kernel due to the scattering of waves. The Fréchet kernel is an analytical function in wave experiments where the straight ray approach holds. The developed scattering theory is therefore just as easy to apply as the ray theoretical approach using the great circle approximation in surface wave tomographic experiments. The Fréchet kernel depends on the experimental parameters, such as the distance between the source and receiver, the reference slowness field and the frequency content of the measured wavefield. It is shown in chapters three through five that the Fréchet kernel for finite-frequency waves has the maximum sensitivity to slowness perturbations off-path from the geometrical ray. For waves propagating in three dimensions, the sensitivity to slowness perturbations vanishes on the ray path (see Fig. 4.1B in chapter four). This is a counter-intuitive result compared with ray theory which predicts non-zero sensitivity to slowness perturbations only on the geometrical ray.

The formation of caustics is significant in small-scale structured media with strong slowness perturbations (chapter two). However, multiple arrivals associated with caustics arrive after the ballistic wavefield due to causality. It is appropriate to use the theory for the scattering of waves even though triplications form in the propagating wavefield.

The developed scattering theory is a generalisation of ray theory. One obtains the same result using either ray theory or diffraction theory in the parameter regime where ray theory is valid. In contrast, only the theory for finite-frequency waves predicts the timeshifts retrieved from a finite-difference 2-D modeling wave experiment (chapter three and four) and from a physical 3-D experiment with ultrasonic waves propagating in samples of granite (chapter four) for which scattering effects are important.

The theory for the scattering of waves is applied in global surface wave tomography for Love waves between 40 s and 150 s (chapter five). In the global surface wave experiment, it is found through a synthetic experiment that present-day global high-resolution surface wave tomographic models are at the limits of the application of the ray theoretical great circle approximation. The great circle approximation is valid in surface wave tomography as long as the characteristic length of slowness anomalies is larger than 1300 km and 2000 km for Love waves with the periods of 40 s and 150 s, respectively. Phaseshift measurements for Love waves between 40 s and 150 s are applied in separate inversions using ray theory and scattering theory. The estimated tomographic surface wave models derived from ray theory and scattering theory are similar, because a restrictive regularisation condition is incorporated in the inversion so that structures with length-scales smaller than the Fresnel zone are mostly suppressed. However, it is important in future global surface wave tomographic experiments to apply surface wave scattering theory instead of ray theory in order to obtain higher resolution models of the Earth than is presently possible.

Surface wave scattering theory is applied together with spectral leakage theory in an inversion of phase velocity measurements for Love waves between 40 s and 150 s (chapter six). The phase velocity models from the spectral leakage inversion are obtained without any damping in use, and they are therefore compared most correctly to the surface wave models from a common least squares solution without applying any regularisation condition. It is found that the estimated surface wave models for Love waves between 40 s and 150 s from the undamped spectral leakage solution correlate better with tectonic features such as plate boundaries, ridges and trenches than the phase velocity models retrieved from the common least squares solution without using any regularisation condition.

The conclusions above do not contradict the application of ray theory in tomographic wave experiments, but this thesis demonstrates examples that ray theory is not always appropriate for the description of propagating waves in media with small-scale heterogeneity. When imaging techniques are based on ray theory in a given tomographic wave experiment, it should be verified in the inverted model that the conditions for ray theory are satisfied. For complex media where the conditions for ray theory are not valid, the modeling of wave propagation should be based on scattering theory instead of ray theory.

There are several natural extensions of this thesis research. First, the scattering theoretical approach in chapter three is made as general as possible, thereby making it feasible to incorporate the non-ray geometrical effect in global body wave tomography, in regional surface wave tomography, in seismic exploration (e.g. crosswell tomography, vertical seismic profiling, reflection seismic experiments and migration theory), in medical imaging and in ocean acoustics. Second, the scattering theory in the thesis is limited to the case of isotropic, homogeneous reference media. It would be of interest to generalise the developed diffraction theory to include heterogeneity and anisotropy in the background

medium as well. Third, the Rytov approximation is here applied on the acoustic wave equation. In the case of surface wave scattering theory in chapter five, it is appropriate to use the Rytov approximation on surface waves because the approach is limited to transmitted and unconverted surface waves. It should be investigated how to generalise the Rytov approximation to elastic wavefields, so that mode conversion between surface waves or P-to-S wave conversion and vice versa can be taken into account in future tomographic wave experiments. Fourth, it is observed in synthetic aperture radar (SAR) experiments that it is possible to obtain high-resolution images of the Earth's surface with length-scales of heterogeneity that are much smaller than the width of the Fresnel zone of radar waves. The theory of the scattering of waves presented in this thesis is related to the concept of Fresnel zones, because the finite-frequency of waves is taken into account. It would be interesting to construct synthetic experiments which are identical to the SAR-experiment or to high-resolution seismic exploration experiments so that the limits of resolution in tomographic wave experiments can be investigated analytically. Lastly, the work about scattering theory by Dahlen *et al.* (2000) and Hung *et al.* (2000) indicates that non-linear effects are important (see the introduction in chapter one for references). In contrast, the scattering theory based on the Rytov approximation as found in this thesis is linearised. It is important to investigate the role of non-linearity on the propagation of waves in media where scattering effects are important.

Nederlandse samenvatting

In dit proefschrift wordt de theorie op het gebied van golfveld-modellering en inverse problemen in seismologische tomografische experimenten verbeterd. Het probleem is dat de meeste golfveld-modelleringsstechnieken in globale seismologie gebaseerd zijn op eenvoudige versies van stralentheorie. Stralentheorie geeft de oplossing van de akoestische golfvergelijking in de hoge frequentie limiet, en daarom worden de voorwaarden voor stralentheorie alleen vervuld in gladde media waar de snelheid langzaam verandert over een lengteschaal die groot is vergeleken met de golflengte en de dikte van de Fresnel zone (zie figuur 1.1 in de introductie van dit proefschift voor een verklaring van de natuurkundige grootheden). Het laatste decennium is er een tendens in de globale seismologie om te proberen de resolutie van snelheids-structuren in tomografische, regionale en globale snelheidsmodellen van de aarde te verbeteren door meer rekenkracht en betere datasets. De huidige snelheidsmodellen van de aarde in de globale seismologie laten zien dat de meest voorkomende lengte van heterogeniteiten dezelfde orde van grootte heeft als de golflengte en de Fresnel zone van het gemeten golfveld. Dit betekent dat de voorwaarden voor stralentheorie in het algemeen niet worden vervuld bij de huidige snelheidsmodellen van de aarde. Daarom moet verstrooiingstheorie worden gebruikt om te beschrijven hoe golven zich voortplanten in media waar de voorwaarden voor stralentheorie niet langer geldig zijn. Verstrooiingstheorie kan worden gebruikt voor media waar snelheidsvariaties dezelfde orde van grootte hebben als de golflengte en de Fresnel zone van het gemeten golfveld.

Storingstheorie voor de faseverstoring van doorgelaten golven (om precies te zijn de Rytov benadering) wordt gebruikt voor het afleiden van de tijdsverschuiving m.b.t. traagheidsstoringen, die eindige frequentie-effecten bevatten. De wiskundige uitdrukking voor de tijdsverschuiving van doorgelaten golven is een integratie van het traagheidsstoringsveld vermenigvuldigd met de Fréchet afgeleide over het volume tussen bron en ontvanger. De Fréchet afgeleide hangt af van de frequentie-inhoud van het gemeten golfveld, en zij geeft aan wat de gevoeligheid voor traagheidsstoring is van elk punt in het volume tussen bron en ontvanger. In de hoofdstukken drie tot vijf wordt uitgelegd, dat de Fréchet funktie door de eindige frequentie-effecten van golven de eigenschap heeft, dat de maximale gevoeligheid voor traagheidsstoringen afwijkt van de baan van de geometrische straal. Met betrekking tot golven die zich in drie dimensies uitbreiden vindt men, in tegenstelling tot wat men zou verwachten op grond van stralentheorie, dat de gevoeligheid m.b.t. traagheidsstoringen op de geometrische straal nul is. De wiskundige uitdrukking

127

voor de tijdsverschuiving, die afgeleid is van de verstrooiingstheorie, is een generaliser-
ing van de tijdsverschuiving uit stralentheorie. Zo wordt bijvoorbeeld in hoofdstuk drie
tot vijf bewezen, dat stralentheorie en verstrooiingstheorie tot hetzelfde resultaat leiden
wanneer golven zich voortplanten in snelheidsmedia die voldoen aan de voorwaarden van
stralentheorie. In complexe snelheidsmedia, waar niet aan de voorwaarden voor stralen-
theorie voldaan wordt, geeft alleen verstrooiingstheorie een correct resultaat.

De hier ontwikkelde theorie, die rekening houdt met de geometrische effecten die niet
van stralen komen, is getest op een 2-dimensionaal numeriek experiment (hoofdstukken
drie en vier) en op een 3-dimensionaal ultrasoon experiment (hoofdstuk vier). In deze
twee experimenten voor doorgelaten golven worden snelheidsmodellen gebruikt die aan
de voorwaarden voor verstrooiingstheorie voldoen. Het 2-dimensionale numerieke ex-
periment en het drie-dimensionale ultrasone experiment laten duidelijk zien dat de the-
orie voor golven met eindige frequenties, de geobserveerde tijdsverschuivingen beter
kan voorspellen dan stralentheorie. Vooral in het ultrasone experiment wordt duidelijk
getoond dat stralentheorie de geobserveerde tijdsverschuivingen overschat in experimenten
waarin verstrooiingseffekten een rol spelen. De resultaten van het 2-dimensionale nu-
merieke experiment en het echte 3-dimensionale ultrasone experiment geven aan, dat het
niet juist is om stralentheorie te gebruiken in tomografische experimenten in de globale
seismologie, die snelheidsstrukturen tonen met dezelfde lengteschaal als de golflengte en
de Fresnel zone van de gemeten golven.

De vorming van triplicaties (gerelateerd aan "caustics") geeft aanleiding tot meer-
voudige golfvelden waarbij de amplitude van de eerst aankomende golf veel kleiner kan
zijn dan van de latere. Daarom is het moeilijk om de golf die het eerst aankomt te ont-
dekken als er triplicaties worden gevormd. Triplicaties worden gevormd, als een golfveld
zich uitbreidt in een medium met focuseringseffecten. In deze studie (hoofdstuk twee)
wordt laten zien in een numeriek experiment dat "caustics" verlaat zijn in verhouding tot
de eerste aankomst. Het is correct om de ontwikkelde verstrooiingstheorie te gebruiken
voor de golfveld van eerst aankomsttijden, ook al is de vorming van triplicaties dominant
in het gemeten golfveld.

De theorie voor golven met eindige frequentie effecten wordt gebruikt in een globaal
oppervlaktegolf experiment waarin de geobserveerde data de faseverschuivingen zijn van
Love golven tussen 40 s and 150 s (hoofdstuk vijf). Oppervlaktegolven zijn, zoals het
woord al aangeeft, golven die zich langs het oppervlak van de aarde uitbreiden. Love
golven zijn een speciaal soort oppervlaktegolven die worden gekarakteriseerd door hun
transversale en horizontale deeltjes beweging. De berekende fasesnelheidsmodellen van
een inversie van Love golf faseverschuivingen met gebruik van verstrooiingstheorie wordt
vergeleken met de corresponderende fasesnelheidsmodellen, die gebaseerd zijn op stra-
lentheorie (preciezer gezegd: de verstrooiingstheoretische grote cirkel die de lijn is die
een bron en ontvanger verbindt over een bolvormig oppervlak). Er bestaat geen noe-
menswaardig verschil tussen de fasesnelheidsmodellen die berekend zijn met stralenthe-
orie en zij die berekend zijn met verstrooiingstheorie. De rede hiervoor is, dat er in het
oppervlaktegolf inversie experiment een strenge regulariseringsvoorwaarde is gebruikt.
Deze regulariseringsregel onderdrukt het effect van heterogeniteiten met lengteschalen
die kleiner zijn dan de Fresnel zone. Op deze manier zijn de voorwaarden voor stralen-

heorie vervuld in de berekende fasesnelheidsmodellen. Een synthetisch experiment is geconstrueerd om de grenzen van stralentheorie in de tomografie van oppervlaktegolven te bepalen. Hieruit is gebleken, dat voor experimenten op het gebied van oppervlaktegol-ven de stralentheoretische grote cirkel benadering beperkt is tot snelheidsstrukturen met karakteristieke lengtes groter dan 1300 km en 2000 km voor Love golven met periodes van respectievelijk 40 s en 150 s.

Ten slotte wordt het gebruik van een speciale inversietechniek onderzocht in globale tomografie van oppervlaktegolven die "spectral leakage" theorie wordt genoemd (hoofd-stuk zes). De "spectral leakage" theorie stelt dat geobserveerde data beïnvloed kunnen worden door snelheidsstrukturen met lengteschalen waarmee in een inversie experiment geen rekening kan worden gehouden. Als de geobserveerde data niet wordt gecorrigeerd voor het "spectral leakage" probleem, is het mogelijk dat het geïnverteerde model een systematische fout bevat. Verstrooiingstheorie van oppervlaktegolven in combinatie met "spectral leakage" theorie wordt gebruikt bij een inversie van Love golf faseverschuivin-gen tussen 40 s en 150 s. De geïnverteerde oppervlaktegolf modellen van de "spectral leakage" inversie zijn berekend zonder regulariseringsvoorwaarde, maar toch tonen zij een goed verband met tektonische strukturen en grenzen tussen tektonische platen.

Resumé på Dansk

I dette phd-studium bliver teorien for bølgefelt-modellering og inverse problemer i seismisk tomografiske bølge eksperimenter forbedret. Problemet er, at de fleste bølgefelt-modellingsteknikker i global seismologi er baseret på simple versioner af stråleteori. Stråleteori er en høj-frekvens tilnærmelse, så betingelserne for stråleteori er kun opfyldt i glatte medier, hvor hastighedsanomalier ændrer sig langsomt over store længdeskalar sammenlignet med bølgelængden og vidden af Fresnel zonen af det registrerede bølgefelt. (Se Fig. 1.1 i introduktionen til denne afhandling for en forklaring af de fysiske variable). Dog er tendensen i global seismologi at forsøge at forbedre opløsningen af hastighedsstrukturer i regionale og globale hastighedsmodeller af Jorden p.g.a. den større computerkraft og forbedrede datasæt der eksisterer idag. Aktuelle hastighedsmodeller af Jorden i global seismologi viser karakteristiske længder af inhomogeniteter med samme størrelsesorden som bølgelængden og Fresnel zonen af det målte bølgefelt. Det betyder, at betingelserne for stråleteori generelt ikke er opfyldt i de nyeste hastighedsmodeller af Jorden. Det er istedet nødvendigt at indføre diffraktionsteori for at beskrive, hvordan bølger udbreder sig i medier, hvor betingelserne for stråleteori ikke længere er gyldige. Diffraktionsteori er relevant at anvende i medier, hvor hastighedsvariationer er af samme størrelsesorden som bølgelængden og Fresnel zonen af det registrerede bølgefelt.

Perturbationsteori for fase transmitterede bølger (mere præcist Rytov approksimationen, der er en faseskiftstilnærmelse) bruges til at udlede tidsskiftet mht. slowness perturbationer, der indeholder endelige frekvenseffekter. Udtrykket for tidsskiftet af transmitterede bølger er et integral af slowness perturbationsfeltet vægtet med Fréchet funktionen over volumet, der er imellem bølgekilden og modtageren. Fréchet funktionen er afhængig af frekvensindholdet af det registrerede bølgefelt, og den angiver sensitiviteten til slowness perturbationer for hvert punkt i volumet mellem kilde og modtager. Det er vist i kapitel tre til fem, at Fréchet funktionen p.g.a. endelige frekvenseffekter af bølger, har egenskaben, at den maximale sensitivitet mht. slowness perturbationer afviger fra banen af den geometriske stråle. For bølger, der udbreder sig i tre dimensioner, finder man det kontraintuitive resultat sammenlignet med stråleteorien, at sensitiviteten mht. slowness perturbationer er nul på den geometriske stråle. Udtrykket for tidsskiftet, der er udledt ved diffraktionsteori, er en generalisation af det stråleteoretiske tidsskift. For eksempel er det bevist matematisk i kapitel tre til fem, at man opnår det identiske resultat ved at bruge enten stråleteori eller diffraktionsteori for transmitterede bølger i hastighedsmedier, hvor betingelserne for stråleteori er gyldige. I mere komplicerede hastighedsmedier,

hvor betingelserne for stråleteori ikke er opfyldt, er det kun korrekt at anvende diffraktionsteori.

Den udviklede teori, der tager geometriske effekter ikke hidrørende fra stråler i betragtning, er testet i et 2-dimensionalt numerisk bølge eksperiment (kapitel tre og fire) og i et 3-dimensionalt ultrasonisk bølge eksperiment (kapitel fire). I disse to bølge eksperimenter for transmitterede bølger anvendes hastighedsmodeller for hvilke betingelserne for diffraktionsteori er gyldige. Det er tydeligt vist i det 2-dimensionale numeriske bølge eksperiment og i det 3-dimensionale ultrasoniske bølge eksperiment, at teorien for bølger med endelige frekvenser er bedre end stråleteori til at forudsige de observerede tidsskift. Det er især tydeligt dokumenteret i det ultrasoniske bølge eksperiment, at stråleteori overestimerer de observerede tidsskift i bølge eksperimenter, hvor diffraktionseffekter er relevante. Resultaterne fra det 2-dimensionale numeriske bølge eksperiment og det 3-dimensionale ultrasoniske bølge eksperiment indikerer, at det ikke er korrekt at benytte stråleteori i tomografiske høj-opløsnings bølge eksperimenter i global seismologi, der viser hastighedsstrukturer med samme længde-skala som bølgelængden og Fresnel zonen af de målte bølger.

Triplikationer (relateret til kaustiks) er bølgefelter med flere ankomststider. Ampliduden af det først ankomne bølgefelt er ofte lille i forhold til ampliduden af de bølgefelterne, som kommer derefter. Det er derfor svært at detektere den først ankomne bølge, når triplikationer er tilstede i det målte bølgefelt. Triplikationer bliver udviklet, når et bølgefelt udbreder sig i et medium med fokuseringseffekter. Det er vist i dette studium (kapitel 2), at kaustiks er forsinkede i forhold til det ballistiske bølgefelt p.g.a. kausalitet. Den udviklede diffraktionsteori for først ankomne bølger er stadig korrekt at benytte, selvom tilstedeværelsen af triplikationer er dominerende i det registrerede bølgefelt.

Teorien for bølger med endelige frekvenseffekter er brugt i et globalt overfladebølge eksperiment, hvor de observerede data er faseskift for Love bølger mellem 40 s og 150 s (kapitel 5). Overfladebølger er, som ordet indikerer, bølger, der udbreder sig langs Jordens overflade, og Love bølger er en special type af overfladebølger karakteriseret ved dets amplitude, der er transversal og horisontal. De beregnede fasehastighedsmodeller fra inversionen af Love bølge faseskift ved brug af diffraktionsteori er sammenlignet med de tilsvarende fasehastighedsmodeller, som er baseret på den stråleteoretiske storcirkel approksimation. Der er ikke nogen nævneværdig forskel mellem fasehastighedsmodellerne beregnet med stråleteori eller diffraktionsteori, hvilket skyldes at der i inversionsproblemet er inkluderet en streng regulariseringsbetingelse. Den restriktive regulariseringsbetingelse undertrykker effekten af heterogeniteter med længde-skalaer mindre end Fresnel zonen, så betingelserne for stråleteori er opfyldt i de beregnede fasehastighedsmodeller. Et syntetisk eksperiment er konstrueret for at bestemme begrænsningen af stråleteori i overfladebølge tomografi. For globale overfladebølge eksperimenter er det derved fundet, at den stråleteoretiske storcirkel approksimation er indskrænket til hastighedsstrukturer med karakteristike længder større end 1300 km og 2000 km for Love bølger med de respektive perioder på 40 s og 150 s.

Til sidst bliver anvendelsen af en særlig inversionsteknik, kaldet spektral lækage teori, i global overfladebølge tomografi undersøgt (kapitel seks). Spektral lækage teori handler

om, at observerede data kan være påvirket af hastighedsstrukturer med en længde-skala, der ikke er taget højde for i en given inversion. Hvis de observerede data ikke bliver korrigeret for det spektrale lækage problem, er det muligt, at den inverterede model indeholder en systematisk fejl, da effekten af inhomogeniteter, der ikke er medtaget i inversionen, kan lække ind i den estimerede model. Overfladebølge diffraktionsteori kombineret med spektral lækage teori er anvendt i en inversion af Love bølge faseskift mellem 40 s og 150 s. De inverterede overfladebølge modeller med den spektrale lækage korrektion af faseskift er beregnet uden brug af en regulariseringsbetignelse, og viser en god korrelation med tektoniske plade grænser og strukturer.

Acknowledgments

In this acknowledgement, I would like to thank the people who have contributed to this thesis in one way or another. First, I am grateful to my promotor and supervisor Roel Snieder for his positive attitude, enthusiasm and inspiration at all moments during the work of my PhD project. We did not only find a common interest in geophysics, but also in firefighting.

My co-promotor and supervisor Jeannot Trampert introduced me to surface wave tomography, and he taught me the importance of error analysis. Cees Wapenaar is the unofficial supervisor of this PhD-project. I want to thank him for accepting me at TU-Delft (Mijnbouw) and for spending time on my project though he was busy with his own work.

Osamu Nishizawa (Geological Survey of Japan) and Chadaram Sivaji (now at: Ministry of Science and Technology, India): doomo arigatoo gozaimasu. They accepted me without hesitation for a jointed a project where laboratory data and theory were applied together (see chapter four).

Kabir Roy-Chowdhury and Hanneke Paulssen contributed to this project by providing me with software and by commenting on the chapters of the dissertation. Joop Hoofd and Theo van Zessen were always kind to help me with matters concerning the computer system at Utrecht University.

I would like to thank the PhD-committee (Jaap Mondt, Jean-Paul Montagner, Roel Snieder, Chris Spiers, Jeannot Trampert and Cees Wapenaar) for reading my dissertation at short notice.

Petter Bragd, Frédéric Deschamps and the players on the basketball team "The TurpEddies" contributed non-academically to my PhD-project. It was fantastic to spend time with friends to do sport, to travel and to go on day or weekend trips in the Netherlands.

At Utrecht University, at TU-Delft and at Colorado School of Mines, I had the opportunity to meet many undergraduate students, graduate students and staff: Caroline Beghein, Rob Devilee, Nicolette Filippidou, Martijn Frijlink, Alex Gret, Stephanie Godey, Yann Gourvil, Renata Hertog, Jeroen van Hunen, Hester Kleinhaus, Dirk Kraaijpoel, Jasqueline Landsheer, Henk van de Meer, Everhard Muijzert, Sander van Ouwerkerk, Sandra Richwalski, Joe Resovsky, Axel Röehm, Stan Schooft, Antonio Ranada Shaw, Sevgi Tigrek, Robbert van Vossen, Arie van Wettum, Kasper van de Wijk, Tim van Zon and many others.

My parents Lone and Erik Spetzler have visited me many times in the Netherlands

during my work with the PhD-project, and especially my father has shown a great interest in understanding the topic of my research project though he has graduated in a completely different field. The parents of my girlfriend, José and Johan van Damme are always kind to invite me to their home in Zeeland at any occasion.

Lastly, but nonetheless the most important person in my life, I would like to thank my girlfriend Esther van Damme for her patience with me. She is my muse.

Curriculum vitae

July 13, 1972	Born in Copenhagen, Denmark
1978 - 1987	Primary school in Albertslund, Denmark
1987 - 1991	Secondary school (Gymnasium) in Albertslund, Denmark
1991 - 1994	Study of physics and mathematics, University of Copenhagen, Denmark
1994 - 1997	Study of geophysics, University of Copenhagen, Denmark
1995 - 1996	Study of geophysics, Institut de Physique du Globe de Paris, France
1997 - 1997	Military service in Hillerød (firefighter), Denmark
1997 - 2001	PhD student at Utrecht University, The Netherlands